



# Athos Conceptual Design Report

PSI Bericht Nr. 17-02  
September 2017  
ISSN 1019-0643

## Cover figure description

SwissFEL Building aerial view: With a total length of 719 m, the accelerator and undulators are located in the ground floor of a two-storey building. Most of the building is underground, but the upper floor (technical buildings) is only semi-covered with soil, to ensure good maintenance access. The experimental area building is a single-storey building which is naturally covered by the surrounding land. The main access road to this area is clearly visible on the bottom left corner of the picture.

### Editor

Romain Ganter

### Review Board

Hans Heinrich Braun  
Terry Garvey  
Florian Löhl  
Bruce Patterson  
Marco Pedrozzi  
Luc Patthey  
Sven Reiche

### With contributions from:

#### Executive Summary

Abela R.  
Braun H.H.  
Ganter R.  
Patterson B.  
Patthey L.  
Reiche S.

#### Design Strategy and Parameters Choice

Prat E.  
Reiche S.

#### Electron Components

Alex J.  
Calvi M.  
Celcer T.  
Craievich P.  
Dordevic S.  
Ganter R.  
Gough C.  
Hauri C.  
Hunziker S.  
Ischebeck R.  
Joehri H.  
Keil B.  
Kuenzi R.  
Paraliev M.  
Pedrozzi M.  
Sanfilippo S.  
Schilcher T.  
Schlott V.  
Schmidt T.  
Trisorio A.  
Zandonella A.  
Zennaro R.

#### Photon Components

David C.  
Flechsigg U.  
Follath R.  
Gerber S.  
Juranic P.  
Milne C.  
Patthey L.  
Pradervand C.  
van Daalen M.

#### Building and Infrastructure

Grossenbacher B.  
Hüsler E.  
Reinhard D.  
Fuchs A.  
Ganter R.  
Hohmann E.  
Janzi G.  
Scheibl R.  
Widmer I.

# Acknowledgements

The author list of this report is limited to the people who have actually written text or supplied figures or tables appearing in the CDR. Many more people from PSI and abroad have contributed to SwissFEL and indirectly to the content of the CDR. The authors of this CDR recognize in particular that the concept for SwissFEL emerged from the “LEG/FEL” R&D activity which was launched at PSI under the leadership of Prof. Albin Wrulich in 2003 [1,2]. Many contributions to the concept as well as to technical solutions which appear in this conceptual design report can be traced back to the work of this R&D activity, although it was not always possible to put references to this work.

Furthermore we profited from the advice and collaboration with many experts from other laboratories. In particular we would like to thank our colleagues from CANDLE, CERN, DESY, ELETTRA, EMPA, HZB, INFN-LNF, PAL-XFEL, SINAP, SLAC and SPRING8.

Last, not least we acknowledge the enormous help and constructive critics we got from the SwissFEL machine advisory committee FLAC chaired by Prof. Jörg Rossbach.



# Contents

<b>1</b>	<b>Executive summary</b>	<b>6</b>			
<b>1.1</b>	<b>Athos project goals and CDR objectives</b>	<b>6</b>			
<b>1.2</b>	<b>Athos design rational</b>	<b>6</b>			
1.2.1	Introduction	6			
1.2.2	Technical highlights of Athos	7			
1.2.3	The injector	8			
1.2.4	The accelerator	8			
1.2.5	The FELs	8			
<b>1.3</b>	<b>SwissFEL building</b>	<b>9</b>			
1.3.1	SwissFEL facility site	9			
1.3.2	Building overview	11			
<b>1.4</b>	<b>Key parameters</b>	<b>12</b>			
<b>1.5</b>	<b>Athos project schedule</b>	<b>13</b>			
<b>1.6</b>	<b>Overview of ATHOS Science Case</b>	<b>14</b>			
<b>2</b>	<b>Design strategy and parameter choice</b>	<b>18</b>			
<b>2.1</b>	<b>Overview and design parameters</b>	<b>18</b>			
<b>2.2</b>	<b>Athos electron beamline</b>	<b>20</b>			
2.2.1	Switchyard	20			
2.2.2	Optics	20			
2.2.3	Dechirper	21			
2.2.4	Post-Undulator Transverse Deflector	22			
2.2.5	Seed-Laser Consideration	23			
2.2.6	Undulator line parameters	23			
<b>2.3</b>	<b>Operation Modes</b>	<b>23</b>			
2.3.1	Normal Operation	23			
2.3.1.1	<i>SASE Operation</i>	23			
2.3.1.2	<i>Optical Klystron</i>	25			
2.3.2	Coherence Control	25			
2.3.2.1	<i>Self-Seeding</i>	25			
2.3.2.2	<i>Phaselocked Double Pulses</i>	25			
2.3.2.3	<i>High Brightness SASE</i>	26			
2.3.3	Bandwidth and Frequency Control	27			
2.3.3.1	<i>Two Color</i>	27			
2.3.3.2	<i>Large Bandwidth</i>	28			
2.3.4	Power and Pulse Length Control	29			
2.3.4.1	<i>Terawatt-Attosecond Mode</i>	29			
2.3.4.2	<i>Slotted Foil</i>	29			
2.3.5	Timing Control	30			
2.3.5.1	<i>Slicing</i>	30			
2.3.5.2	<i>HHG Seed</i>	31			
2.3.5.3	<i>Mode-locked Lasing</i>	33			
<b>3</b>	<b>Electron beam components</b>	<b>34</b>			
<b>3.1</b>	<b>Laser system</b>	<b>34</b>			
3.1.1	Gun laser system	34			
3.1.2	General layout	34			
3.1.3	Two bunch operation regime	35			
<b>3.2</b>	<b>RF systems</b>	<b>36</b>			
3.2.1	RF systems of the Athos Linac	36			
3.2.1.1	<i>C-Band module overview</i>	37			
3.2.1.2	<i>C-band Accelerating Structure</i>	37			
3.2.1.3	<i>RF C-band Pulse Compressor</i>	37			
3.2.2	Power systems for the SwissFEL linac	38			
3.2.2.1	<i>C-Band Klystron</i>	38			
3.2.2.2	<i>C-Band Modulator</i>	39			
3.2.3	Post-undulator X-band Transverse Deflecting Structures (TDSs)	39			
3.2.4	Low-Level RF	42			
<b>3.3</b>	<b>Timing and synchronization</b>	<b>44</b>			
<b>3.4</b>	<b>Magnets</b>	<b>44</b>			
3.4.1	Quadrupole Magnets	44			
3.4.2	Dipole magnets	46			
3.4.3	Corrector magnets	47			
3.4.4	Sextupole magnets	47			
3.4.5	DC magnet power supplies	47			
3.4.6	Septum and Kicker systems	50			
<b>3.5</b>	<b>Undulators</b>	<b>52</b>			
3.5.1	Athos undulator	52			
3.5.2	Undulator module	54			
3.5.3	Mechanics	56			
3.5.4	Inter-undulator magnetic delay chicane design	58			
3.5.5	Undulator tolerances	60			
3.5.5.1	<i>Error Sources in the undulator lines</i>	60			

3.5.5.2	<i>Measurements and Alignment of Undulator magnet arrays</i>	60	4.3.3	Optical Beamlines	82
			4.3.3.1	<i>Pink beam operation</i>	82
<b>3.6</b>	<b>Electron beam diagnostics concept</b>	<b>61</b>	<b>4.4</b>	<b>Experimental Hall</b>	<b>83</b>
3.6.1	Overview electron beam diagnostics	61	4.4.1	Concepts for experimental endstations	84
3.6.2	Description of the different electron beam diagnostics	63	4.4.1.1	<i>Condensed matter physics</i>	85
3.6.2.1	<i>Transverse profile monitors</i>	63	4.4.1.2	<i>Ultrafast chemistry and biology</i>	85
3.6.2.2	<i>Wire-scanners and beam loss monitors</i>	63			
3.6.2.3	<i>Beam arrival monitors</i>	64	<b>5</b>	<b>Building and infrastructure</b>	<b>87</b>
3.6.3	Beam position monitor system	64	<b>5.1</b>	<b>Building layout</b>	<b>87</b>
<b>3.7</b>	<b>Undulator Vacuum concept</b>	<b>65</b>	<b>5.2</b>	<b>Safety issues</b>	<b>92</b>
3.7.1	Chamber Design	65	<b>5.3</b>	<b>Supply installations</b>	<b>94</b>
3.7.1.1	<i>Production Process</i>	65	5.3.1	Electrical supply and consumption	94
3.7.2	Vacuum Performance	66	5.3.2	Heating, cooling, air conditioning and water supplies	94
3.7.3	Further steps	66	5.3.2.1	<i>Summary</i>	94
<b>3.8</b>	<b>Mechanical systems</b>	<b>66</b>	5.3.2.2	<i>Heating / Cooling facilities</i>	94
3.8.1	Girder Concept	66	5.3.2.3	<i>Air conditioning units</i>	95
3.8.2	Special mechanical systems	66			
3.8.2.1	<i>Dechirpers</i>	66	<b>6</b>	<b>References</b>	<b>97</b>
<b>3.9</b>	<b>Control system</b>	<b>69</b>			
3.9.1	EPICS environment	69		<b>PSI in brief</b>	<b>99</b>
3.9.2	Network infrastructure	70		Imprint	99
3.9.3	Software maintenance and distribution	70			
3.9.4	Controls infrastructure and subsystems	70			
3.9.4.1	<i>Timing</i>	71			
3.9.4.2	<i>VME IOC systems</i>	72			
3.9.4.3	<i>I/O signals</i>	72			
3.9.4.4	<i>Motion systems</i>	72			
3.9.4.5	<i>Cameras</i>	73			
3.9.4.6	<i>Data Archiving</i>	74			
3.9.4.7	<i>Other Interfaces</i>	74			
<b>4</b>	<b>Photon beam components</b>	<b>75</b>			
<b>4.1</b>	<b>Front End Layout</b>	<b>75</b>			
<b>4.2</b>	<b>Photon Beam Diagnostics</b>	<b>75</b>			
<b>4.3</b>	<b>Athos optical layout</b>	<b>79</b>			
4.3.1	Introduction	79			
4.3.2	Incident photon beam characteristics	80			

# 1 Executive summary

## 1.1 Athos project goals and CDR objectives

The goal of Athos is to provide a source of extremely bright and short soft X-ray pulses enabling scientific discoveries in a wide range of disciplines, from fundamental research to applied science. The eminent scientific need for such a source is well documented in the Athos Science Case Report [3].

The technical design of Athos has to keep a delicate balance between the demand from experimentalists for breathtaking performance in terms of photon beam properties, on the one hand, and essential requirements for a user facility, such as confidence in technical feasibility, reliable and stable functioning, and economy of installation and operation, on the other hand. A baseline design has therefore been defined which relies entirely on state-of-the-art technologies or on components already existing in the SwissFEL Aramis line. This Athos Conceptual Design Report (CDR) describes the technical concepts and parameters used for this baseline design, as of the beginning of 2016. The objective of the CDR is to provide a reference for the machine design, thus ensuring that the various teams working on Athos use consistent planning assumptions. Given that the design is still evolving, all relevant modifications relative to the CDR have to be documented in an unambiguous manner accessible to all personnel involved in SwissFEL Athos. The design with all accumulated modifications and more detailed technical component descriptions and specifications will have to be compiled again in the technical design report SwissFEL TDR [4].

## 1.2 Athos design rational

### 1.2.1 Introduction

In a free-electron laser, the active medium is a beam of relativistic electrons. This beam moves in vacuum through a periodic magnet array, called an undulator, forcing the electrons to follow a wiggling orbit centered on a straight line. The wiggling orbit introduces a transverse velocity component, which allows the electrons to exchange energy with a light wave which is co-linear with the electron beam. The electrons become accelerated or decelerated, depending on the phase of the transverse electric field of the light wave. For a particular wavelength of the light beam, this exchange becomes resonant for a single electron, leading to a continuous transfer of energy from the electron to the light wave. The resonant wavelength is given by

$$\lambda = \frac{\lambda_U}{2\gamma^2} \left( 1 + \frac{K^2}{2} \right)$$

where  $\lambda_U$  is the period length of a planar undulator and  $K$  is the undulator parameter, defined by

$$K = \frac{1}{2\pi} \frac{e}{mc} B_U \lambda_U$$

with  $B_U$  the peak magnetic field of the undulator on the axis. Since the path length of the electrons depends on the electron energy, the energy modulation induced by the radiation field is converted to a bunching of the electrons with the periodicity of the light wave.

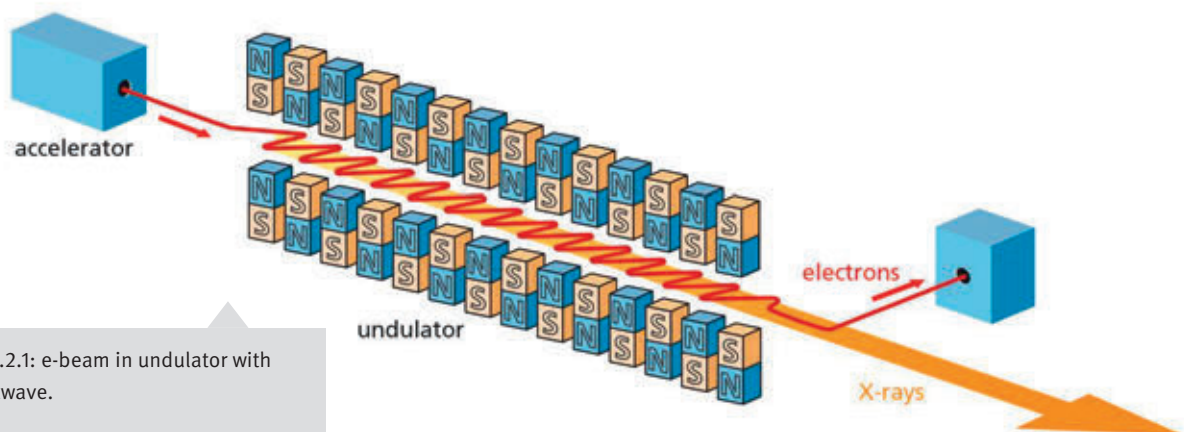


Fig.1.2.1: e-beam in undulator with lightwave.

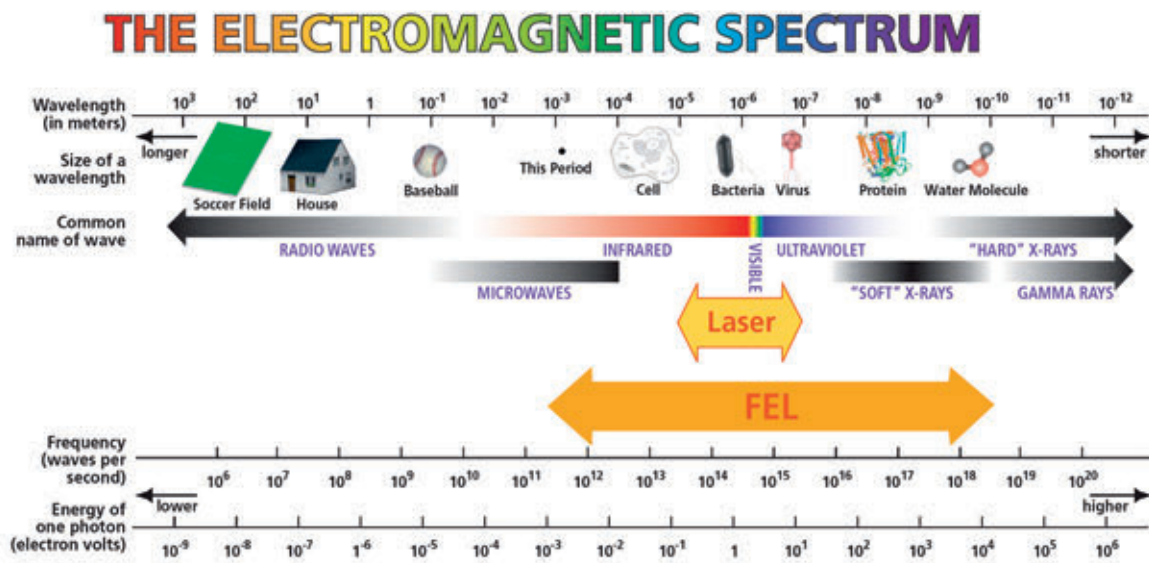


Fig. 1.2.2: Wavelength range of the FEL vs. a quantum laser.

Thus the electrons are concentrated at the phase of the light wave where efficient energy transfer occurs and the light wave becomes coherently amplified. As a result, the entire system acts analogously to a light amplifier in the well-known optical quantum laser. However, the FEL has the fundamental advantage that its operation does not depend on quantum transitions in a specific laser medium. Therefore, the FEL scheme can be applied over a much wider photon wavelength range than the quantum laser principle, as shown in Figure 1.2.2. The FEL principle is the only proven method for providing coherent light pulses reaching the X-ray wavelength regime. The Athos baseline design aims to produce FEL pulses covering the photon energy range 250 eV to 1900 eV (or in wavelength 6.5 Å to 49 Å). This energy range includes the K shell binding energy of two important atoms in the nature: the carbon K edge at 280 eV and the silicon K edge at 1850 eV.

### 1.2.2 Technical highlights of Athos

In order to increase performances in terms of photon beam brightness and bandwidth and still meet the cost constraints, several innovative lasing schemes and technical developments for some key components are underway. For these developments, Athos profits not only from the excellent R&D performed at PSI for SwissFEL, but also from the vast experience and progress achieved at other laboratories active in electron linac and FEL design. Introduction of new concepts makes the SwissFEL Athos line unique. These innovations can be listed as follows:

- Fast and stable resonant kicker will separate the electron bunches which goes to Athos from those going to Aramis.
- Dechirper units will be integrated in the dog leg section in order to remove the remaining electron energy chirp.
- The undulator line will integrate small magnetic chicanes in the space between the undulator modules [5]. This allows special operating modes with potentially following benefits in comparison to SASE operation:
  - reduction of the required undulator length to achieve FEL saturation (optical klystron mode),
  - improvement of the longitudinal coherence of the FEL pulses (high brightness mode),
  - ability to produce shorter FEL pulses with higher-power levels (TW attosecond mode).
- In addition to these compact small chicanes, a larger 4 electromagnet dipole chicane will be installed in the middle of the Athos undulator line in order to adjust the time delay (0 to 500 fs) between 2 pulses with two different colors (2 colors mode).
- The undulators will have a new design, the so-called APPLE X design where the 4 magnet arrays can be moved radially in a symmetric way enabling full polarisation control. This offers new possibilities like to scan rapidly the photon energy while keeping the polarisation constant or to produce transverse magnetic gradient for generation of beam with up to 10% bandwidth (ultra-large bandwidth mode [6]).
- The undulator will use an ultra-thin vacuum chamber of 5 mm inner diameter and only a few hundred micrometers

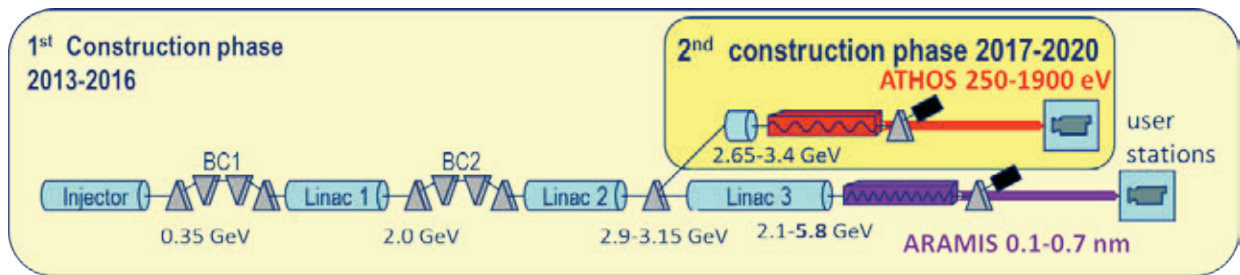


Fig. 1.2.3: SwissFEL layout schematic with the Aramis and Athos FEL.

wall thickness produced by galvanic technics. This lead to an outer vacuum chamber diameter of less than 5.5 mm.

- Finally an X band post-undulator deflecting cavities will be located downstream the undulator line to have an online diagnostic of the FEL process which is especially important if one consider all the different modes of operation (SASE, 2 colors, high-brightness mode, optical klystron ...).

### 1.2.3 The injector

The baseline technology for the SwissFEL electron injector relies on the RF gun photo-injector concept. A semi-conductor photocathode placed in a high-field RF cavity is illuminated with a short-pulse laser. The timing of the laser pulses is synchronized to the RF, so that electrons are emitted when the accelerating RF field on the cathode reaches an optimum value. Several bunches can be extracted from the photocathodes if a train of laser pulses is sent to the cathode. The total maximum charge which can be sent to Athos and Aramis are limited to 800 pC at 100 Hz repetition rate in each line with a minimum bunch separation of 28 ns (see section 4.2).

### 1.2.4 The accelerator

The SwissFEL linear accelerator (linac) must fulfil two functions:

- acceleration of the electron bunches from the injector to the nominal energy of each FEL Line: 5.8 GeV for Aramis and between 2.9 and 3.15 GeV for Athos
- time compression of the electron pulse from 5 ps rms to 25 fs rms

For temporal pulse compression, two magnetic chicanes are placed in the linac at 355 MeV and 2.0 GeV. A magnetic resonant kicker, positioned at the end of the Linac 2, will split the beam in two: the first bunch goes straight to the Aramis FEL line while the second bunch (28 ns later) is deviated to the Athos line.

In order to cover the full photon energy range from 250 to 1900 eV (6.5 to 49 Angstrom), the electron beam energy

in the Athos undulator line has to be varied from 2.65 to 3.4 GeV in addition to the undulator K parameter tuning from 1 to 3.6 (see Fig. 1.2.4). This energy tuning is done with a small linac installed in Athos, the so-called Athos Linac, which can either accelerate or decelerate the beam by 250 MeV in combination to a variable extraction energy downstream the linac 2 between 2.9 and 3.15 GeV. Changing the extraction energy present the inconvenient of coupling the Aramis and Athos line but allows the reduction of the Athos linac to only one C band module. A future extension of the Athos linac to 2 C band modules will allow operation at a fixed extraction energy of 3 GeV in case the coupling Athos / Aramis appears to be too complicate in terms of operation.

### 1.2.5 The FELs

The soft X-ray SASE FEL line Athos will be driven by the main linac and the Athos linac to cover the energy photon range 250 – 1900 eV (6.5 - 49 Å). The Athos undulator period is 38 mm and the permanent magnet arrays can therefore be situated outside the vacuum chamber. These undulators are built in the so-called APPLE X configuration [7], which allows full control of the FEL polarization, wavelength and transverse gradient by adjusting the radial and longitudinal

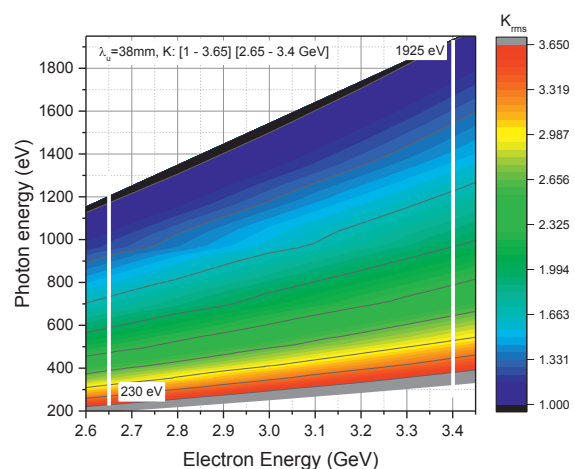


Fig. 1.2.4: 1D simulation of the Athos FEL photon energy in function of the electron beam energy and the undulator rms K value (undulator period length is 38mm). The Athos Undulator design covers the range 250 eV to 1900 eV.

position of the magnet arrays. Movements of the magnet arrays with micrometres accuracy have to be performed in the presence of very strong magnetic forces, making the mechanical design of the mover systems particularly challenging. The feature of polarization control will be particularly advantageous for magnetization dynamics experiments. In an APPLE X configuration, the magnetisation is at 45 degrees to maximize the magnetic field amplitude near the beam but also the motion of the arrays is radial with 45 degrees angle. As a consequence, the mechanics will open the gap and the slit in a symmetric way (radial motion) so that the photon energy can be scanned while keeping the polarisation. If only the right (or left) arrays – gap is open then the electron beam sees a transverse magnetic gradient [6] which offers new operation scheme like for example lasing with a large bandwidth. Finally, a new type of vacuum chamber with ultra-thin walls will allow a minimum aperture clearance of 6.5 mm.

The real innovative part of the Athos FEL lines lies in the installation of small magnetic chicanes in between every undulator segment. These chicanes can be used to delay electrons and / or to shift electron horizontally or to compress electrons bunches. Thanks to these chicanes one can operate the FEL in different modes:

- **Optical Klystron mode** [8] [9]: The chicane is used to convert an energy modulation in a density modulation which speeds up the SASE process and makes the saturation length shorter. As a consequence there is more undulator length for tapering (to get more FEL power) or to generate a second color (two color modes) [5].
- **High brightness SASE mode** (or purified SASE mode): The chicane is used to delay the electron bunch after every undulator segment in order to increase the cooperation length so that the bandwidth of the FEL light becomes smaller. By delaying the electron bunch, a given coherent wave pulse (SASE spike) will induce coherent microbunching over a longer portion of the electron bunch and so increase the cooperation length [5].
- **Superradiance mode** (or **TW pulse mode**): the electron bunch is first tilted transversally such that only a slice of the bunch is lasing. Once the lasing of this slice saturates, the bunch is delayed so that an adjacent slice with fresh electrons starts to lase [10] [5].

- In the **two colors mode** [11,12], the undulator line is splitted into two parts with a 4 dipoles magnetic chicane in between. Each undulator part is tuned at a different wavelength with up to a factor five difference. The duration between the two FEL pulses can be adjusted with the chicane between -10 fs to +500 fs. This chicane, at SATUN14, could be in a later stage completed by a monochromator to allow self-seeding operation. But in the first phase of Athos, the bandwidth obtained with the High Brightness mode of operation should be only a factor two larger than the self-seeding bandwidth.
- In the **ultra large bandwidth mode** [6], the beam is tilted to become larger transversally and the undulator is tuned to have a transverse magnetic gradient such that electrons are lasing at a different wavelength depending on their transverse position. Up to 10 % full width bandwidth could be potentially reached with this method

Another possible and attractive upgrade of the Athos line is the synchronisation of the FEL with an external laser. The principle is to modulate the electron bunch energy distribution by interaction of a laser pulse with the electron bunch in the last dipole of the transfer line. On top of time locking which is of high importance for pump – probe experiment, mode locking and slicing schemes become possible and would produce trains of sub-attosecond FEL pulses and femtosecond pulse of almost TW power [13] [14].

FEL seeding with an external source at these short wavelengths is an as-yet unproven technology, and considerable R&D, with uncertain outcome, is required in order to apply it for Athos.

### 1.3 SwissFEL building

#### 1.3.1 SwissFEL facility site

The location of the 700m-long SwissFEL facility near the PSI campus is shown on Figure 1.3.1.1. The site has been chosen because of almost ideal conditions for stability and the availability of ground water for an efficient cooling-water supply at low and constant incoming temperature. The pre-assembly of the Athos girder will be done directly in the SwissFEL building OSFA in various rooms (e.g. OSFA-UH.006).



Fig. 1.3.1.1: The location of the SwissFEL facility at PSI.



Fig. 1.3.2.1: SwissFEL Facility located in the forest close to the PSI campus.

### 1.3.2 Building overview

The overall length of the SwissFEL facility is about 720 m, with a width varying between 6 and 40 m (Fig. 1.3.2.1). The building is less than 10 m high where two levels are foreseen. A footprint drawing of the facility is shown in Figure 1.3.2.2. The linac is built on two levels (see Figure 1.3.2.2), with the electron beam tunnel below ground, to minimize the radiation protection requirements (concrete wall thickness). This also has the advantages of better temperature and mechanical stability, and the overall visual impact on the landscape is minimized. On the top floor of the electron accelerator section, a series of infrastructure buildings hosts all the necessary RF power stations, control units, water cooling system, electrical power supply and air conditioning system. These infrastructure buildings are separated from the electron beam tunnel by a thick concrete floor, for radiation shielding. This allows easy access during facility operation for maintenance of all technical installations.



Fig. 1.3.2.3: Sectional view of the SwissFEL Tunnel (z=520 m, looking towards gun), showing the Aramis Undulator line (on the left) and the available space for the Athos line (right).

The Athos undulator line starts with the switchyard fast kickers at z=265 m which separate the Athos bunch from the Aramis bunch. The Athos electron branch ends up with the beam dump at z=517m. The Athos photon beamline starts already in the tunnel with front end components before to enter into the Athos optical hutch (z=538m – 604m) where all the mirrors and monochromators are located. Finally the FEL pulses arrive in the Athos experimental hall which is a large open room of about 650m<sup>2</sup> to ensure maximal flexibility in the installation of experiments.

Fig. 1.3.2.2: SwissFEL Facility overview from the injector (at the left end) to the Aramis experimental hall (on the right).

1st Floor: Infrastructure gallery



Pump Laser Room



Ground Floor: Beam Tunnel

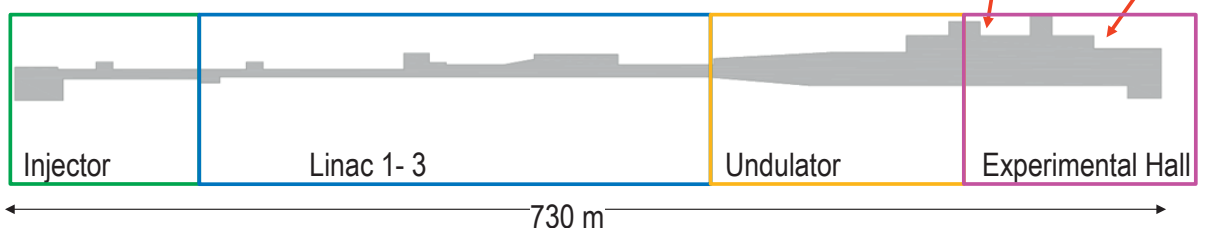


Table 1.4.1 Key parameters and features of SwissFEL Athos line.

Overall length (incl. experimental hall)	From z =265 m to 658 m (393 m)
Total electrical power consumption	0.6 MW
Maximum electron beam energy	3.4 GeV
Height of beamline above tunnel floor	1.2 m (for the electron beam) 1.4 m (for the experimental end stations)
Electron gun	3 GHz RF gun with 2.5 cells
Cathode type	Cs <sub>2</sub> Te or Cu photocathode driven by a CaF laser
Injector booster	Normal-conducting travelling wave structures (copper) with $\nu=3$ GHz
RF source main linac	Klystron with solid-state modulator and RF pulse compression
Accelerating structures, main linac	Normal conducting travelling wave structures (copper) with $\nu=5.7$ GHz and $G=26-28$ MV/m
Linac repetition rate	100 Hz
Undulator type, Athos	Apple X permanent magnet with $\lambda U=38$ mm
Wavelength range, Athos FEL	250 eV – 1900 eV (6.5 Å–49.6 Å);
Polarization, Athos	Variable (circular, elliptical and linear)
FEL pulse energy	50 $\mu$ J (2 colors mode) to 8 mJ (at 250 eV)
FEL pulse Bandwidth	0.02 % (High Brightness mode) to 10 % (large BW mode)
FEL pulse length	1 – 30 fs

## 1.4 Key parameters

### • SwissFEL Athos key parameters

Some key parameters and features of Athos are summarized in Table 1.4.1 left side.

The SwissFEL injector and accelerator permit a wide range of electron beam parameters that are described in Section 2. Two basic modes – “long pulse” and “short pulse” – are defined as the standard operation modes. In addition to variation of the electron bunch charge (and duration) the magnetic chicanes of the Athos undulator line allows a full set of different operation regimes already mentioned in section 1.2.5.

Since these new lasing schemes have not yet been proven experimentally, the Athos undulator line will be designed to also allow for a conventional SASE operation. The electron beam parameters and associated FEL parameters for these modes are summarized in Table 2.1.1 to 2.1.3.

The SwissFEL linac operates with a repetition rate of 100 Hz. At each linac pulse, two bunches are accelerated with a spacing of 28 ns. While the first bunch goes straight to the Aramis FEL line, the second is deviated to the Athos FEL by a fast kicker in the switchyard between Linac 2 and Linac 3 at an energy varying between 2.9 and 3.15 GeV. This timing scheme allows both FEL lines to be operated simultaneously at 100 Hz, thus doubling the number of photon pulses sent to the experiments.

### • SwissFEL operations scenario parallel to Athos installation

In 2017, the tunnel opening will depend on the delivery of the linac RF modulators which need to be connected to their respective C band structures in the tunnel. This corresponds to roughly one week shutdown per month.

In the period 2018-2020 starts the user operation: Periods of 12 weeks with alternating machine development and user

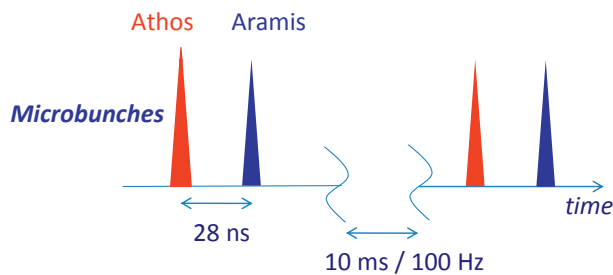


Fig: 1.4.1 Time structure of linac beam.

operation time and also including at least 2 to 3 weeks shutdown in a row for Athos installation.

In addition, it is planned to have following yearly shutdowns: 3 weeks at the end of the year: 3rd week of December to 2nd week of January, 6 weeks in summer from 1st of August to mid of september.

SwissFEL plans to operate continuously 24h a day and 7 days a week. A maintenance break of 8 hours from 6:00-14:00, is planned during one of the working day of each week. The following shift of this shutdown day, will be dedicated to beam development and beam set-up from 14:00-7:00.

Experiments get beam time in 12h portions with a first shift 7:00-19:00 and the next shift 19:00-7:00 (except for shift before maintenance day which finishes at 6:00). Both FEL lines are served simultaneously at 100Hz with charges of 10-200pC in each FEL. Charges, bunch length and repetition rate are similar for both lines. Both X-ray beams can be switched off and on independently. The special operating modes of Athos (Table 1.4.2) are independent of Aramis operation. Both electron bunches can also be switched off and on independently. However, switching off ARAMIS electron bunch may require some readjustment of ATHOS beam. Photon beam repetition rate can be reduced independently for both lines.

Before tunnel access after high repetition rate running, cool down period of about 1h is foreseen.

On each FEL line one experiment will run, one will be ready for taking data (in case of sudden and unexpected beam availability) and one experiment will be in preparation. It is also possible to split the x-ray pulse into two experiments simultaneously. Ready for taking data implies availability of user and instrument within less than 1h.

Repetition rate of RF needs adjustment independent of beam (i.e. gun laser), such that usually  $f_{\text{Beam}} \leq f_{\text{RF}}$ . This is required to keep RF in thermal equilibrium.

In case of beam loss, the machine protection system (MPS) shall, depending on loss level, reduce repetition rate or stop beam (RF will however not be stopped to avoid thermal transients). MPS shall stop LLRF (Low Level RF) in case of exceeding dark current beam loss.

MPS interlocks in injector, linac 1 and linac 2 will stop both beams. MPS interlocks in linac 3 will stop only the ARAMIS beam. MPS interlocks in ATHOS will only stop ATHOS beam. In ARAMIS, the experimental hutch running with beam is closed, while the others are accessible. In ATHOS, all experimental areas are always accessible.

## 1.5 Athos project schedule

The present planning for SwissFEL Athos is summarized in Figure 1.5.1. Presently, the design of key components, such as undulators, is already in progress and many components (electromagnets, RF linac, diagnostics, ...) can be directly copied from the Aramis line. As a consequence, procurements can start already beginning of 2017. The installation of the required technical infrastructure (cooling stations, racks, cabling ...) will start in 2017 while the installation of the components in the tunnel will start in 2018, after the commissioning of the dogleg has been completed. The preparation and storage of accelerator components before installation in the SwissFEL tunnel will be carried out directly in rooms of the OSFA building (room UH.006 for vacuum components, EH.035 for the undulators). Girders and undulators that are pre-assembled will then be stored in the tunnel until their definitive installation. By the mid of 2019, installation of the Athos linac and undulator line will be completed, and commissioning of Athos will start. The

dogleg commissioning, will be performed beforehand, between ends of 2017 and beginning of 2018, to allow demonstration of 2 bunch operation before main machine commissioning. First beam transport to the Athos beam dump will start in fall 2019, with the goal of having first FEL lasing of Athos by end 2019 and regular user operation by fall 2020. A schematic sequence of the construction steps and main milestones are shown in Figure 1.5.1.

### 1.6 Overview of ATHOS Science Case

This Section gives a short overview of the experiments planned at the ATHOS soft X-ray XFEL and the expected scientific progress. As was done for the ARAMIS hard X-ray XFEL, many discussions were held with local and international research groups to highlight particularly promising areas of soft X-ray investigations, both for fundamental and applied science. A detailed description can be found in the Athos Science Case Report [3].

Of vital importance in today’s world are functional molecules and materials. These can be catalytic systems to produce plastics or purify gases or synthesize fuels, ultrafast electronic switches and high-capacity magnetic storage media

in information technology, or molecular complexes which govern cellular function and cause hereditary disease. The cogs in such functional molecules and materials are the valence electrons, which, due to their electric charge, light mass and moderate binding energy, determine the physical, chemical and biological properties of matter. For the same reasons, it is also the valence electrons which interact with external influences such as electromagnetic fields, optical excitation and neighboring reactive species. Since the advent of the optical laser in 1960, time-resolved optical spectroscopy has been developed into a powerful tool for investigating the properties of valence electrons in matter. A drawback of optical spectroscopy, however, is its general inability to determine the position on the atomic scale of the electrons being observed – information which is often only available from theoretical predictions.

With soft X-ray spectroscopy, however, one can use well-defined resonant atomic transitions to specifically address particular electron orbitals. In this way, for example, one can determine the chemical valence of a metal ion in a biological complex, or the symmetry of d-electrons in a cuprate superconductor, or the spin and orbital angular momenta of a particular ion in a magnetic material. For this reason, a variety of soft X-ray spectroscopies are now bread-and-but-

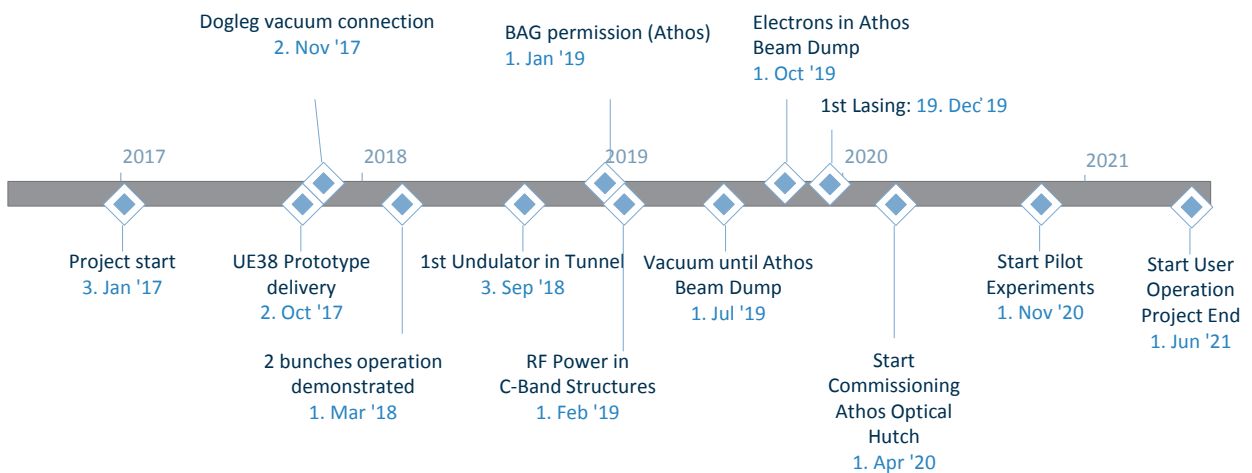


Fig.1.5.1 Schedule for Athos and main milestones.

ter users of the many synchrotrons in operation worldwide. In order to observe and quantify the *functionality* of matter, it is necessary to follow the dynamics of valence electrons on their natural time scale. These time scales  $\tau$ , in turn, are related by the Heisenberg uncertainty principle to the characteristic energy scales  $E$  involved, via the relation  $\tau = \hbar / E$ , where  $\hbar = 0.66$  eV fs. Hence, the dynamics of a valence electron with a typical interaction energy 0.1 eV must be probed on the time scale of 7 femtoseconds. Reasonably intense synchrotron pulses have a duration longer than 50 picoseconds – a factor of 7000 too slow. Only at a soft X-ray Free Electron Laser, such as ATHOS at SwissFEL, does one have the combination of peak intensity, wavelength tunability and fs pulse length required to perform dynamic soft X-ray spectroscopy (see Figure 1).

The hard X-rays to be available at the ARAMIS XFEL at SwissFEL will allow one to follow the motion of atoms. (An atom moving at the speed of sound requires 1 ps to travel 1 nm.) The ATHOS soft X-ray XFEL will immensely extend the capabilities of SwissFEL to dynamic soft X-ray spectroscopy and hence to the detailed study of functional molecules and materials. A further extension of capabilities offered by ATHOS over those at ARAMIS will be the ability to control the longitudinal coherence, allowing one, e.g., to produce approximately Fourier transform-limited pulses and to generate ultrashort double pulses, with variable wavelengths and inter-pulse delay. This ability will be particularly useful for the application of ATHOS pulses to non-linear X-ray optics. Direct beneficiaries of the ATHOS XFEL will be the chemical, materials and biological development programs at PSI, but also at Swiss universities and in international academic and industrial research laboratories.

The principal areas of application are the following:

---> **Ultrafast magnetization dynamics on the nanoscale**

Magnetism is responsible for one of the oldest inventions, the magnetic compass, and further applications have revolutionized our world, through, e.g., ferrite core memory to today's high-density data storage. In modern magnetic storage devices, of the order of 400 gigabits can be written per square inch at a rate of one bit per two nanoseconds. Faster reversal, on the sub-ps time scale, has been demon-

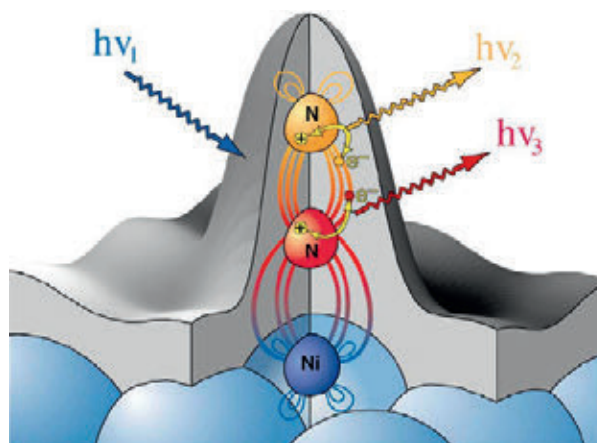


Fig. 1.6.1: Schematic representation of the “local probe” nature of soft X-ray spectroscopy, applied to an N2 molecule adsorbed on a nickel surface. The grey volume represents the electron density outside the metal surface, and the colored loops indicate a particular molecular orbital, which extends over both nitrogen atoms and a surface nickel atom. Following excitation by an incoming energetic X-rays  $h\nu_1$ , transitions between core and valence electron states, indicated by arrows, produce fluorescence radiation at characteristic photon energies  $h\nu_2$  and  $h\nu_3$ . These transitions are sensitive to the chemical binding of the two nitrogen atoms. The ATHOS beamline at SwissFEL will allow such site-specific probing of electronic binding to be performed in a time-resolved manner after driving the system out of chemical equilibrium, e.g., with an optical laser pulse. The figure is reproduced with the permission of the publisher from A Nilsson and LGM Pettersson, *Surface Science Reports*, 55, p. 49 (2004).

strated, but its origins still remain to be investigated. The fact that many fundamental magnetic processes take place on the nanometer length and picosecond time scales, and the high magnetic sensitivity of resonant, circularly-polarized X-rays, make the ATHOS beamline at SwissFEL a versatile instrument for state-of-the-art research in magnetism. Of particular current interest are the ultrafast disappearance, creation and modification of magnetic order and the novel quantum effects which arise in two-, one- and zero-dimensional systems. The Swiss-FEL, with coherent, high-brightness, circularly-polarized X-rays at energies resonant with

the 3d-transition metal ions, corresponding to nm wavelengths, is capable of single-shot lensless imaging of nanometer-scale magnetic structures. Furthermore, the combination of high-energy, half-cycle THz pump pulses and the synchronized, sub-picosecond SwissFEL probe pulses will permit the investigation in real time of ultrafast magnetic interactions.

...→ **Following catalysis and biochemistry with soft X-rays**

Valence electrons, distributed in bonding and anti-bonding molecular orbitals, determine the chemical properties of inorganic and organic matter. Their redistribution, on the sub-picosecond time scale, is responsible for the atomic rearrangements we call chemistry. The elemental and even chemical specificity of soft X-ray spectroscopy, performed at the K-absorption edges of the light elements C, O and N and the L-absorption edges of the 3d transition metal elements Ti, Mn, Fe, and Cu provide a powerful tool to probe the valence electron distributions, and when combined with the femtosecond time resolution of the XFEL, allows real-time studies of photo-triggered chemical reactions.

...→ **Time-resolved spectroscopy of correlated electron materials**

“Electron correlation” is a dominant theme in condensed matter science, manifesting itself in, *e.g.*, metal-insulator transitions, high-temperature superconductivity and colossal magneto-resistance. On the microscopic scale, one speaks of the charge (C), spin (S) and orbital (O) degrees of freedom, each of which may show short- or long-range order, and each of which may exchange energy with the others and with the crystal lattice (L). Important correlation effects can occur in systems with partially-filled electron shells, such as those of 3d-transition metal ions, with anisotropic, quasi-localized character. Vast amounts of experimental and theoretical work have been published on electron correlation, triggered largely by the discovery of high-temperature superconductivity in 1986. Phase diagrams of many interesting materials have been investigated in detail, and numerous theories of the microscopic charge-spin-orbital-lattice interactions have been proposed. Much has been achieved, but much is still unclear. There is increasing evidence of the importance of nanoscale inhomogeneities and

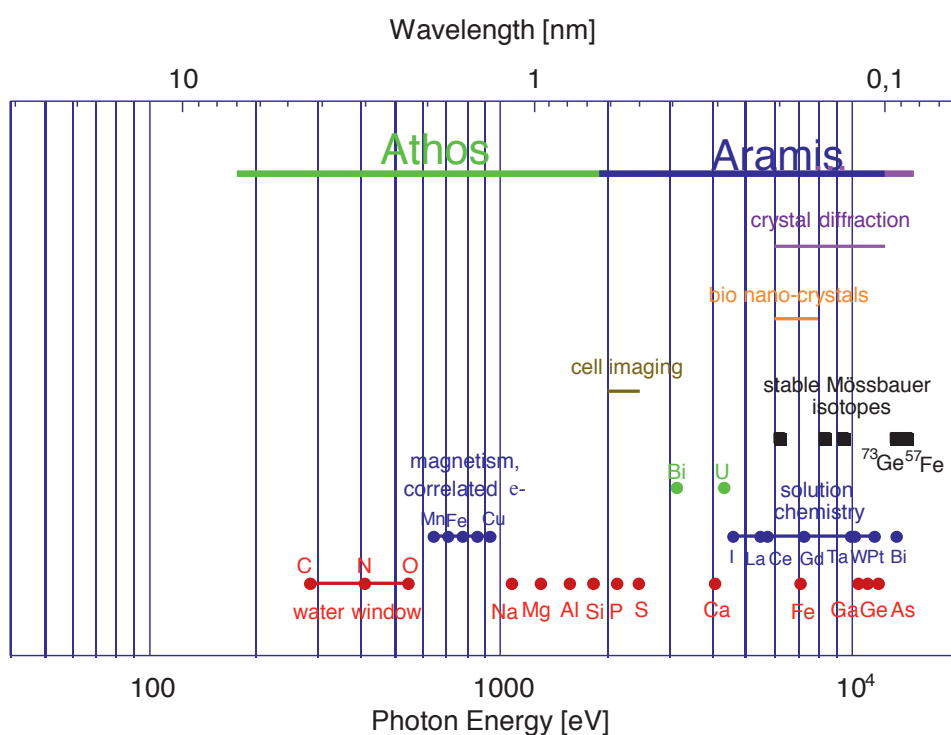


Fig. 1.6.2: An overview of photon energies accessible with the SwissFEL beamlines, and the corresponding areas of application.

fast fluctuations in correlated electron materials – indicating the important role that the ATHOS beamline at SwissFEL will play. Furthermore, it has been suggested that the chicken-or-egg problem, of determining the cause and effect relationships among the C, S, O and L subsystems, may best be approached with pump-probe time-resolved spectroscopy: one pumps energy into a particular degree of freedom and measures the time required for a response to appear in the others.

#### ...✦ **Non-linear X-ray optics**

The first optical laser emitted light in 1960, producing high-intensity coherent radiation. This opened the now vast field of non-linear optics, including effects such as sum and difference frequency generation, self-focusing, solitons and stimulated Raman scattering. Some fifty-five years later, the X-ray free electron laser has the potential of extending these effects to the soft X-ray regime. An important possible advantage of such an extension would be the ability, by using element-specific core excitations, to excite and probe matter in a highly efficient manner at pre-determined atomic sites. The various options to enhance and manipulate the longitudinal coherence of the ATHOS pulses will greatly facilitate the development of the field.

# 2 Design strategy and parameter choice

## 2.1 Overview and design parameters

The design parameters are defined so that they correspond to the specifications required to fulfil the experimental programme of the Athos Science Case Report [3]. The design parameters of the machine for the Athos undulator line lasing at 250 eV and at 1900 eV are summarized in Tables 2.1.1 (electron beam output parameters) and 2.1.2 (photon beam output parameters). There are two nominal operation modes at 200 pC and 10 pC. Five additional special operation modes (optical klystron, high brightness, TW pulse, large bandwidth, 2 colors) are also foreseen (see Table 2.1.2). These modes are obtained by manipulation of the electron bunch in the Athos undulator line but without changing the bunch parameters at the exit of the Athos linac. The photon energy range of Athos can be tuned from 250 eV to 1900 eV (0.65 nm to 5 nm wavelength) by adjusting the energy of the Athos linac (+/- 0.25 GeV) in addition to a variation of the extraction energy at the switchyard between 2.9 GeV and 3.15 GeV (Figure 2.1.1).

The operation modes listed in the Table 2.1.2 represent the modes which triggered interest by the user community at present but are not fully exhaustive. For example attosecond regime of operation could be also achieved in Athos as it is plan in Aramis. On the other hand, most of these operating schemes have not been demonstrated yet and are based on simulations and / or tests done in other institutes.

The design parameters of SASE operation of the soft X-ray beamline Athos are shown in Table 2.1.3 for the long-pulse operation mode (200 pC). The electron beam parameters required to achieve these FEL performances are the same as those in Table 2.1.1. In this beamline, the wavelength tuning from 250 eV to 1900 eV is carried out by continuous variation of the electron beam energies at output of the Athos Linac from 2.65 GeV to 3.4 GeV and by varying the undulator K value.

With a total length of about 550 m (from gun to undulator end), the SwissFEL facility can be divided into sections, as follows:

- Gun, Booster 1 and 2
- Bunch Compressors 1 and 2
- Linacs 1, 2 and 3
- Switchyard and collimator
- Aramis Undulator line
- Athos Undulator line (with Athos Linac)

Results from simulations of each of these sections is described in [15]. As discussed in Chapter 1, it is planned to operate SwissFEL (up to the switch-yard) with two electron bunches per RF macropulse. The simulated parameters presented in [15] are also valid for the second electron bunch, assuming that inter-bunch wake-field effects are negligible.

A schematic overview of the accelerator is displayed in Figure 2.1.1.

Electron Beam Design Parameters	Nominal Operation Mode	
	Long Pulses	Short Pulses
Charge per bunch (pC)	200	10
Beam energy for 250 eV (GeV)	2.65	2.65
Beam energy for 1900 eV (GeV)	3.4	3.4
Core slice emittance (mm.mrad)	0.43	0.18
Projected emittance (mm.mrad)	0.65	0.25
Energy spread (keV, rms)	350	250
Relative energy spread (% , rms)	0.006	0.004
Peak current at undulator (kA)	2.7	1.6
Bunch length (fs, rms)	25	2
Bunch compression factor	125	533
Repetition rate (Hz)	100	100

Table 2.1.1: Design parameters of the electron bunch at output of Athos linac.

Table 2.1.2: Operation modes of Athos (corresponding electron beam parameters are the same as in Table 2.1.1).

Operation mode	Pulse energy at saturation	Number of photons at 1 nm	Pulse length (rms)	Bandwidth	Comment
SASE (200 pC)	> 1 mJ	$5 \cdot 10^{12}$	30 fs	0.1–0.4 %	
SASE (10 pC)	> 50 $\mu$ J	$2.5 \cdot 10^{11}$	2 fs	0.1–0.4%	
Optical Klystron	As SASE	$5 \cdot 10^{12}$	As SASE	As SASE	More length for taper
High Brightness SASE	As SASE	$5 \cdot 10^{12}$	As SASE	0.02–0.04%	Can also be configured for pulse trains
TW power pulse	> 1 mJ	$5 \cdot 10^{12}$	~ 1 fs	1% FWHM	200 pC bunch
Two colors	$2 \times > 50 \mu$ J	$2 \times 2.5 \cdot 10^{11}$	$2 \times 2-10$ fs	0.2%, tuning range: factor 5	Based on 200 pC
Large Bandwidth	> 0.5 mJ	$2.5 \cdot 10^{12}$	30 fs	> 10% FW	200 pC only

Expected Parameters	Large Gap High Energy	Small Gap High Energy	Large Gap Low Energy	Small Gap Low Energy
Electron beam energy (GeV)	3.4	3.4	2.65	2.65
Undulator period (mm)	38	38	38	38
Undulator parameter K	1.0	3.6	1	3.6
Undulator module length (m)	2.0	2.0	2.0	2.0
Undulator section length (m)	2.8	2.8	2.8	2.8
Average b-function (m)	7	7	7	7
FEL photon energy (eV)	1900	390	1170	235
Saturation length (m)	36 (*)	20	31	16
Saturation pulse energy (mJ)	0.8	1.6	0.8	1.4
Effective saturation power (GW)	10	19	9.8	17.7
Number of photons at saturation	$2.8 \times 10^{12}$	$2.6 \times 10^{13}$	$4.4 \times 10^{12}$	$3.9 \times 10^{13}$
Bandwidth (% rms)	0.25	0.5	0.27	0.55
Pulse length (fs, rms)	30	30	30	30
Beam radius ( $\mu$ m, rms)	20	20	22	24
Beam divergence ( $\mu$ rad, rms)	2.6	12.0	4	18

Table 2.1.3: Design parameters of the photon pulses from the Athos beamline in SASE operation (corresponding electron beam parameters are the same as in Table 2.1.1).

(\*): The Athos beamline has a total effective length of 32 m. The value shown in the Table (36 m) indicates the total length required for SASE operation (§ 2.4).

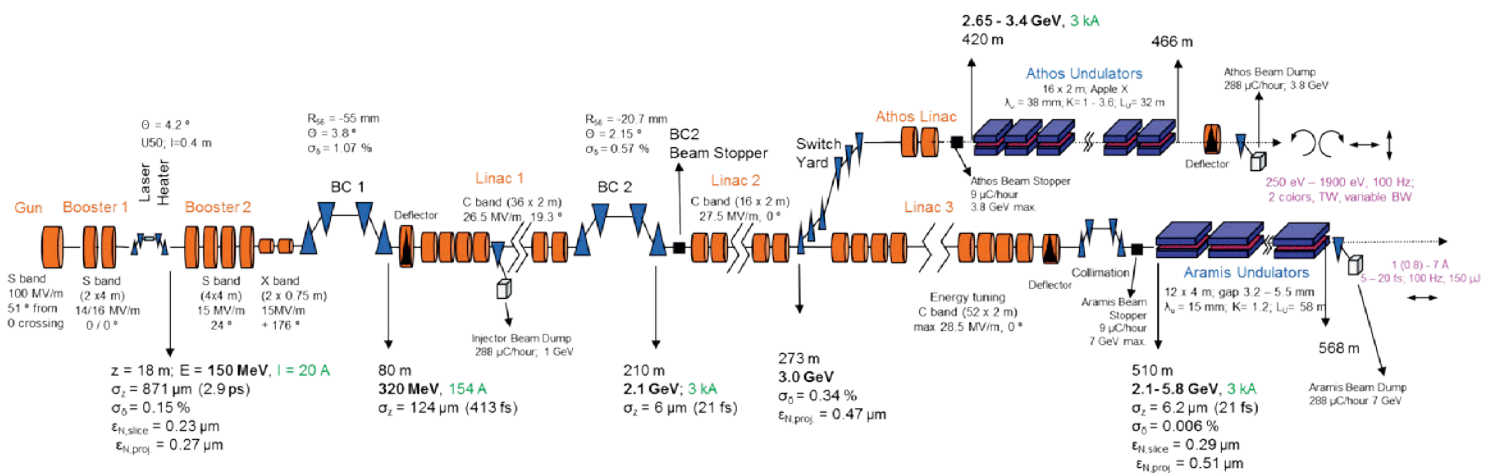


Fig. 2.1: Schematic of the SwissFEL Accelerator and FEL with the simulated beam parameters for the 200 pC operating mode.

## 2.2 Athos electron beamline

### 2.2.1 Switchyard

The switchyard which extracts the beam from the main linac and injects it into the Athos undulator beam line has multiple purposes:

1. Allow for a separation of about 3.75 m to place Aramis and Athos in parallel
2. Allows for some R56 to tune the beam for Athos slightly different than for Aramis
3. Close the vertical dispersion, arising from the resonant kicker in the linac 2 beam line of the switchyard.
4. Allow for energy collimation for the Athos beamline
5. Allow for adjustable phase advance between the two bending section to compensate for the CSR kicks
6. Align the beam tilt and energy acceptance by means of sextupoles.
7. Remove the residual chirp with the dechirper
8. Select parts of the beam for lasing with slotted foil.

As such the configuration of the switchyard is most likely the most complex part in setting up the machine.

### 2.2.2 Optics

The beam optic is the key parameter to control and configure the switchyard. The nominal beam optic functions of the Athos lattice are shown in Figure 2.2 to Figure 2.4 in the case of SASE operation. These functions might slightly change depending on the operation mode.

Strongest contribution to the R56 arises from the value of the dispersion at the 1 degree bending dipole SAT-SY01-MBND200, which can be controlled by the quadrupoles in SATSY01. Some flexibility in the R56 is given to vary its value from some decompression to a slight compression. Due to space constraint the configuration of SATSY01 also influences the evolution of the vertical dispersion, which arises from the resonant kicker in the main linac beam line. The lattice should allow for sufficient flexibility to close the dispersion in the vertical dogleg in SATSY02. The two quadrupoles within the vertical dogleg are used to match the dispersion and derivative of it to zero while preserving the height adjustment of 1 cm, so that the beam line is back at 1.2 m height.

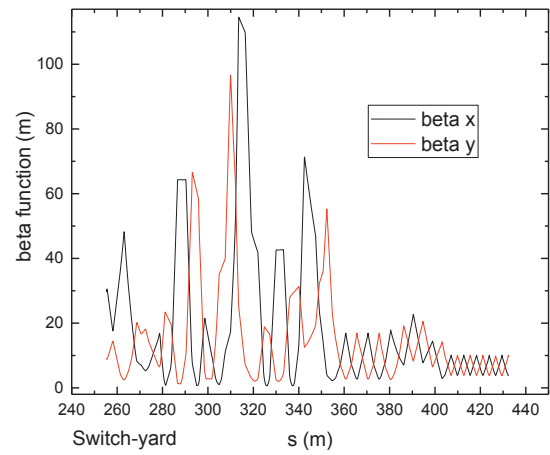


Figure 2.2: Beta function of the Athos lattice starting from the switchyard.

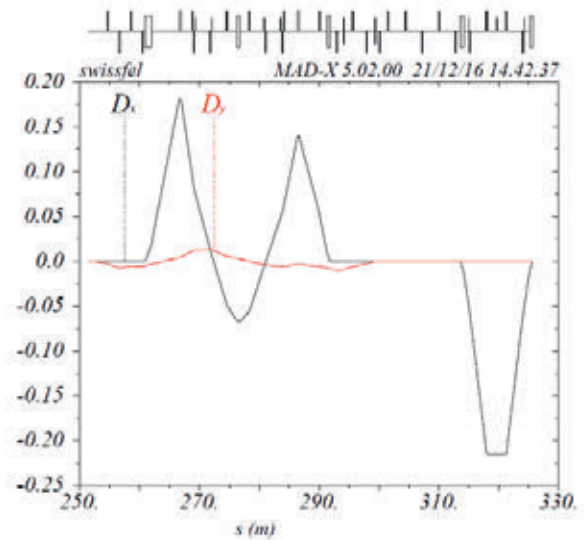


Figure 2.3: Dispersion from S20SY01 to SATCL01 (until energy collimator section).

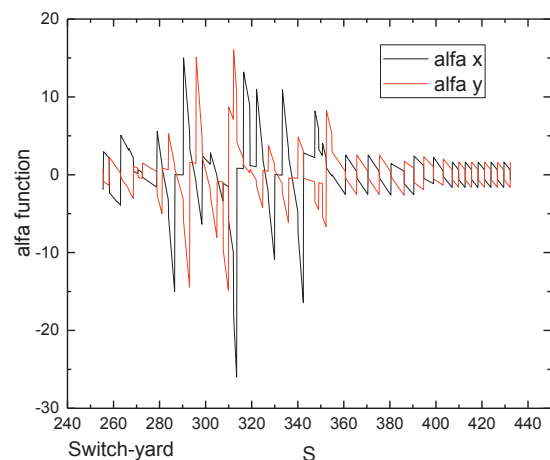


Figure 2.4: Beam optic alfa function of the Athos lattice starting from the switchyard.

The most critical aspect of the switchyard is the degradation by the CSR within the bending magnets, in particular in the septum magnet, which is significantly longer for a 2 degree bend than the AFBC3 type bending magnet at SATSY01-MBND400. To minimize the impact there are three knobs to optimize:

1. Keep the betatron function in the horizontal plane small in all dipoles, preferable below 5 m
2. Optimize the betatron phase advance between SATSY01 and SATCL01 so that the CSR kicks have opposite kick and cancel each other.
3. If FEL operation permits inject with a slightly longer bunch by shifting the acceleration phase of the second bunch in Linac 1 slight more on-crest.

Because most of the switchyard has non-vanishing dispersion it is also the ideal location for longitudinal phase space manipulation. In the section SATCL01 the energy collimator is placed to yield a controlled loss of the beam in the case the central beam energy changes in an uncontrolled manner, such as a failure of an RF station in Linac 2. Note that for a failure of more than one RF station the aperture of the septum is not sufficiently large to guarantee a safe transport. Here most of the particles are lost in or right behind the septum magnet.

Compared to Linac 3 the Athos switchyard misses the wakefields of 11 C-band RF station to yield the same wakefield budget and thus the removal of the energy chirp from the last compression stage. This is achieved by the dechirper in SATDI01 and SATCL02. A detail description is given in the next section.

The quadrupoles in SATCL01 are configured to normally close the dispersion but they can be changed to leak out dispersion out of the switchyard. This is one possible method to tilt the beam for various modi of operation such as the two color mode. However this requires that the dechirper is disabled because without a chirp the beam is not tilted despite a non-zero dispersion value.

In the dispersive region a slotted foil can be placed to select parts of the bunch for lasing. To be independent of the dechirper this has to be done in the first section SATSY01, close to the first dipole, where the dispersion is the largest. For the same reason the correction of the beam tilt has to

be done before the dechirper. Corrector sextupoles are placed to control the second order tilt of the beam misalignment, while the first order tilt is done with some leaked first order dispersion, actually using the same mechanism to generate the tilt as described.

### 2.2.3 Dechirper

A dechirper is a device used to control wakefields by means of parallel plates with micro-structured surfaces (Fig. 2.5). By adjusting the micro structure geometry and the gap between the plates the magnitude of the wakefield can be controlled. The set-up foresees two identical pairs of plates, which are rotated by 90 degree with respect to each other, to compensate asymmetries of the wakefield, which otherwise would degrade the beam quality of the electron bunch in SwissFEL. The gap between two surfaces should be controllable down to one millimeter for the strongest wakefields. More details on the device parameters are given in chapter 3. These two identical pairs of one meter length each are then followed by 3 dechirpers with a square section that is to say 4 identical micro-structured plates with a fixed aperture. The fixed dechirper are about 2 m long.

Wakefields offer an automatic synchronization of the fields with the electron bunch arrival time, thereby avoiding the synchronization problem of electronically powered devices like RF cavities. Although no net energy gain can be obtained, there is a control on the local wakefield amplitude based on the source of the wakefields, such as corrugated walls. They offer a reliable control on the wakefield amplitude and periodicity with the specification of the corrugation periodicity and depth, which allows the tailoring of the wakefield according to the needs for a beam manipulations on femtosecond time scales, as it is required for removal of the energy chirp of the last compression stage.

#### *Dechirper principle:*

The electron beam is controlled by the interaction with electric and magnetic fields. While the fields of magnets are static and guide and focus the beam independently of its injection time, the manipulation with the time-dependent RF- and laser fields depend critically on the synchronization of these sources with the electron beam. A compromise has to be found between low-frequency RF fields, which lack the

field amplitude to efficiently accelerate or deflect the beam, or laser fields, where the synchronization on a femtosecond level is required to avoid strong jitter in the acceleration phase.

Fields, which are generated by the bunch and act upon the bunch itself, are called wakefields and offer the benefit of providing high field strengths while being automatically synchronized to the beam itself. This is explicitly sought after in plasma beatwave acceleration projects [4] or acceleration in dielectric structures [5]. By the nature of self-interacting fields no net energy gain is possible. However energy or momenta can be transferred within the bunch with high frequency time variations which are either difficult or impossible to access for active RF beam manipulation systems. This opens up the possibility to manipulate the electron bunch distribution in a controllable manner on the femto-second time scale.

Although the design of FEL facilities is aimed to reduce the magnitude of wakefields in the machine to a minimal level, they are actually used in facilities such as LCLS [6] or Swiss-FEL [3] to remove the residual energy correlation along the bunch after the last compression stage before injecting the beam into the FEL for the smallest bandwidth of the FEL signal and thus the highest spectral flux. The limitation is that the wakefields, generated by the cavities of the accelerating RF structures [7], are fixed and thus link the energy chirp at the bunch compression with the overall length of the remaining accelerating sections. Recent projects such

as the Korean FEL PAL [8] are trying to break this correlation with controllable wakefield sources [9], which are called “dechirper” with reference to the correlated beam energy along the bunch often referred to as a chirp.

#### 2.2.4 Post-Undulator Transverse Deflector

Unlike the Aramis beamline, where in the energy collimator the horizontal slice emittance and alignment as well as the longitudinal phase space can be measure with a single deflection direction, the Athos beamline requires the ability to streak into both directions, because the only significant dispersion occurs in the beam dump, which is in the vertical direction. The required streaking in the horizontal direction would obscure the measurement of the horizontal slice parameters which are more sensitive to degradation and misalignment because the entire compression scheme is acting in that plane.

An elegant solution is the development of a transverse deflecting structure in the X-band frequency range, which is fully cylindrically symmetric and has degenerated modes for deflection in the two transverse directions (see section 3.2). Solely by manipulating the phase advance at the RF input couplers a given direction can be selected.

The location is between the last Athos undulator section at SATUN22 and the dump dipole. In total, a length of 26 m is available. To allow for matching into the TDS structure for best resolution and sufficient betatron phase advance for emittance measurements at a high resolution screen right before the dipole, strong quadrupoles are placed in this section. Upstream the TDS, there are 6 QFF quadrupoles and there are 5 QFM quadrupoles downstream. Quadrupoles of the type QFD are not sufficiently strong enough to fit the layout within the given 26 m. The vacuum chamber aperture is kept at 16 mm for most of the section.

The deflection can be configured to measure the longitudinal phase space at each shot in the dispersive part of the beam dump. Following the experience of LCLS this give a single shot measurement of the FEL performance which is strongly correlated to the mean energy change and energy spread increase of each slice. A resolution of 1 fs is sufficiently high to obtain multiple slices and to construct a valid envelope of the FEL pulse.

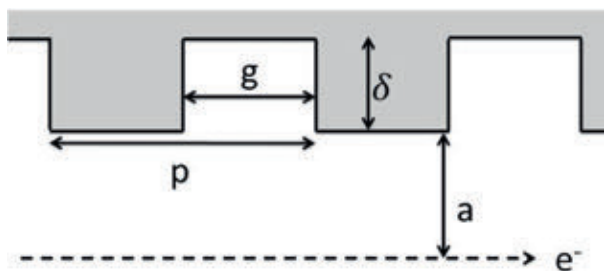


Fig. 2.5: Geometry of a corrugated wall ( $p$ ,  $g$ ,  $a$  and  $\delta$  have typical values between 0.1 and 1 mm).

### 2.2.5 Seed-Laser Consideration

Some operation modes foresee an external laser source to manipulate the electron beam prior to the injection into the FEL or to overlap an HHG signal. The former requires the coupling of the laser field to the electron beam similar to an undulator. However with an expected wavelength of up to 2 microns, the required undulator parameter and period are large to be resonant at 3.0 GeV, e.g. a period of 50 cm and a K-value of 23.4 would fulfill the requirement.

The length of the energy modulation is the convolution of the pulse length in terms of radiation wavelength and the number of undulator periods. For the case that only one slice is selected (see above) it is mandatory to use only a single cycle seed pulse and a single period undulator on the cost of more radiation power. In fact, the case of a single period modulator has a very broadband resonance such that actually a single dipole of similar extension can be used, such as the last dipole SATCL01-MBND300 of the switchyard. In addition it allows for a direct in-coupling of the laser beam in line with the remaining beamline and has a better coupling due to the fact that the transverse motion of the electrons with respect to the laser field propagation axis is only one directional and does not change signs. In fact the coupling is almost constant for a large frequency range well below the critical frequency of the bending magnet, similar to that of transition radiation. We summarize that no additional hardware in the beamline is needed to modulate the electron beam beside the actual laser system and its beam transport.

### 2.2.6 Undulator line parameters

The SwissFEL goal is to provide FEL radiation which spans the wavelength range from 1 Å to 5 nm, with a compact design. A natural cut in the wavelength is at around 7 Å, because the optics to transport the radiation differs significantly for longer or shorter wavelengths. Thus the hard X-ray beamline Aramis covers the wavelength range from 1 to 7 Å. For the soft X-ray beamline Athos, a tuning range from 0.65 to 5 nm is ensured by varying the electron beam energy from 2.65 GeV to 3.4 GeV. This wavelength range corresponds to photon energies ranging from 250 eV to 1900 eV so that the binding energy of the K shell electrons of carbon atoms C (280 eV) and silicon Si (1850 eV) is covered by the Athos line. The beam energy at the switch yard kicker magnet needs

Beam energy	3.4 GeV	2.65 GeV
Peak current	2.7 kA	2.7 kA
Charge	200 pC	200 pC
Energy spread	350 keV	350 keV
Emittance	0.43 mm.mrad	0.43 mm.mrad
Undulator period	38 mm	38 mm
Undulator parameter	1.0	3.6
Undulator module length	2.0 m	2.0 m
Undulator section length	2.8 m	2.8 m
Average $\beta$ -function	15 m	15 m
Wavelength	0.65 nm	5.2 nm
Saturation length	36 m	17 m
Saturation pulse energy	0.9 mJ	1.4 mJ
Effective saturation power	10 GW	17 GW
Photons at saturation	2.8.1012	3.9.1013
Bandwidth	0.23 %	0.56%
Pulse length	30. fs	30 fs
Beam radius	19 $\mu$ m	25 $\mu$ m
Beam divergence	2.6 $\mu$ rad	18 $\mu$ rad

Table 2.2.1: Performance of the Athos soft X-ray beamline in SASE Operation.

to be variable between 2.9 GeV and 3.15 GeV and the Athos Linac (+/- 0.25 GeV) is used to accelerate to 3.4 GeV or decelerate to 2.65 GeV (see Fig. 2.6).

## 2.3 Operation Modes

### 2.3.1 Normal Operation

#### 2.3.1.1 SASE Operation

Normal SASE operation parameters define the baseline parameters of the Athos beamline. These parameters were already given in section 2.1. The presence of the magnetic chicane gives however the possibility to operate the Athos line by using the optical klystron effect (see below). This effect, if successful, will improve the performance of the line in comparison to the standard SASE operation.

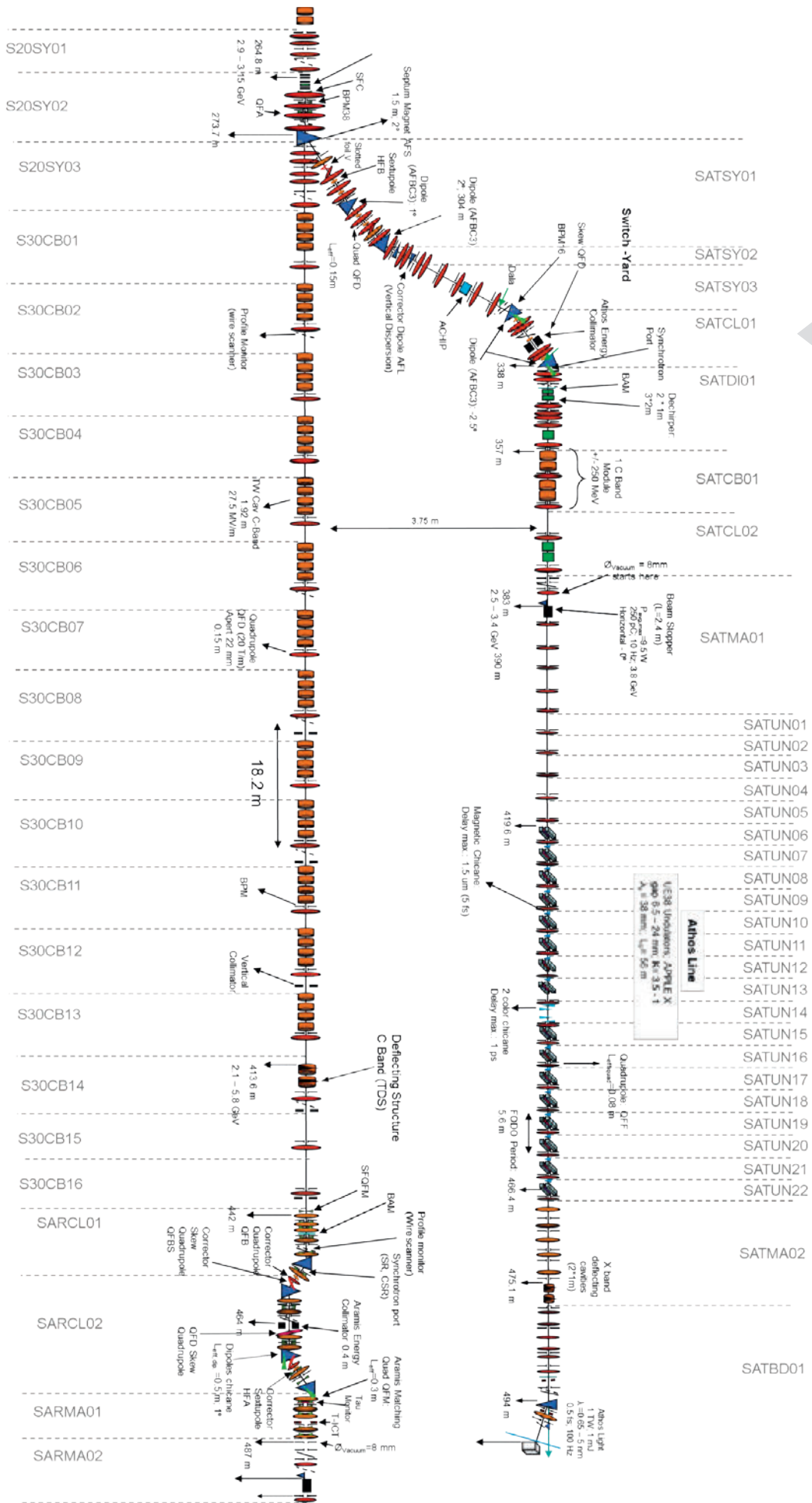


Fig. 2.6 Schematic of the SwissFEL Switch-Yard and Athos FEL (0.65 to 5 nm).

### 2.3.1.2 Optical Klystron

In the undulator, electrons start to emit spontaneous synchrotron radiation leading to a velocity modulation. The electric field of the radiation together with the magnetic field of the undulator produces a longitudinal force on the electrons that is a periodic function of position. This force tends to bunch the electrons at distances  $\lambda r/2$  (where  $\lambda r$  is the output wavelength) leading to coherent synchrotron emission (SASE emission). The bunching can be made more rapid by introducing a magnetic dispersive element (where faster (slower) electrons move on a shorter (longer) path). The optical klystron mode consists then in speeding up the microbunching process taking place in the SASE process [8]. In Athos, a permanent magnetic chicane (the magnetic dispersive element) is installed between every undulator segment [5,12]. The enhancement of the bunching reduces the required undulator length to reach saturation (see Fig. 2.7). This extra length of available undulator can be used to do tapering in order to reach higher FEL power or it can be used to generate another color (see two colors operation mode).

Figure 2.5 shows the FEL amplification for the normal SASE case and for the optical klystron case where short permanent magnet chicanes are considered between every undulator segment.

The dispersive section and undulator parameters are indicated in Table 2.4.3.1 and Table 2.4.3.2.

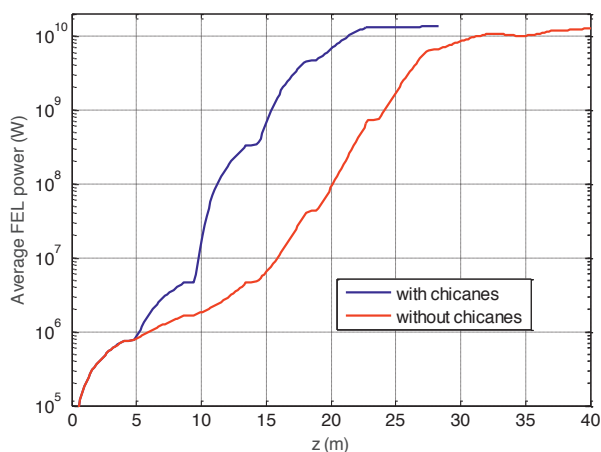


Figure 2.7: FEL power in normal SASE operation (without chicanes) and in optical klystron mode (with chicane) [5].

## 2.3.2 Coherence Control

### 2.3.2.1 Self-Seeding

Despite a self-seeding chicane is not part of the baseline design of Athos, it is possible to install such a chicane by using two consecutive undulator slots. This would give more than 4 meters of beamline length to accommodate a self-seeding chicane with a monochromator. In any case, the strategy is to first get operation experience with the High Brightness SASE mode of operation before to build a self-seeding chicane. Indeed the bandwidth of the High Brightness SASE mode is only a factor 2 larger than with a self-seeding chicane (see below).

### 2.3.2.2 Phaselocked Double Pulses

One special mode of self-seeding provides two pulses of short duration, where the separation can be freely tuned while remaining phase-locked. Beside the mode-lock operation (see further down) the most prominent way to achieve this is in a modified configuration of self-seeding. To select two regions in a bunch, which are lasing, a double slotted foil can be inserted into the dispersion region of the Athos switchyard right after the septum magnet. In a V-shape configuration of the foil the separation is controlled by the height of the foil.

However the challenge is to provide the seed signal. For that the beam is split in half. The tail part is providing the SASE signal which is then filtered by the self-seeding chicane to seed the two slices in the head of the second stage. To obtain a stronger seed signal the tail part is driven into saturation while the head is not amplifying the radiation

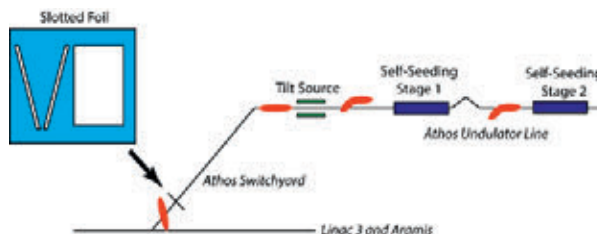


Figure 2.8: Schematic layout for phase-locked pulses in Athos.

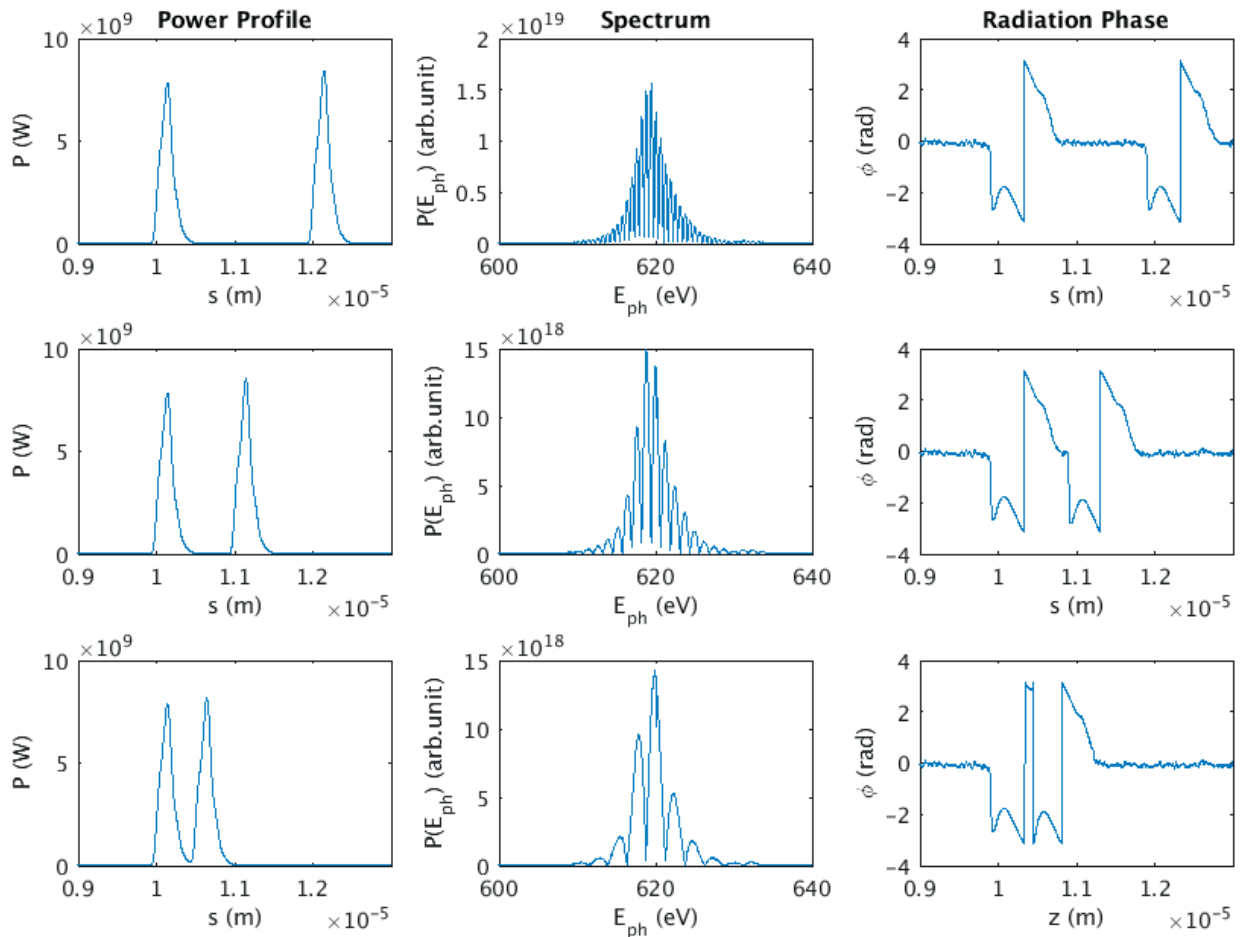


Figure 2.9: Power profile, spectrum and radiation phase (left to right plot) for various separation of the two pulses.

due to an introduced tilt (either generated by dispersion or wakefield source). The schematic configuration is shown in Figure 2.8.

With the coherence of the seed signal the FEL pulses are locked in phase as it can be seen in Figure 2.9. The simulation assumed a seed level of 1 MW in the second stage, however the phase locking is still preserved with a seed level down to 10 kW before the intrinsic shot noise becomes dominant. With the expected performance of self-seeding this threshold should be easily exceeded for almost all shots (more than 95%) despite the negative exponential proba-

bility distribution at the exit of the monochromator in the self-seeding chicane.

There are different methods to obtain the tilt. In general the cleanest solution would be to have two wakefield sources of same type and specification, where the second is placed directly before the second stage with the constraint of having a betatron phase advance in the tilting plane of 180 degrees or an additional multiple of 360 degrees. However LCLS has recently demonstrated this advanced self-seeding with just a single tilt source prior to the undulator beam line.

### 2.3.2.3 High Brightness SASE

The magnetic chicane between every undulator segment can also be used to increase the cooperation length of the FEL process which would lead to a reduction of the bandwidth. In the SASE process individual bunch slices starts to

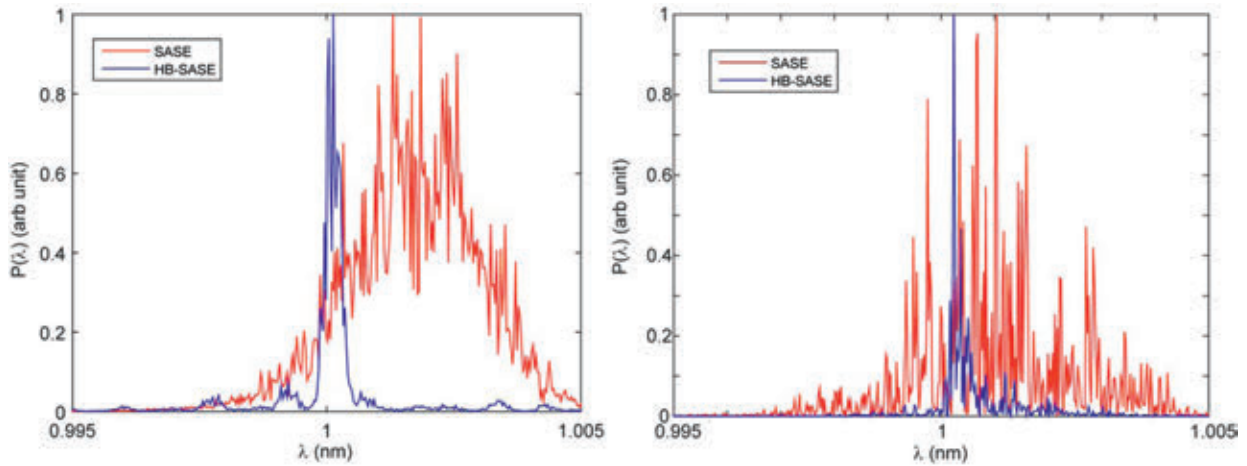


Figure 2.10: Output spectra for an undulator length of  $L=1.5$  m in SASE operation or in the high brightness SASE mode averaged over 10 pulses (left) and for a single shot (right). [12]

lase independently one to each other leading to a spiky FEL intensity time profile. The duration of these spikes corresponds to the cooperation length: slippage length of electrons over radiation in one gain length. If magnetic chicanes are used to delay electrons then a given radiation slice will slip over a longer portion of the bunch. The slippage length becomes longer and thus the FEL spike duration becomes longer. The bandwidth gets then reduced, thus reducing the FEL bandwidth.

Figure 2.10 illustrates the potential reduction of bandwidth when operating in the High-Brightness regime. The Bandwidth can be reduced by up to a factor 10 in comparison to normal SASE operation.

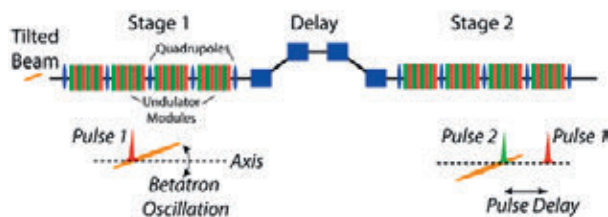


Figure 2.11: Schematic configuration of two color operation.

### 2.3.3 Bandwidth and Frequency Control

#### 2.3.3.1 Two Color

One mode of operation, which is in high demand from the users, is the “two color” mode which provides two pulses with full control on relative time delay and central frequency. The most flexible approach is to split the undulator line into two sections of 8 undulator modules each with a delaying chicane placed in between [11]. Each section is tuned to one of the two photon frequencies and the delay is controlled with the strength of the delay. To restrict the pulse length and to guarantee that the electron bunch is not completely exhausted by the saturation in the first stage the beam is tilted by means of leaked dispersion or transverse deflecting structure. The conceptual set-up is shown in Figure 2.11.

With the given parameters of Athos the photon energy is tuned with the undulator parameter in the range of  $K=1$  to  $K=3.5$ , which corresponds to a range of a factor of 4.75. The delay is up to 1 ps and if the second pulse is generated by the head of the bunch it can be tuned from some time before (about 50 fs) to well after (950 fs). The length of the pulse is defined by the degree of tilt and the strength of the focusing, which can be controlled with some slight rematching in each section individually.

The limiting factor arises from the need to saturate within 8 undulator modules, which naturally excludes higher photon energies. The distributed optical klystron is used to shorten the saturation length and thus extending the tuning range. In Figure 2.12 the performance at 1 keV is shown for various beam parameters.

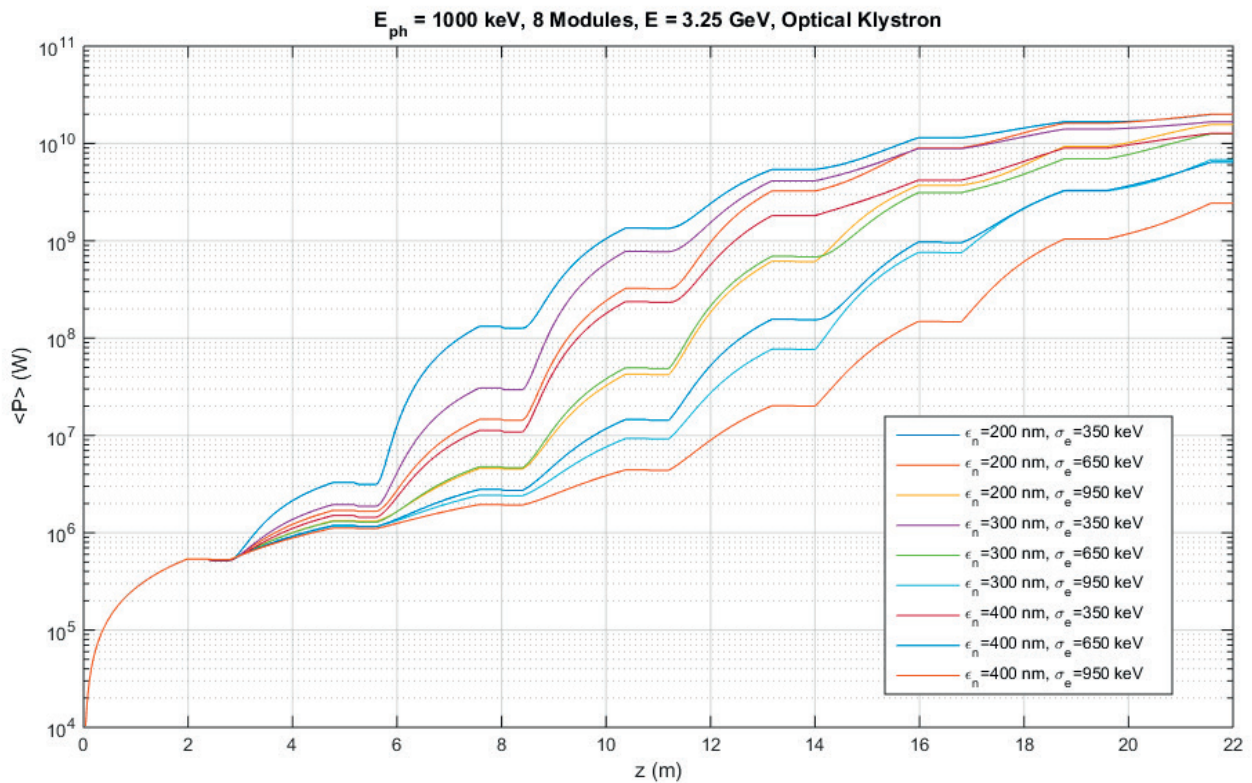


Figure 2.12: FEL performance at 1 keV photon energy for various electron beam parameters.

Even for parameter worse than the design parameter with e.g. a slice emittance of 400 nm and an energy spread of 950 keV saturation is reached, where the strongest dependence is on the energy spread. With nominal energy spread and optical klystron it can be expected that two color can be provided up to 1200 eV.

### 2.3.3.2 Large Bandwidth

In a transverse gradient undulator (TGU) there is a dependence of the undulator field on the transverse position. A transversely-tilted beam traveling through a TGU will produce broadband XFEL radiation (Figure 2.13) [16] [16].

All the electrons need to produce XFEL radiation and the transverse positions of the electrons must be as constant as possible in order for a longitudinal slice to radiate at the same frequency. Therefore all electrons comprising the beam should travel parallel along the undulator axis. This is

achieved if the beam has a transverse tilt only in offset (not in angle) at the undulator entrance and in the absence of external focusing all along the undulator lattice.

The transverse tilt of the beam can be generated with different methods, all relying on standard components of XFEL facilities: applying a transverse deflecting RF structure to streak the beam [17], introducing dispersion to an energy chirped beam [18], or using the transverse wakefields [19] of the accelerating or any other structures of the beamline. The transverse gradient can easily be achieved with the

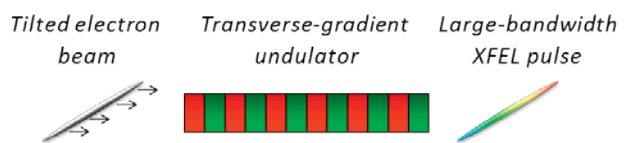


Figure 2.13: Sketch to show the working principle of the proposed method: an electron beam with a transverse tilt traveling through a TGU generates large-bandwidth XFEL radiation.

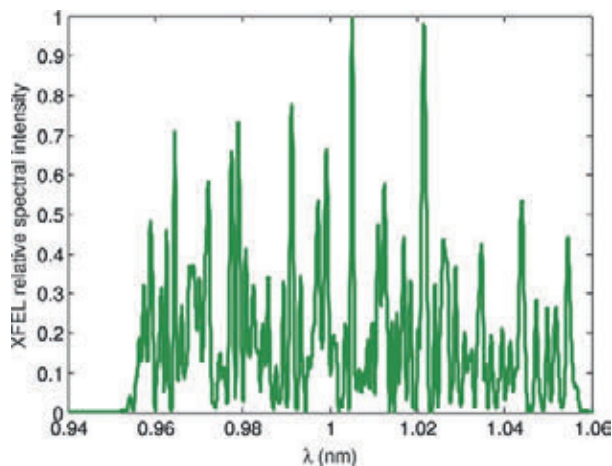


Figure 2.14: Example of a simulated spectrum for an XFEL pulse with a total bandwidth of 10%. It is obtained with a tilt amplitude in offset of 125 and a TGU gradient of 48 m<sub>-1</sub>.

particular UE38 undulator mechanics where left and right gap can be set to different K values leading to a transverse magnetic field gradient (see section 3.5 and [7]).

Figure 2.14 is an example of a GENESIS simulation of the FEL spectrum obtained with a tilted beam at 3GeV traveling through 40m of undulator line without external focusing. This simple method could generate spectral bandwidth as large as 10 %.

### 2.3.4 Power and Pulse Length Control

#### 2.3.4.1 Terawatt-Attosecond Mode

In this mode of operation a short and high-power XFEL pulse is generated by suitably correcting the trajectory and delaying a tilted electron beam between undulator sections [10]. Due to the tilt only a small portion of the beam is on the good trajectory region which produces efficient SASE effect. Once this beam portion saturates, the chicane between undulator segment is used to shift the bunch (delay and offset) so that a new portion of the bunch comes on the undulator axis. These fresh electrons will amplify the XFEL pulse produced in the previous segment. By this way, all the electrons can contribute to enhance a short XFEL pulse in the superradiance regime. The scheme is illustrated by the Figure 2.15.

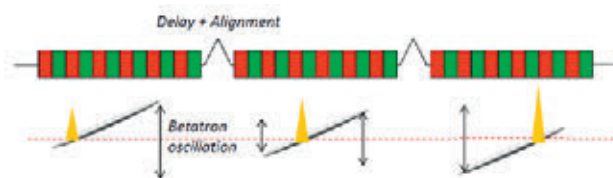


Figure 2.15: Schematic of the tilted beam which is delayed and shifted horizontally at each chicane so that always fresh electrons overlap the XFEL pulse (in yellow).

Figure 2.16 represents a simulation of this operation mode with 8 undulator section and 7 chicanes. After each section the FEL pulse is amplified due to reach power above 1 TW for a pulse duration of 0.34 fs FWHM at a wavelength of 2 nm.

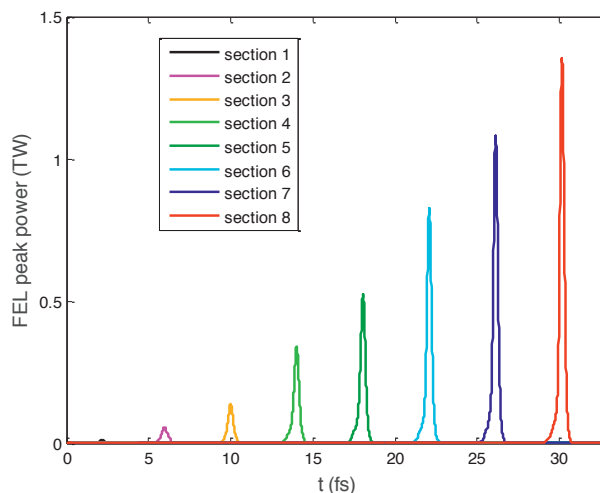


Figure 2.16: FEL radiation profile after each undulator section for L=2m and a tilt of 3 mm in offset.

#### 2.3.4.2 Slotted Foil

A few other methods based on slotted foils do exist and could also produce FEL pulse with TW power and sub-femtosecond duration. The method foreseen for Athos is described in details in [20]. In addition to chicanes between undulator, a foil with a series of slits intercepts the beam in the bunch compressor. The bunch will develop a longitudinal

nal structure with good slice (where a slit was present) and spoiled parts. When this train of good slices enters the undulator, the chicanes are used to delay the slices such that only one radiation pulse gets amplified by all fresh slices.

This method is a bit less efficient (less electrons contribute to the FEL pulse) than the scheme proposed in the previous section.

### 2.3.5 Timing Control

The following operation modes are driven by an external laser signal. As for now this is not part of the baseline design though the possible implementation is foreseen and accordingly space reserved in a room next to the Athos beam-line. The interaction with an external seed has the benefit to provide a more stable time difference between pump and FEL signal, if both are derived from the same laser. To get this benefit the laser signal must be shorter than the electron bunch length because otherwise the FEL signal is still locked by the electron bunch arrival time.

#### 2.3.5.1 Slicing

One proposed method to lock an external laser seed with the FEL pulse is to manipulate the electron beam in a way that only a certain part of it will lase. One idea is the enhanced SASE scheme, where an induced energy modulation is converted to a current modulation, which then drives the FEL amplification. While this would work for hard X-rays in the soft X-ray regime the problem is the dominant slippage. Radiation escapes in the forward direction the current spike while significant less radiation slips into the spike. This effective damping reduces the growthrate and no good contrast ratio to the SASE background can be achieved.

The solution is to exclude the bunching and uses the imprinted energy modulation for slicing. In normal configuration a strong chirp suppresses the lasing process because the radiation field slips into parts of the electron bunch which has different mean energy and therefore is not in resonance with the field anymore. This can be compensated by a change in the undulator gradient, synchronized to the slippage velocity so that the resonance condition for the spike is preserved and can be amplified further. At the same time, parts of the bunch which have no energy chirp or

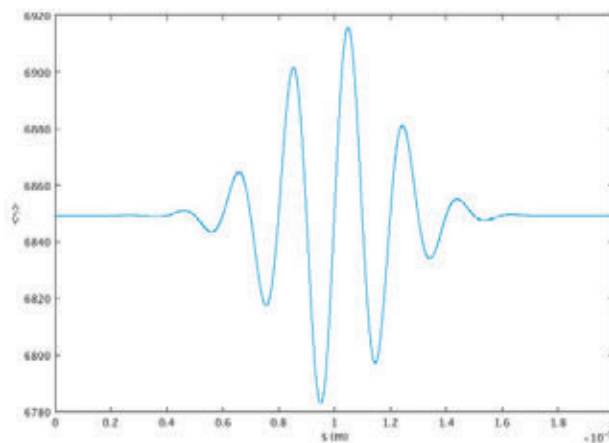


Figure 2.17: Energy modulation of the electron beam at the undulator entrance.

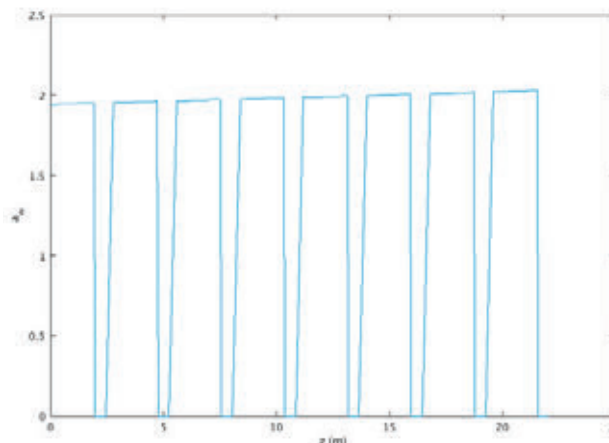


Figure 2.18: Undulator field tapering to preserve resonance for the part in the beam with the largest rising energy chirp.

modulation or a chirp with non-matching slope will not contribute to the FEL process. A working energy modulation and corresponding undulator taper for an electron beam at 3.5 GeV and tuned to 2 nm is shown in Figure 2.17 and Figure 2.18.

Better performance is achieved for a positive taper because a slight negative taper has still an enhancing effect on the FEL performance, which would be needed to overcome. The

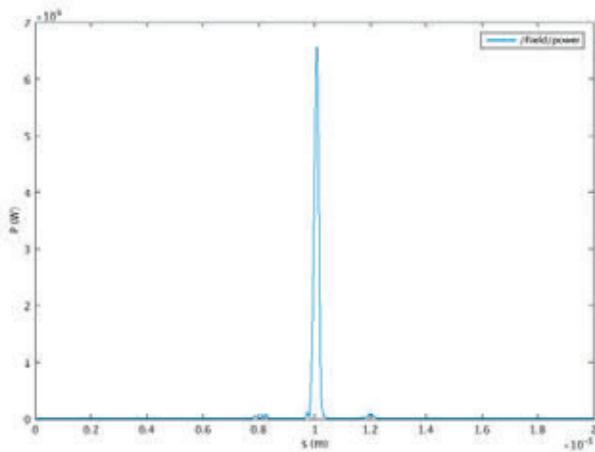


Figure 2.19: Radiation pulse at undulator exit.

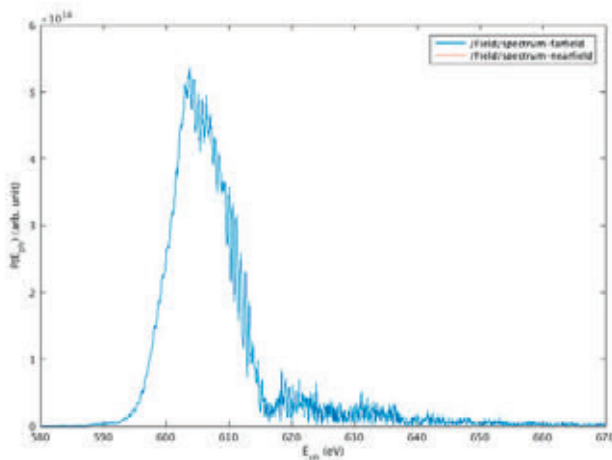


Figure 2.20: Spectrum of FEL pulse at undulator exit.

resulting pulse is shown in Figure 2.1Figure 2.9. There are some satellite pulses visible, which peak values are at the percent level of the main pulse. They could be further suppressed when the modulation pulse is even shorter, reducing the positive chirp one wavelength before and after the main chirp of the sine phase stabilized pulse. These smaller peaks have also caused some small interference in the spectrum, as shown in Figure 2.20. Because the pulse start at the lowest point in the energy modulation, the resonant photon energy is somehow lower and is then preserved in the slicing process. In this example the main bunch is res-

onant at 620 eV while the peak is around 605 eV. This 2.4% shift is in relative good agreement with the detuning of 1.1% for the minimum electron energy along the bunch. This detuning separates also the sliced pulse with the SASE background, where a significant part of it could be removed with a low-pass filter, if needed.

### 2.3.5.2 HHG Seed

Theoretically the simplest method for seeding is to provide an external signal with a photon energy in resonance with the FEL. However in the soft X-ray regime of Athos no such source has been demonstrated though the high harmonic generation (HHG) in gases could be an option. In the HHG process an intense laser pulse is injected into a gas, ionizing electrons, accelerating them, and recombining them with the ions. The emitted photons are phase locked with the drive laser field and the spectrum is rich of odd harmonics with almost the same amplitude up to a threshold photon energy. Beyond that the harmonics have a strong drop off in intensity. Expanding this threshold energy up to 310 eV (4 nm wavelength) is challenging and favors longer drive wavelength. For the following discussion we assume a wavelength of 2 microns, driving the HHG process.

To model the seed we assume an ideal HHG pulse, where all harmonics are locked to the drive pulse. The pulse has an rms length identical to the drive wavelength of 2.004 micron and expanding up to the 501st harmonics (corresponding to 4 nm) with the same amplitude and then a rapid drop off for high harmonics by a factor of 0.5 for each next harmonic. The signal is filtered for the Genesis simulation in the frequency range of +/- 50% around the resonant wavelength of 4 nm to avoid aliasing effects of the lower harmonics. The resulting power profile is shown in Figure 2.21. The power has been scaled to have a peak value of 1 GW. The total pulse energy of this ideal seed is 60 nJ, equally distributed for the odd harmonic between 251st and 501st harmonic.

The signal is rather unique because it has only significant amplitude over one wavelength of 4 nm spaced by 501 wavelength. Under this condition the FEL operates in the weak radiant regime, where the seed signal slips almost undisturbed over the bunch while the effective FEL signal is evolving on a much slower rate. The profile after 5 undulator

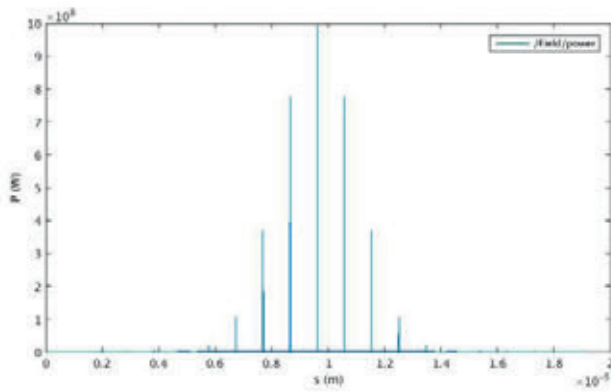


Figure 2.21: Seed signal of HHG pulse to be resonant at 4 nm.

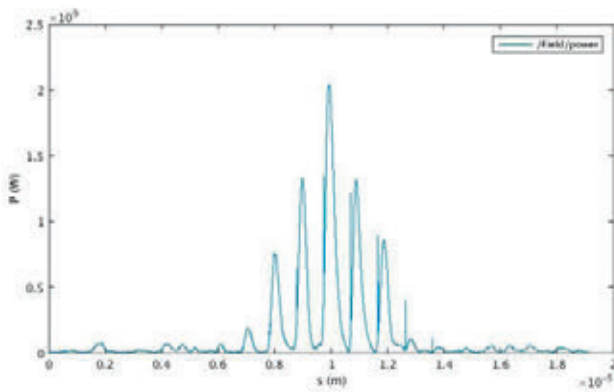


Figure 2.22: Radiation power profile after 5 undulator modules.

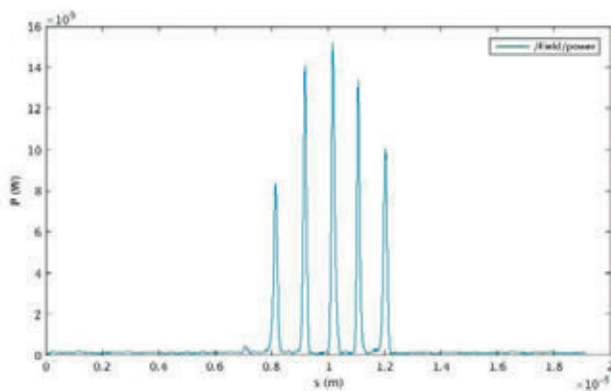


Figure 2.23: FEL signal at 1 nm at saturation after 5 undulator modules in the second stage.

modules is shown in Figure 2.22. The seed signal is still visible but the FEL spikes are of the same amplitude but much wider. The end of this stage was chosen to avoid saturation which prevents an efficient harmonic conversion due to the spoiled energy spread. Also noticeable is the SASE background which is on the 1% level with respect to the amplified HHG signal.

While the first stage was tuned to 4 nm with a K-value of 3.5 the second stage is tuned to the 4th harmonics with an K-value of 1.27. The harmonic content of the 4th harmonic in the first stage is driving the second stage till saturation is achieved. Because the contrast ratio of the bunching at harmonics is stronger the seed signal of the second stage is cleaned up with reduced content of the SASE background. After 5 further modules the pulse has reached saturation as shown in Figure 2.23. For the same reason the spikes are shorter.

The odd harmonics are separated by 0.5%, which requires a tuning of the drive laser wavelength by the same amount. The lowest harmonics of the HHG seed is given by the tuning range of Athos which is 5 nm. The smallest harmonic is the second harmonic in the HHG stage, resulting in a wavelength of 2.5 nm. This means that in the wavelength range 5 – 2.5 nm there will be only one stage, seeding directly at the final wavelength. Therefore it is required that the HHG seed provides sufficient seed power down to 2.5 nm. All shorter wavelength can be reach without any problem but it is preferred that the initial seed is at the longest wavelength. This results in the tuning ranges: 5 – 2.5 nm → direct seed, 2.5 – 1.6 nm → 2nd harmonic, 1.6 – 1.25 nm → 3rd harmonic, and 1.25 – 1 nm → 4th harmonics. The presented case shows the shortest wavelength and all other cases should perform better in terms of required length and FEL pulse energy.

Because the total length requires at least 10 modules the HHG seed signal cannot be injected at the self-seeding chicane into the undulator, which would be convenient due to the existing diagnostics of the signal for transverse overlap. Therefore it has to be injected before the first undulator module. Possible position would be directly before the first module, at the location between C-band linac and end of switchyard or at the last dipole of the switchyard. Only the last would avoid the requirement of a mini-chicane of the

in-coupling but the rather long distance of 64 m from the dipole to the first module would make it rather inconvenient.

### 2.3.5.3 Mode-locked Lasing

Interleaving short undulator modules with a fixed delay by the chicanes, as it can be configured in the Athos beamline generate module structure in time and frequency domain. Here the bandwidth in spectrum is roughly given by the number of period per module. However the FEL process is still started by the underlying SASE process and several of the modes are not locked in phase and time. This can be overcome by introducing a periodic perturbation in the electron beam, which periodicity is the same as the slippage in one module and the delay of the chicane.

The simplest method to provide such periodic perturbation is energy modulation with an amplitude larger than the FEL resonance bandwidth. Here FEL spikes are predominantly formed at the bottom and top of the energy modulation. With even larger modulation the amplification at the bottom of the modulation is preferred resulting in space of the energy modulation.

However the R56 of the chicanes in Athos will slowly modulate the current with a growing spike at the falling energy chirp in the modulation. To prevent the required adjustment of the spikes from the bottom to the falling flank of the modulation, linear negative taper of the undulator field over each module is preferred. In fact the selection of the slice is identical to the slicing as described above. The mode-lock lasing has the additional benefit that due to the frequent shift of the spike to the next modulation the effective slippage is significantly introduced. This established a common phase over many spike in strict analogy to the high-brightness mode, which is also driven by the fact of enhanced slippage.

Figure 2.24 and Figure 2.25 show the profile and spectrum of a mode-locked FEL pulse. The simulation used a modulation period length of 400 nm and a peak-peak modulation of 0.12% of the electron beam energy. The slippage within one undulator module is 52 nm and the chicanes are set to 348 nm to match the total slippage with the modulation periodicity. Note that the FWHM of the spectrum is 2% which corresponds to the inverse of numbers of periods per module. Shorter modules would result in larger bandwidth. The

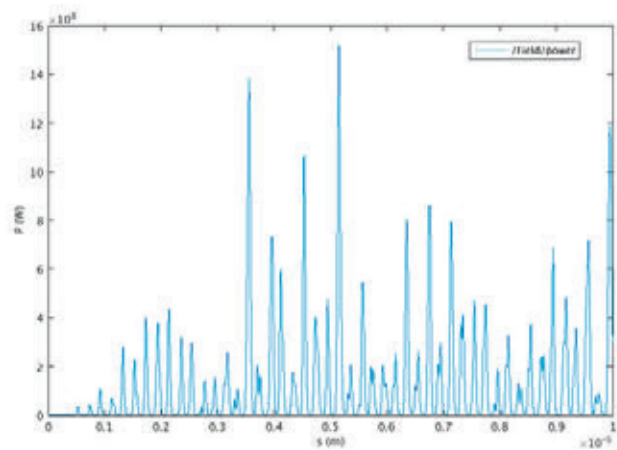


Figure 2.24: FEL profile after 3m of undulator with mode-locked pulse structure.

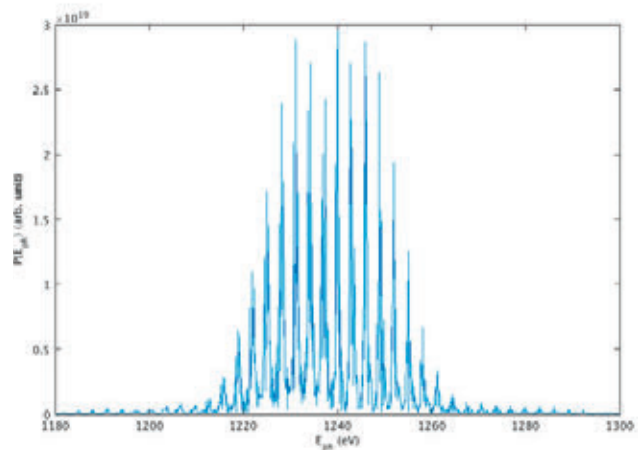


Figure 2.25: Corresponding spectrum of mode-locked pulse.

number of modes in the spectrum is controlled by the periodicity of the modulation. A longer periodicity would result in fewer modes.

Configuring Athos in mode-locked operation utilized the chicane similar to the optical klystron. For a better spectrum and pulse structure the applied number of chicane induced slippage has to be maximized up to 15 times given by the Athos lattice. However the optical klystron counteracts this due to reduced saturation. Therefore the current of the electron beam has been lowered to set the saturation to the end of the 16 undulator modules. For the simulation presented below the values was 2 kA.

Note that the presented results are not fully studied systematically but to show that the Athos system can be configured to support mode-locked lasing. The spectrum and pulse structure can be improved by optimizing the modulation amplitude and the taper gradient per undulator modules.

# 3 Electron beam components

## 3.1 Laser system

### 3.1.1 Gun laser system

A semi-conductor photo-cathode (Cs<sub>2</sub>Te) is presently the base-line electron source fulfilling the SwissFEL injector requirements in terms of beam brightness. For the operation of SwissFEL, a laser system capable of generating 200pC of photo-electrons is required. A minimum energy per pulse of 500 nJ at 266nm is required to produce 200pC of photoelectrons from a semi-conductor surface, assuming a QE of 0.2%.

### 3.1.2 General layout

The choice of the laser system gain medium and architecture has a direct impact on its final performance and reliability. The Yb:CaF<sub>2</sub> have all desired properties for the production of high energy, UV femtosecond pulses. Moreover by keeping the laser architecture simple and compact the system reliability is improved.

The use of calcium fluoride with ytterbium doping (Yb:CaF<sub>2</sub>) as an active laser medium for CW systems started in 2004 [21]. Its very interesting properties for laser amplification

led to developments for short-pulse, high energy laser system up to the TW-scale.

- Yb:CaF<sub>2</sub> crystal exhibit a very broad and smooth emission band. The material is able to emit in the 1020-1060 nm spectral range allowing the generation of sub-500 fs pulses.
- The crystal absorption cross section exhibits a pronounced and narrow band peak at 980 nm. This point is of particular interest since it allows direct pumping with CW infrared diode modules developed for telecom applications.
- The material fluorescence lifetime of 2.4 ms and the thermal conductivity of 4.9 W.m<sup>-1</sup>.K<sup>-1</sup> are well suited to the design of high power lasers. The first one is crucial, since it permits high energy storage in regenerative amplifier cavities leading to high energy pulses. The later permits CW pumping with high average power while avoiding detrimental thermal effects

The future SwissFEL gun laser is a complex laser system. Apart from stringent specifications in terms of pulse energy, temporal profile and timing jitter, it needs to deliver three pulses with very different properties:

- A picosecond, temporally and spatially flat top UV ( $\lambda=260$  nm) pulse that generates the photo-electrons at the cathode.
- A picosecond, temporally Gaussian, infrared pulse ( $\lambda=1040$  nm) for the laser heater.
- A sub-50 fs temporally Gaussian, infrared pulse ( $\lambda=1040$  nm) used as a short probe in order to characterize temporally the UV pulse via optical crosscorrelation. The schematic of our Yb:CaF<sub>2</sub> CPA system is shown in Fig. 3.1.1. The oscillator delivers broadband pulses at 71.4 MHz and is used as seed for the 100 Hz amplifier. Up to now, our choice for the oscillator will be the Origami-10 (OneFive). The reason for this is the exceptionally low timing jitter of the device when synchronized to the master timing system. The specific associated synchronization electronics have been developed by the PSI Timing and Synchronization group. This results in an integrated jitter noise that is <35 fs RMS over 10Hz-1MHz and <10 fs RMS over 1kHz-10MHz. After stretching, the oscillator output is amplified in a regenerative amplifier up 5 mJ energy before compression.

Laser specifications	
Nominal pulse energy on cathode	5 - 500 nJ
Central wavelength	250-300 nm
Bandwidth (FWHM)	1-2 nm
Pulse repetition rate	100 Hz
Double-pulse operation	yes
Delay between the two pulses	28 ns
Laser spot size on cathode (rms) (10 pC / 200 pC)	0.1 / 0.27 mm
Minimum pulse rise-time	< 0.7 ps
Pulse duration (FWHM)	3-10 ps
Longitudinal intensity profile	various
Transverse intensity profile	Uniform
Laser-to-RF phase jitter on cathode (rms)	<100 fs
UV pulse energy fluctuation	< 0.5% rms
Pointing stability on cathode (relative to laser diameter)	<1% ptp

Table 3.1.1: Gun laser characteristics for SwissFEL.

## Gun laser setup with double bunch operation

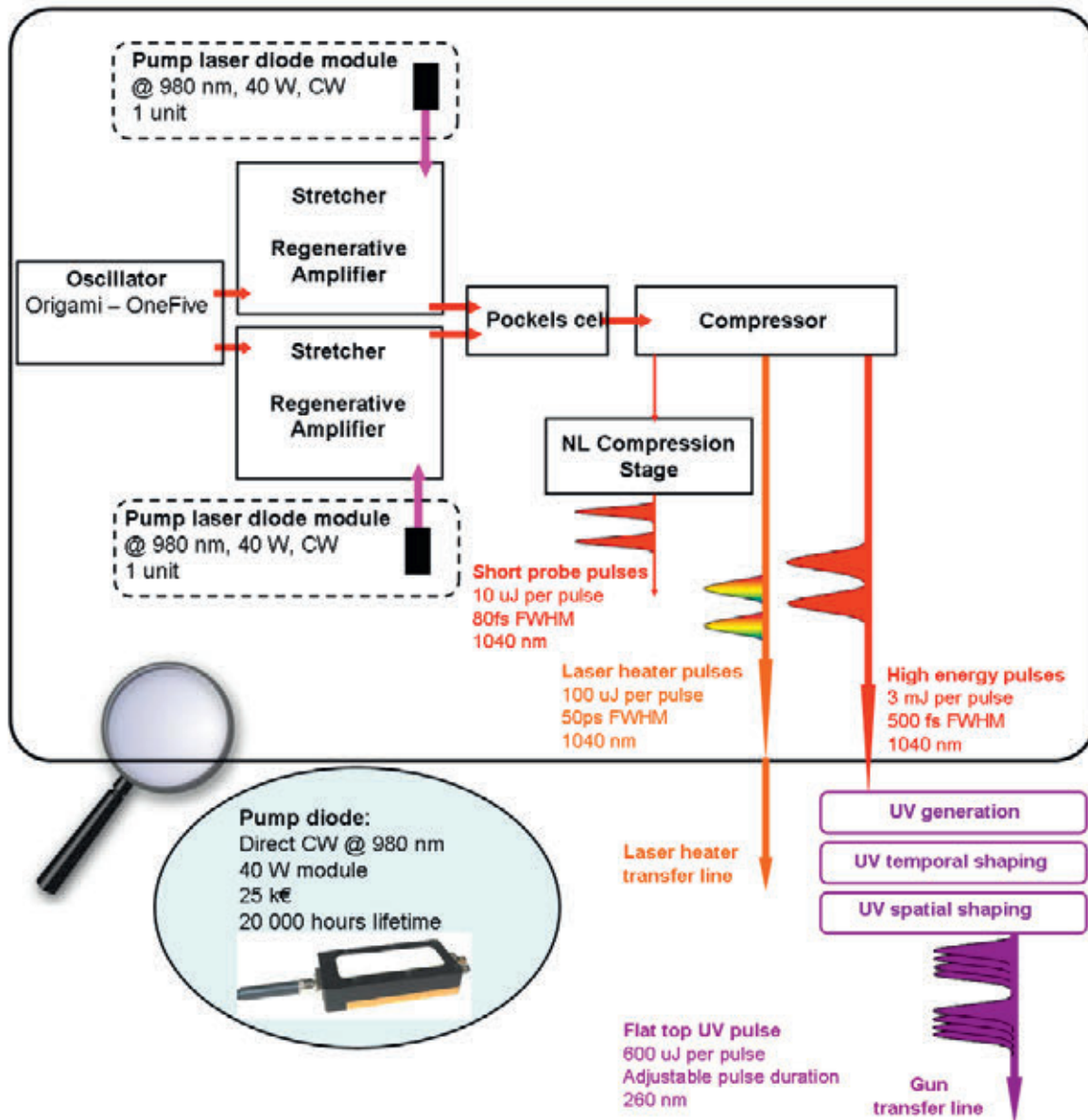


Fig. 3.1.1: Schematic of the gun laser architecture [22]. The system is able to deliver the temporally shaped UV pulses to the gun cathode but also the laser heater pulse and a short probe for UV pulse diagnostic. The system is able to deliver 2 pulses delayed by 28 ns in order to seed the hard and soft X-ray line of the FEL.

After amplification, the pulse is compressed to 500 fs FWHM duration with a transmission grating pulse compressor. The pulse energy is around 3 mJ. Afterwards, a properly designed frequency conversion stage produces 800  $\mu$ J at 260 nm. Subsequent UV temporal and spatial shaping consisting in respectively, pulse stacking and aperture clipping enables to generate 500  $\mu$ J, temporally and spatially flat-top UV pulse.

Details of the pulse shaping techniques can be found in the SwissFEL CDR [23].

### 3.1.3 Two bunch operation regime

Synchronous operation of the Athos and Aramis beamlines at 100 Hz requires the gun laser to provide two pairs of UV and nIR pulses, respectively, delayed by 28 ns. While the UV pulses are used for driving photoemission on the Cs<sub>2</sub>Te cathode, the nIR pulse pair shall be used for operating the laser heater. In order to reduce the complexity and cost of the laser system the two laser pulses in the UV and nIR, respectively, shall be identical in energy, beam size and pulse duration.

An additional pair of nIR pulses shall be used for the temporal diagnostics (cross-correlation) of the UV pulse.

#### • Concept for double pulse generation:

A split-delay and recombine (SDR) approach shall be implemented for the formation of two pulses in order to keep the complexity and cost low. For the gun, the 50% laser beam split and delay takes place in the UV, prior to temporal

shaping (pulse stacking). The energy of the replica will be controlled by the attenuators located in the two individual arms. The energy attenuators consist of a  $\lambda/2$  wave-plate and a polarizer. The beam diameter and pulse energy on the cathode shall be identical for the two pulses.

For the laser heater, a pair of 50 ps nIR pulses is required, delayed by 28 ns. Similar to the UV beam the SDR will be done in the laserlab before transport to the laser heater. Optionally SDR could be performed directly on the laser heater table located next to the electron beamline, in order to reduce misalignment caused by the long beam transport from the laser hutch to the laser heater (20 meter). However, SDR in the laserlab seems to provide higher stability as the mechanical and temperature stability might be significantly better than in the tunnel.

• **Diagnostics:**

the beam profile of individual pulses on the virtual cathode shall be recorded only destructively, i.e. by blocking 1 pulse, using a conventional CCD.

The individual pulse energy shall be recorded individually by means of a fast photodiode and box-car integration.

Drift measurements shall be performed only for 1 pulse out of the pulse pair, to reduce cost and complexity. The expected relative drift between two neighboring pulses is expected to be minor.

### 3.2 RF systems

In the Athos branch of SwissFEL there are essentially two RF stations: one C band accelerating module identical to those of Linac 1 and an X band RF deflector. The C band module of

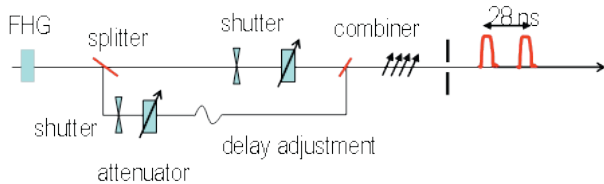


Fig. 3.1.2: Schematic of the two laser pulse generation upstream of the temporal and transverse shaping.

the Athos Linac is located upstream the Athos undulator and is used to vary the electron beam energy by +/- 250 MeV in order to change the wavelength of the FEL. The X band deflector is located downstream the undulator line and will be used as a diagnostic tool to tilt the bunch so that its projection on a screen will give information on the longitudinal shape of the bunch. Since it is located downstream the undulator, it is not perturbing the FEL beam and can be used permanently. When the X band deflector is combined with the dump dipole spectrometer, it will become possible to observe electron energy drop due to lasing and so monitor the bunch slices which do contribute to the FEL intensity.

#### 3.2.1 RF systems of the Athos Linac

The C band module in Athos consists of a solid state RF modulator powering a klystron operating at the C band frequency. The klystron is situated in a room in the upper floor above the accelerating tunnel and is connected with waveguides to the C band accelerating structures (Fig. 3.2.4.1). The main parameters of this C band module are summarized in table 3.2.1.1.

	Unit	C-band cavities (Athos linac)
Frequency (MHz) – fb=142.8 MHz		5712 (40 × fb)
Phase Advance		2π/3
Active Length	mm	1978
Total Length	mm	2050
Number of Cells		113
Operating Temperature	°C	25–35
Maximum Gradient	MV/m	30
Operating Gradient	MV/m	28.5
Required Input Peak Power per structure		27.2 MW for 27.5 MV/m
Klystron maximum performance		50 MW – 2.5 μs 40 MW – 2.5 μs
Filling Time	ns	329
Number of structures		4
Number of structures per klystron		4

Table 3.2.1.1: Summary of the key parameters of the accelerating structures of Athos.

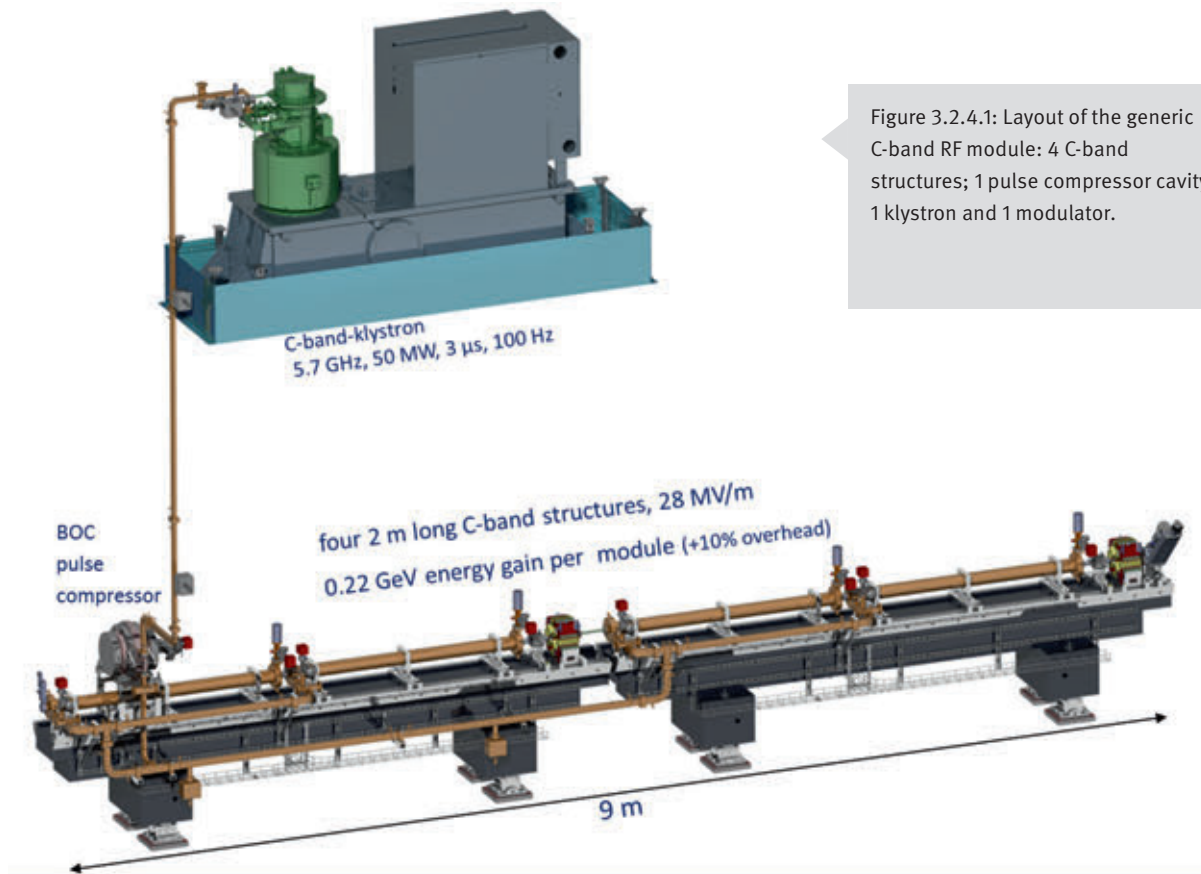


Figure 3.2.4.1: Layout of the generic C-band RF module: 4 C-band structures; 1 pulse compressor cavity; 1 klystron and 1 modulator.

### 3.2.1.1 C-Band module overview

The Athos linac consists of 4 two-metre long accelerating structures (with a possible upgrade to 8 structures) to vary the beam energy by +/- 250 MeV in the Athos branch. The final energy is ranging from 2.65 GeV (extraction energy of 2.9 GeV together with a deceleration in the Athos linac) to 3.4 GeV (extraction energy of 3.15 GeV together with an acceleration in the Athos linac). The 4 accelerating structures are grouped into a so-called RF module, each module being composed of four accelerating structures, one pulse compressor, one 50 MW klystron and one solid-state modulator (Figure 3.2.4.1). The design frequency of these C-band structures is 5712 MHz as in the linac of the SACLA project [24].

The maximum peak power of the klystron is 50 MW with a 3  $\mu$ s pulse length. The power requirements are determined by the required average gradient (27.5 MV/m), the accelerating structure design, the energy multiplication factor of the pulse compressor (see Figure 3.2.4.12) and the overall losses in the waveguide network. Single-bunch operation requires 28 MW at the accelerating cavity input. The waveguide network is based on an asymmetric design to take into account both phase synchronism and group delay for an optimum operation with the pulse compressor. The average RF path length from the klystron output to the accelerating structure input is roughly 10 metres which ideally corresponds to 7% losses. Taking into account the pulse compressor and all the flanges, a conservative value of 20% has been assumed for the losses.

In the case of two-bunch operation mode with a bunch spacing of 28 ns, the required power is below 40 MW.

### 3.2.1.2 C-band Accelerating Structure

The C-band accelerating structure has 113 cells, including two coupler cells of the J-type and operates with a  $2\pi/3$  phase advance. The length of each cell is 17.495 mm and the active length of each structure is 1.978 m. Each cell has rounded walls to increase the quality factor (Figure 3.2.4.3). Note that a disk-loaded structure and a structure with cup-like cells have also been considered. However, having a lower quality factor, they require slightly more input power to achieve the same accelerating gradient. All along the structure the iris tips are elliptically shaped and are optimized to ensure minimum peak surface electric field, the iris thickness being constant at 2.5 mm – a good compromise between high shunt impedance and mechanical rigidity. The required RF power to achieve an accelerating gradient of 27.5 MV/m without pulse compressor is about 27.2 MW. Table 3.2.4.1 shows the main parameters of the synthesized C-band structure.

### 3.2.1.3 RF C-band Pulse Compressor

Each RF module is composed of a single 50 MW klystron feeding a pulse compressor and four two meter long accelerating structures. The pulse compressor is based on a single Barrel Open Cavity (BOC). The BOC makes use of a “whispering gallery” mode which has an intrinsically high quality factor and operates in a resonant rotating wave re-

Operating frequency	5712.0 MHz
Operating temperature	40oC ± 0.1°C
Phase advance	2π/3
Flange-to-flange total length	2050 mm
Number of cells	113
Cell length at operating temperature	17.495 mm
Iris thickness at 20 °C	2.5 mm
Iris radius at 20 °C	7.257 mm ... 5.612 mm
Cell radius at 20 °C	22.432 mm ... 21.988 mm
Input coupler	J type
Output coupler	J type
Average (over Linacs) accelerating gradient	27.5 MV/m
Shunt impedance per unit length	81.7 MΩ/m
Peak power – accelerating gradient of 27.5 MV/m – no SLED	27.2 MW
Filling time	322 ns
Maximum pulse repetition rate	100 Hz
Material of the cavity	Cu-OFE
Material of the flanges, supports and cooling connectors	316LN
Concentricity tolerance	+/- 25 μm
Design pressure drop of the cooling channels	4 bar

Table 3.2.4.1: Main parameters for the C-band structures.

gime; moreover, and contrary to the conventional SLED scheme, a single cavity is sufficient to define the pulse compressor, without the need for two cavities and a 3-dB hybrid.

### 3.2.2 Power systems for the SwissFEL linac

The basic idea for the linac RF power system is to keep it identical to the injector systems as far as possible.

#### 3.2.2.1 C-Band Klystron

Due to the frequency choice the available klystron types are limited. Toshiba has developed a new version adapted to 100 Hz repetition rate and 3 μs pulse length.

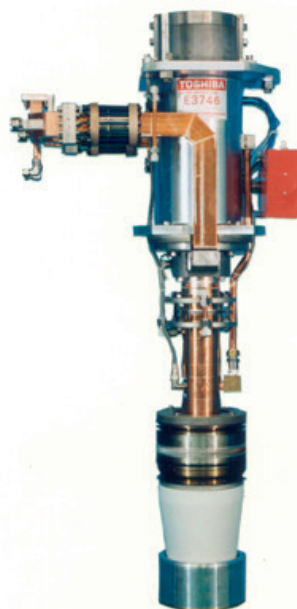


Figure 3.2.6.1.1: Similar C-Band klystron (Toshiba E3748).

Type	Barrel Open cavity
Frequency	5.712 GHz
Diameter	492 mm
Resonant mode	TM18,1,1
Number of coupling slots	70
Q	216000
Coupling factor (β)	10
Max. input power	50 MW
RF input pulse length	3 μs
RF compressed pulse length	330 ns
Energy multiplication factor (M)	2.13
Repetition rate	100 Hz

Table 3.2.4.2: Main parameters of the pulse compressor

	Upgraded Version E37212	Unit
Nominal Frequency	5712	MHz
Klystron micro perveance (μl/V <sup>1.5</sup> )	1.44–1.62	Rel. unit
RF peak power	50	MW
Peak Cathode Voltage	370	kV
Peak Klystron Current	344	A
High Voltage Pulse Width	6.2	μs
RF Pulse Width	3	μs
Average RF Power	15.6	kW
Average Collector Power Dissipation	78	kW
Pulse Repetition Rate	100	pps
RF Bandwidth @ -1.5 dB	+/- 5	MHz
Gain	50	dB

Table 3.2.6.1.1: Technical data of the C-Band klystron types.

### 3.2.2.2 C-Band Modulator

The Athos C-band RF station will use a Type- $\mu$  modulator from Ampegon. Currently, this modulator is installed in SwissFEL at the location S10CB01, and in 2018, this modulator will be upgraded to the same state as all the other Ampegon modulators in SwissFEL and then installed in Athos.

	Value	Unit
Peak Voltage	370	kV
Peak Current	344	A
Pulse Repetition Frequency	100	Hz
Pulse-to-pulse voltage stability (rms)	< 15	ppm
Pulse to pulse timing jitter (RMS)	< 3	ns
High Voltage Pulse Width @76%	< 6.2	$\mu$ s
Flat-top Ripple (peak-peak)	+/- 1%	
Voltage rise time (10-90%):	< 0.8	$\mu$ s
Voltage fall time (90-10%):	< 1.7	$\mu$ s
Mains Supply	400	V
Mains Power Factor	> 99 %	

Table 3.2.6.2.1: Target parameters for the C-Band Modulator.

The modulator will be separated in two or more mechanical units in order to allow transportation and installation inside the SwissFEL technical building. Figure 3.2.6.2.1 shows the reference design for the modulator mechanics. The tank with the transformer and the klystron socket will be a separate unit. The racks with the electronics and auxiliaries will be placed close to the modulator on a double floor.

### 3.2.3 Post-undulator X-band Transverse Deflecting Structures (TDSs)

The SwissFEL project will produce soft X-rays FEL radiation with pulse durations ranging from a few to several hundred femtoseconds. Electron beam diagnostic based on a transverse deflecting structure (TDS) placed downstream of the undulators (post-undulator TDS) in conjunction with an electron beam energy spectrometer can indirectly measure the pulse length of these ultra-short photon beam analysing the induced energy spread on the electron bunch due to the FEL process [25]. Furthermore, a complete characterization of the 6D phase space by means of measurements of the bunch length, energy and of the transverse slice emittances (vertical and horizontal) are important tasks for commissioning and optimization of FEL process. In this context, the

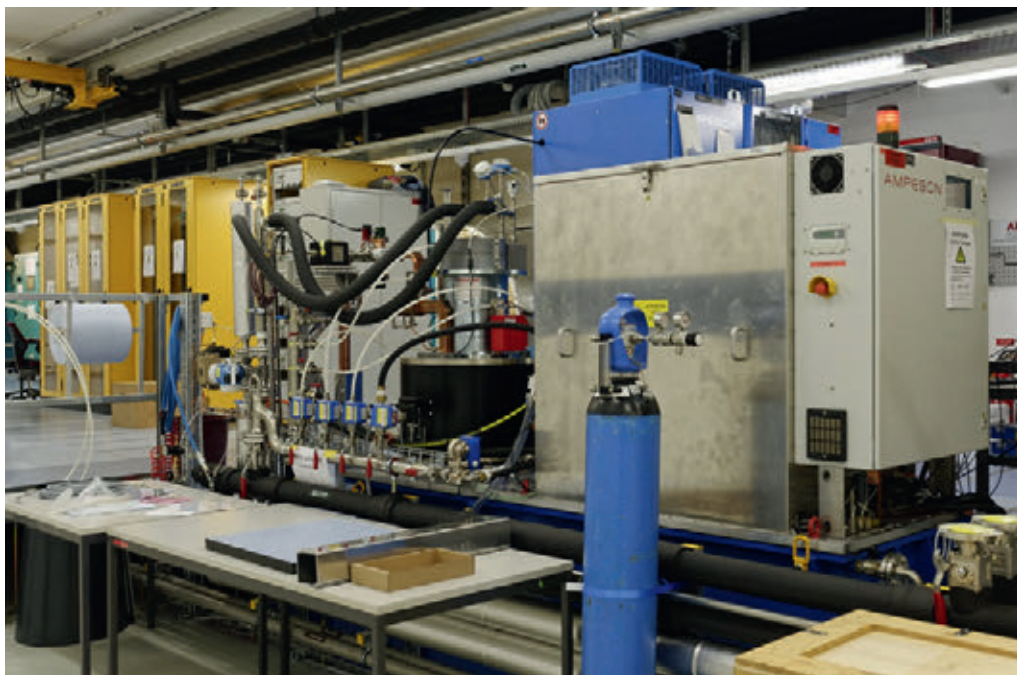


Figure 3.2.6.2.1: Ampegon Prototype Modulator to be installed at Athos.

design of an innovative X-band TDS structure, including a novel variable polarisation feature, is foreseen [26]. Table 3.2.3.1 contains the beam parameters at Athos post-undulator diagnostic section that have been used for the following calculations.

Parameter	Value	Unit
e <sup>-</sup> charge	10–200	pC
Peak current	2–3	kA
Pulse duration	2–30	fs (rms)
e <sup>-</sup> Energy	≤ 3.5	GeV
Emittance	≤ 300	nm
Energy spread	≤ 350	keV

Table 3.2.3.1: Beam parameters at Athos post-undulator diagnostic section.

Figure 3.2.3.1 shows a schematic layout with the concept of the post-undulator diagnostic section. Beam slice emittance in both transverse planes will be investigated by a multi-quadrupole scan technique combined with the TDS. By means of the TDS, the beam is vertically and horizontally streaked and a multi-quadrupole scan is performed in the horizontal or vertical direction, respectively, with the constraint of keeping the vertical/horizontal beam size constant over the whole scan. For this purpose, five quadrupoles are foreseen to be placed downstream of the TDS. Reconstruction

of the longitudinal phase space will be performed by means of the spectrometer line.

Figure 3.2.3.2 shows the  $\beta$ -functions of the beam lattice optics in the post-undulator diagnostic section. The locations of the deflectors are highlighted with a green circle and the  $\beta$ -functions are the same for the two polarization ( $\beta_x = \beta_y = 50$  m). Energy resolution at the spectrometer is less than 180 keV due to betatronic effect and 150 keV due to the screen resolution.

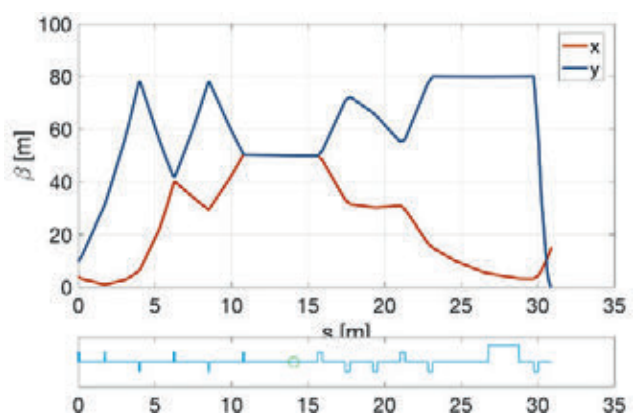


Figure 3.2.3.2: The  $\beta$ -function of the beam lattice optics for the post-undulator diagnostic section.  $s=0$  corresponds to the end of the last Athos undulator. The locations of the deflectors are highlighted with a green circle and the  $\beta_x = \beta_y = 50$  m.

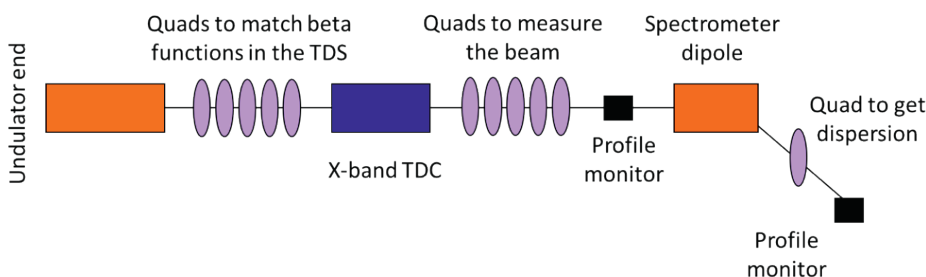


Figure 3.2.3.1: Concept of the post-undulator diagnostic section based on TDS.

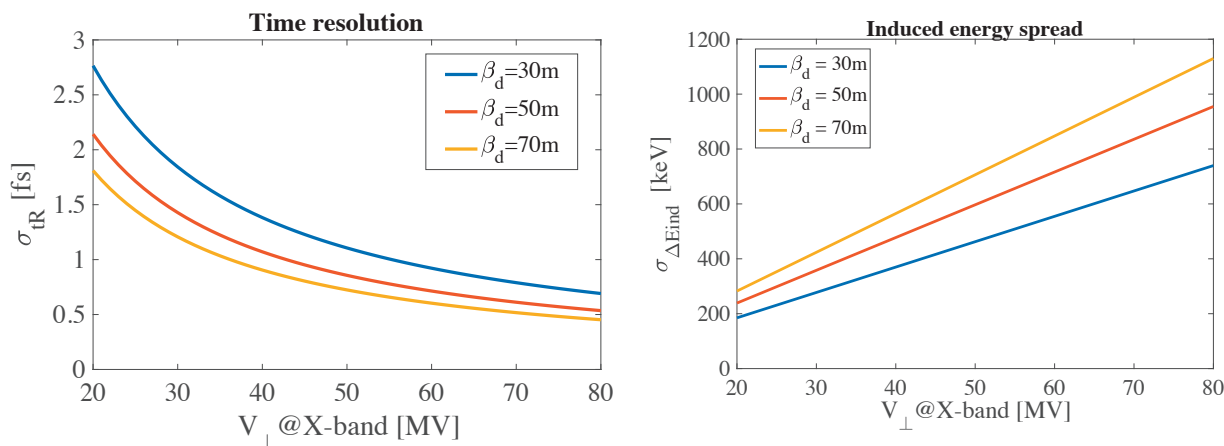


Figure 3.2.3.3: Time resolution (left) and rms induced energy spread (right) as a function of the integrated deflecting voltage. Sub-fs resolution with  $V_{\perp} \geq 45$  MV and  $\beta_d = 50$  m in both transverse planes.

Figure 3.2.3.3 shows the time resolution (left) and the induced energy spread (right) as a function of the integrated deflecting voltage. Time resolution is on sub-fs scale if the deflecting voltage is more than 45 MV with a  $\beta_d = 50$  m. Such time resolutions permit the resolution of the shortest beam profile pulse indicated in table 3.2.1 with approximately 2-3 slices. Induced energy spreads from the TDS is 500 keV with  $\beta_d = 50$  m.

Figure 3.2.3.4 shows the rms centroid jitter (left) and the calibration factor (right) as a function of the integrated

deflecting voltage. Considering the RF phase jitters indicated in figure 3.2.3.4 (left) and a deflecting voltage of 45 MV then the expected jitter of the streaked beam is approximately 200-700 $\mu$ m (rms) that is in the same order of magnitude of the beam size of the streak beam on the screen for the longer pulse ( $\sigma_y = 450\mu$ m) while is an order of magnitude higher for the shortest pulse ( $\sigma_y = 30\mu$ m).

The main RF parameters of the TDS and pulse compressor are summarized in table 3.2.3.2. A deflecting voltage of 45 MV could be achieved with a set of two TDS with an active

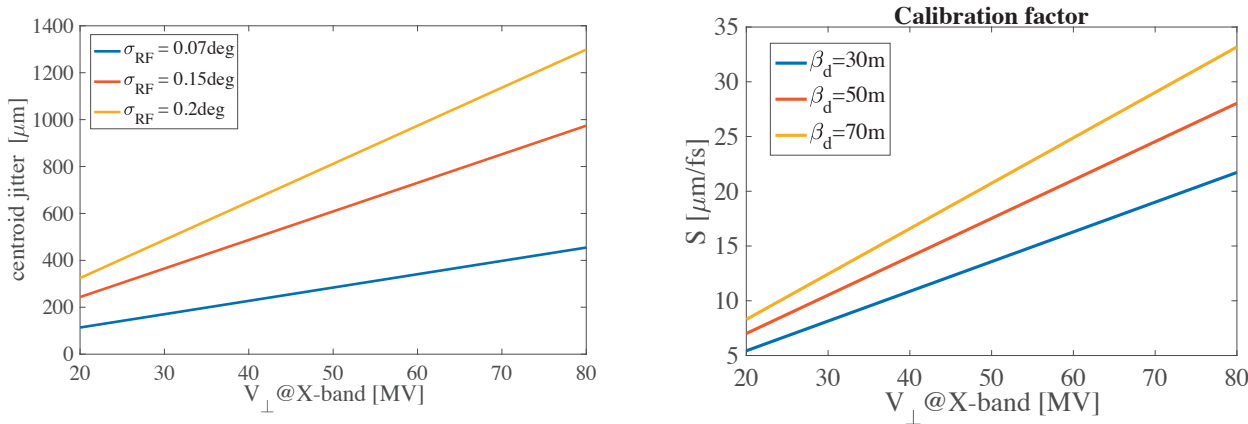


Figure 3.2.3.4: Centroid jitter (left) and calibration factor (right) as a function of the integrated deflecting voltage. Centroid jitter is estimated considering three different values of the RF phase jitter for  $\beta_d = 50$  m.

length of 1000 mm. Figure 3.2.3.5 shows a sketch of the X-band TDS RF power distribution system based on an X band modulator identical to the one used in the SwissFEL injector with 50 MW RF peak power could also provide the required power to the TDS and serve also as a spare part for the injector.

Parameter	Value	Unit
Frequency	11995.2	MHz
Phase advance	120	degree
Iris radius	4	mm
Active length	1000	mm
Filling time	129.5	ns
Number of structures	2	
Peak RF from klystron	50	MW
Power to voltage	6.124	MV/MW <sup>0.5</sup>

Table 3.2.3.2: RF parameters to reach an *integrated deflecting voltage of 45 MV*. Waveguide length is approximately 13.5 m and waveguide attenuation is  $-0.098$  dB/m (standard WG90).

### 3.2.4 Low-Level RF

The Low-Level RF (LLRF) system has to synchronize and control the RF fields in the accelerating structures to tight tolerances. In particular the RF pulse to pulse stability should reach 0.018 % rms pulsed voltage stability and 0.036 deg rms phase stability. In the Athos C band linac, a single klystron and an RF pulse compressor delivers RF power to four C-band structures (see Section 3.2.1). A generic overview of the RF station in the Athos linac is given in Figure 3.2.4.1. The controller therefore has to regulate amplitude and phase of the vector sum of a string of four accelerating structures. The LLRF system is based on modern FPGA technology and floating point processing platforms. Such a system allows the required flexibility for different RF stations, especially for the necessary phase switch for the RF pulse compression for the Athos RF stations. The RF signals from pick-ups and directional couplers are down-converted to common intermediate frequencies ( $f_{if}$ ), which are digitized by high-resolution, low-noise analogue-to-digital converters (ADC). Thus, the digital signal processing hardware and main parts of the firm- and software are generically independent of the RF frequency ( $f_{RF}$ ). Each RF station will receive a phase-stable, low-noise RF signal which is distributed via a cw drift-stabilized optical reference link system. This signal is required

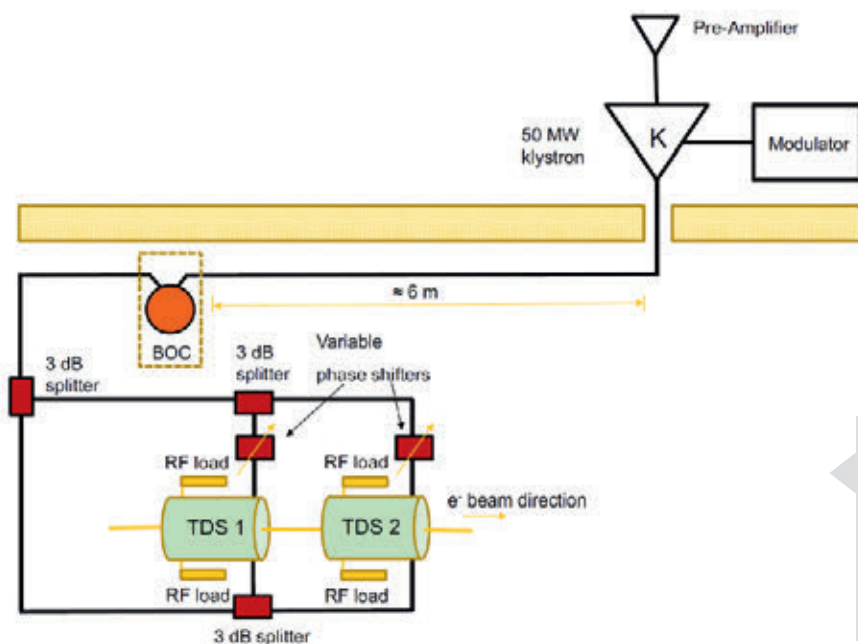


Figure 3.2.3.5: First concept for RF power feeding scheme, with SLED system and waveguide components.

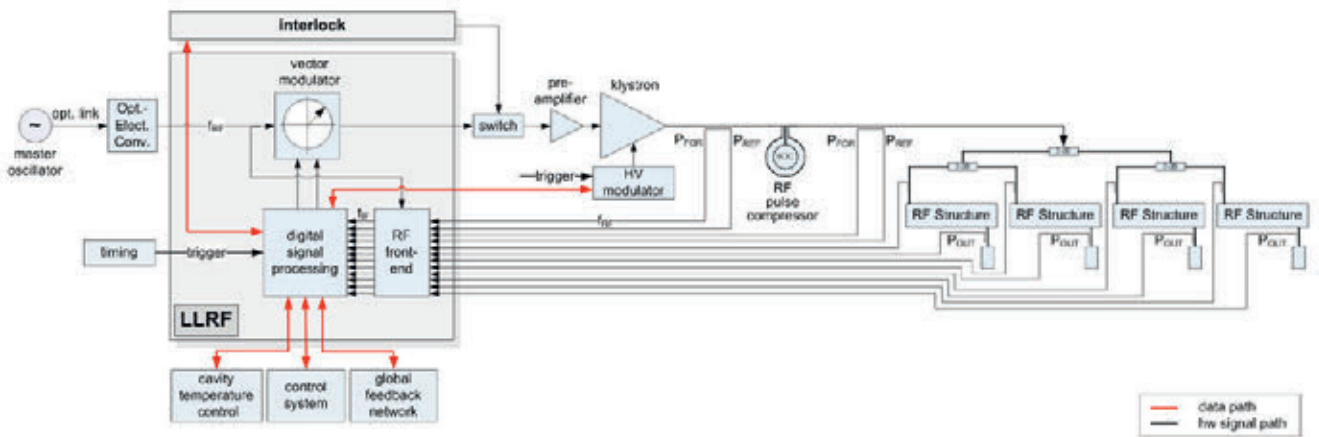


Figure 3.2.4.1: RF system overview of one RF station in the main linac with RF pulse compression.

to drive the vector modulator and to generate the local oscillator frequencies for the LLRF system (see Section 3.3). The IF frequency has to be chosen so that it is a sub-harmonic of the RF frequency ( $f_{RF}$ ), in order to alleviate the frequency generation. In addition, it has to be high enough to allow for a sufficient detection bandwidth of the RF signal, but finally also low enough to avoid performance degradation due to clock jitter of the successive ADCs. Today's state-of-the-art technology can provide 16 bit ADCs with sampling rates well beyond 100 MHz. The application of the non-IQ algorithm [27] for the I/Q detection in the LLRF digital signal processing part implies the use of IF frequencies of the order of a few 10's of MHz up to a maximum of 100 MHz.

All frequencies of the LLRF system (ADC/DAC clocks, local oscillator frequencies for the RF front-ends) are derived from the reference distribution and thereby tightly locked to the master oscillator. The trigger signals for pre-amplifier, modulator and digital signal processing are generated by an event-receiving unit which is directly coupled to the global event generator. The RF pulse duration is of the order of a few  $\mu s$ , which is too short for efficient intra-RF pulse feedback, due to the inherent latency of the digital system. In case the high-voltage modulators or the pre-amplifiers do not provide the necessary short-term stability, which may result in pulse-to-pulse phase jitter, the implementation of

fast analogue intra-pulse phase stabilization loops around the amplifier chain may be necessary. Pulse-to-pulse feedback corrects slow drifts in amplitude and phase, while adaptive feed-forward techniques provide the ability to reduce repetitive distortions. In order to compensate for drifts, it is therefore of utmost importance to minimize the drift of the components in the measurement path. To achieve this goal, all measurement cables from the directional couplers to the LLRF system, and the LLRF electronics itself, will be placed in a temperature-stabilized environment, with temperature variations not exceeding  $\pm 0.1^\circ C$ . During the R&D phase, the application of pulse-to-pulse calibration techniques will be explored, to minimize any remaining drifts and low-frequency jitter in the measurement of amplitudes and phases. In addition, the LLRF electronics provides optical high-speed Gigabit communication links to other sub-systems, which allows the implementation of beam-based feedbacks, such as longitudinal feedback. Pulse-to-pulse stability is then solely determined by the stability of the actuator chain, which consists of the reference distribution, the local phase-locked loops, the vector modulator, the pre-amplifier and the high-voltage modulator, together with the klystron. Each of these components has to provide stability such that the required short-term amplitude and phase stability of an RF station is reached.

### 3.3 Timing and synchronization

In an accelerator (and particularly in a free electron laser (FEL)) the electron bunches to be accelerated and linearly compressed demand extremely stable field phases in the RF accelerating cavities (with respect to the time they have been emitted from the gun photocathode by the gun laser). The SwissFEL RF structures, which will be operated at frequencies around 3, 6 and 12.0 GHz (S, C and X-band, respectively), need reference signals with the property that the temporal position of their zero-crossings, measured over a certain time (some ms) at different points in the machine, has to achieve a stability level below 10 fs. Moreover, the temporal stability and synchronization of laser systems at the experimental stations of the SwissFEL facility need to be kept within the lengths of the X-ray pulses over the duration of pump probe experiments (several minutes to hours). A number of diagnostics systems, such as, for example, beam arrival time monitors (BAM) and electro-optical bunch length monitors (EOM), will be able to measure the longitudinal properties of the electron bunches with reference to a temporally stable timing and synchronization system. Such beam-based information may be used to further improve the temporal stability of SwissFEL through longitudinal feedback systems. Although some other “clients”, such as the master event generator for the timing system and the beam position monitors (BPMs) for meas-

uring transverse beam position, may not need such high timing stability, the SwissFEL timing and synchronization system will be designed to provide fs stability, during short time periods of some  $\mu$ s up to some ms, to the majority of the “critical clients” along the accelerator and at the various experimental stations. Detailed description of the timing and synchronization of SwissFEL can be found in various publications [28] [15] [29].

### 3.4 Magnets

Electromagnets (bending dipoles, quadrupoles and correctors) will be used all along the Athos line, to focus (quadrupoles) and steer the beam and to correct the field quality (correctors, quadrupoles). An overview of the accelerator layout with the foreseen magnets is presented in Chapter 2. For the Athos phase of the project, an additional 76 quadrupoles and 13 dipoles will be required. Apart from the new 2 colors chicane dipoles AFSS, the magnets are identical to those installed at SwissFEL Aramis and details about them can be found in [23] [15]. In this chapter only the main parameters of these magnets are summarized.

#### 3.4.1 Quadrupole Magnets

The 22 mm-aperture QFD quadrupoles will be used in the switchyard and beam matching sections. The longer QFM

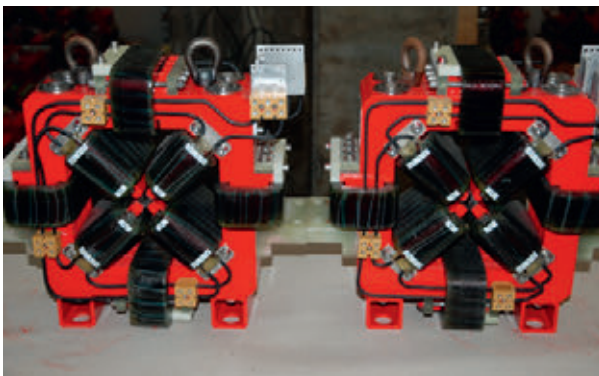


Fig. 3.4.1: QFF quadrupoles from SwissFEL (left picture) with integrated horizontal and vertical steering function. QFM quadrupole from SwissFEL water cooled (right picture).

	QFD	QFM	QFS (skew QFD)	QFBS (skew)	QFF
Location	Dogleg transfer line and to match into the X band TDS	post-undulator deflector to match the screen	Corrections in switchyard	Corrections in switchyard	Undulator FODO line
Number of magnets	32	8	1	1	34
Aperture	22 mm	22 mm	22 mm	45 mm	12 mm
Gradient G	20 T/m	50 T/m	20 T/m	1.5 T/M	50 T/m
Yoke length	0.15 m	0.3 m	0.15 m	0.08 M	0.08 m
Gradient measurement accuracy	$10^{-4}$	$10^{-4}$	$10^{-4}$	$\pm 10^{-3}$	$10^{-3}$
Multipole measurement accuracy at $r \sim 19$ mm	$10^{-3}$	$10^{-3}$	$10^{-3}$	$< 10^{-3}$	$10^{-3}$
Max. Current	10 A	50 A	10 A	10 A	10 A
Accuracy in magnetic axis determination (rms)	50 $\mu$ m	50 $\mu$ m	50 $\mu$ m	50 $\mu$ m	
Turns / coil	104	57	104		84
Cooling Art	air	water	air	air	air
Resistance at 50°C	0.5 $\Omega$	0.35	0.5 $\Omega$		0.39 $\Omega$
Total Weight	80 kg	158 kg	80 kg		32 kg
Technical reference	[15] [32]	[15] [33]	[15] [32]	[15]	[15,34]
Ref. Drawing	50023.41.001	50023.41.071	50023.41.001	50022.21.677	50023.41.035
Power Supply Type	bipolar	bipolar	bipolar	bipolar	bipolar
Steering max. field (H and V)	30 mT	N.A.	30 mT	N.A.	500 G
Steerers maximum current	2 x 10 A	N.A.	2 x 10 A	N.A.	2 x 10 A
Steerers Resistivity	2 x 0.15 $\Omega$	N.A.	2 x 0.15 $\Omega$	N.A.	

Table 3.4.1: Requirements for the quadrupoles used for the Athos transfer and undulator beamline.

magnets (0.3 m) will be used in the matching section to the X band deflecting cavity where stronger focussing is required. The gradient reproducibility from one quadrupole to another should be kept within  $10^{-3}$  but was measured to be up to 1% over 62 QFD magnets of Aramis line. The characterization of each magnet will consist of measuring the integral field strength versus current (magnetization curve, hysteresis cycle), the field quality (integral harmonics up to order  $n=10$ ) and the magnetic axis position. The position of the magnetic axis with respect to external fiducials has to be known within 50–100  $\mu$ m rms. Measurements using a vibrating wire system will be systematically performed on all the quadrupoles. The precision of the vibrating wire technique together with the precision on mechanical reference positions (fiducials) leads to an overall accuracy of 50  $\mu$ m rms in the magnetic axis

position. Identical magnets have already been measured for the SwissFEL Aramis line [30].

In particular, the impact of the thermal effects on the magnetic axis position has been carefully measured on a QFF undulator quadrupole and a vertical dilatation of 10  $\mu$ m at nominal current of 6 A has been observed. The steady state was reached after 6 hours [31].

QFF quadrupoles (50 T/m, 12 mm apertures) will be placed in the undulator beamlines. The same measurement goals as for the switchyard quadrupoles are required and the tolerance on the field quality is at the level of one percent. The fiducialization of the undulator quadrupole will be carried out using the vibrating wire technique.

To save space, all quadrupoles (QFD and QFF) will contain integrated steering functions in the horizontal and vertical directions. These steerer dipoles are air cooled and designed for 10 A maximum current with a bandwidth of 1 kHz for fast feedback orbit corrections (PS bandwidth limit).

### 3.4.2 Dipole magnets

The different types of dipoles are summarized in Table 3.4.2. A schematic layout and parameter summary is given in Chapter 2. To build dipoles as similar as possible to each other, all dipole yokes will be cut and machined from one

piece of iron so as to avoid differences in the material composition. The tolerance on the pole parallelism and flatness will be tightened to 10  $\mu\text{m}$  and 5  $\mu\text{m}$  respectively. Each AFBC3, AFL and AFSS dipole winding will integrate additional loops separately powered, to correct possible differences between dipoles.

	AFBC3	AFL	AFD1	AFSS	AFP1
Location	Switch-Yard	Switch Yard Vertical septum correction	Dump dipole 8 deg bend	2 colors chicane	Downstream AFD1 & at beam stopper
Number of magnets	4	2	1	4	2
Max. Strength	0.96 T	0.4 T	1.77 T	0.8 T	0.77 T
Effective Length	0.5 m	0.15 m	2 m	0.3 m	0.3 m
Fig. Type	H-Magnet	H-Magnet	H-Magnet	H-magnet	C - magnet
Integrated dipole field precision	$10^{-4}$	$10^{-4}$	$10^{-4}$	$10^{-4}$	$10^{-4}$
Transverse good field region (field constant within $10^{-4}$ )	70 mm	> 10 mm	10 mm	> 20 mm	> 2 mm
Integrated dipole field (T.m)	0.512 T.m at 150 A	60.8 mT.m at 50 A	3.547 T.m at 150 A	0.25 T.m at 150 A	0.22 T.m
Full gap	22 mm	20 mm	20 mm	8 mm	12 mm
Maximum Current	150 A	50 A	150 A	150 A	N.A.
Turns per coil	57	65	108	20	N.A.
Cooling	Water	water	Water	water	N.A.
Flow Rate	1.29 l/min.	0.62 l/min.	4.45 l/min.	1 l/min	N.A.
Mass	800 kg	75 kg	3350 kg	60 kg	36 kg
References	[15,35,36]	[15,35]	[15,35,37]	[38]	[15]
Ref. Drawing	50023.41.233	50023.41.177B	50023.41.302	50023.41.788	50023.41.230
Steering max. V integrated field (mT.m)	8.54 mT.m	1.4 mT.m	N.A.	+/- 400 $\mu\text{rad}$ at 3.5 GeV	N.A.
Steerers maximum current	10 A	10 A	N.A.	10 A	N.A.
Steerers Resistivity	0.19 $\Omega$	0.04 $\Omega$	N.A.		N.A.

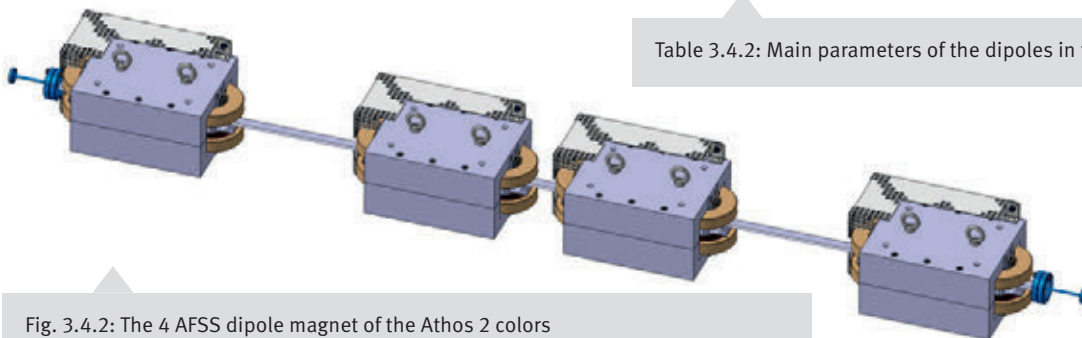


Table 3.4.2: Main parameters of the dipoles in the Athos line.

Fig. 3.4.2: The 4 AFSS dipole magnet of the Athos 2 colors chicane to adjust the delay between the two FEL pulses from 0 to 500 fs.

### 3.4.3 Corrector magnets

Eight separated steering magnets (SFQFM) for horizontal and vertical correction of the beam position will sit near each QFM quadrupole (where there is no steering function). SFQFM steerers yoke are made out of ARMCO iron. They work at a nominal current of 10 A, producing a nominal field of 20 mT. The magnetic length is 0.05 m and the equivalent aperture is 80 mm.

QFD and QFF quadrupole magnets do integrate a steering function thanks to additional corrector coils driven by 10 A power supplies. A deflection angle of 0.3 mrad at maximum energy is specified for the QFD steerers and 0.2 mrad for the QFF steerers at 5.8 GeV. Finally each extremity of the undulators will be equipped with vertical and horizontal steerers (window frame;  $\pm 200 \mu\text{T}\cdot\text{m}$ ; 10A) to compensate the kicks errors introduced by the permanent magnets of the undulator (when changing gap).

### 3.4.4 Sextupole magnets

Sextupoles	
Location	Switchyard & Aramis collimator
Name	HFB
Quantity	7
Pole Tip Field (mT)	144.5
Yoke Length	80 mm
Aperture	20 mm
Technical Specifications	[39]

### 3.4.5 DC magnet power supplies

The Power Supplies (PS) for the DC magnets mentioned above are designed and tested in-house and have a direct interface to the EPICS control system. As for any particle acceleration application, the PS for the SwissFEL must fulfil

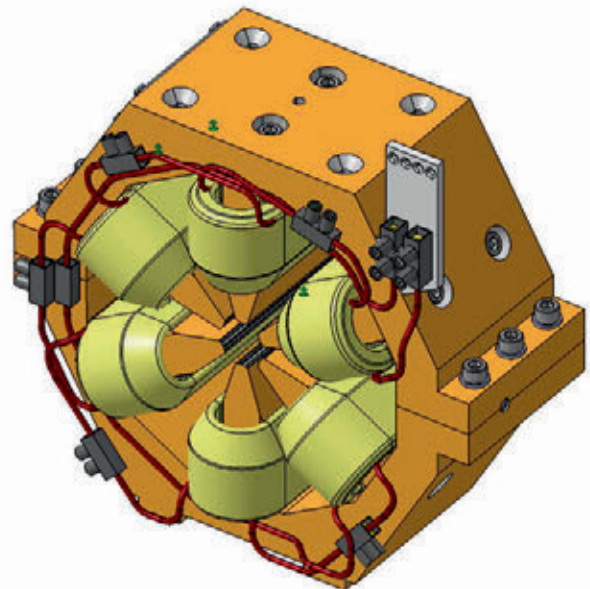
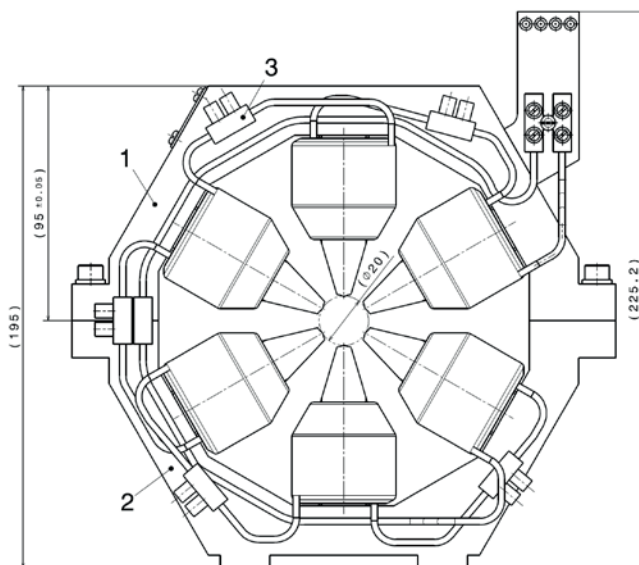


Fig. 3.4.4: HFB sextupoles located in the switchyard to the Athos line.

very high stability and precision requirements. They consist of switched-mode converters controlled by 2<sup>nd</sup> generation PSI-type Digital Power Electronics Controllers (DPC). A detailed description of the system is given in [23].

The list of power supplies is summarized in Table 3.4.5.1. The table also shows the cooling type and the power rating per PS.

PS type	Used in ...	Number	Cooling	Power
10A/24V/ bipolar	Injector (99) Linac (189) Aramis (178) Athos (313)	779	air	0.24 kW
20A/10V/ bipolar	Injector (13)	13	air	0.2 kW
50A/24V/ bipolar	Injector (1) Linac (1) Aramis (17) Athos (8)	27	air	1.2 kW
100A/10V/ bipolar	Linac (1)	1	water	1.0 kW
150A/40V/ bipolar	Injector (1) Linac (6) Aramis (1) Athos (5)	13	water	6.0 kW
150A/110V/ bipolar	Linac (1) Aramis (2) Athos (1)	4	water	16.5 kW
200A/50V/ bipolar	Injector (1)	1	water	10.0 kW
220A/40V/ unipolar	Injector (5)	5	water	8.8 kW
220A/100V/ unipolar	Injector (2)	2	water	22.0kW

Table 3.4.5.1: Power supply list for SwissFEL.

Each of the quadrupole magnets QFD, QFDM and QFF has three windings rated 10A, one quadrupole- and two corrector-windings. These magnets and all the corrector magnets and the corrector windings of the dipole magnets are energized from 3\*10A PS according to fig. 3.4.5.1. Optionally one channel of the triple PS can be equipped with a high-precision ADC, if the stability requirements are very high. The triple PS is controlled by one DPC controller with a serial optical link to the EPICS control system. The converters, the current sensors (DCCT), the controller and the optional ADC are installed in a 19" module (dotted line in fig. 3.4.5.1). Up to 7 such 19" modules can be installed in a rack, which contains a common DC link for all the converters. The DC link voltage can be adjusted as required, allowing the DC/DC converters to operate with a reasonable modulation index. For reliability reasons, fans are omitted entirely; the controllers and the DC/DC-converters are designed to operate with free convection cooling.

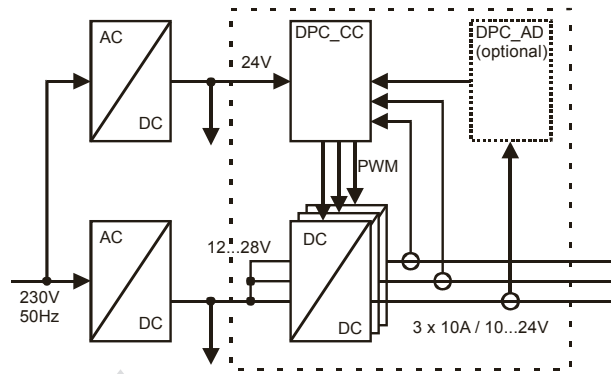


Fig. 3.4.5.1: Converter concept 3\*10A.

precision ADC, if the stability requirements are very high. The triple PS is controlled by one DPC controller with a serial optical link to the EPICS control system. The converters, the current sensors (DCCT), the controller and the optional ADC are installed in a 19" module (dotted line in fig. 3.4.5.1). Up to 7 such 19" modules can be installed in a rack, which contains a common DC link for all the converters. The DC link voltage can be adjusted as required, allowing the DC/DC converters to operate with a reasonable modulation index. For reliability reasons, fans are omitted entirely; the controllers and the DC/DC-converters are designed to operate with free convection cooling.

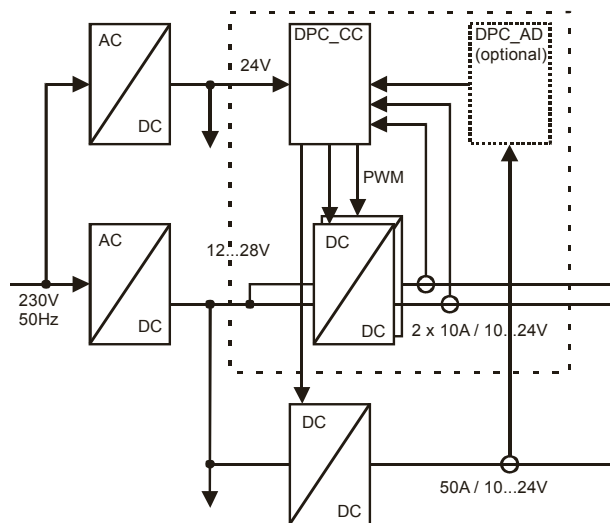


Fig. 3.4.5.2: Converter concept 1\*50A+2\*10A.

The QFM magnets are rated 50A. For that purpose a bipolar 50A converter with a switching frequency of 100kHz has been developed. The converter is built on a printed circuit board and installed in a separate 19" module. It requires forced air cooling, which is realised with 2 redundant fans for reliability reasons.

The 3\*10A concept mentioned above is adopted also for the 50A PSs. One 10A converter is removed and replaced by the 50A converter. This leads to the 1\*50A + 2\*10A concept according to fig. 3.4.5.2. Up to 4 such systems can be installed in a rack, which contains a common DC link for all the converters. The DC link voltage can be adjusted as required, allowing the DC/DC converters to operate with a reasonable modulation index.

The PSs with higher current ratings are built according to fig. 3.4.5.3. They have been in service at the SwissFEL Injector Test facility and were moved to the SwissFEL. Totally 5 different types are used in SwissFEL:

- PS 220A / 40V / unipolar 2 pc. per rack
- PS 220A / 100V / unipolar 1 pc. per rack
- PS 200A / 50V / bipolar 1 pc. per rack
- PS 150A / 40V / bipolar 2 pc. per rack
- PS 150A / 110V / bipolar 1 pc. per rack

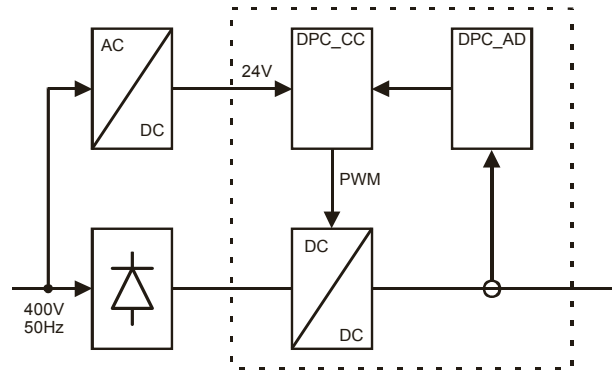


Fig. 3.4.5.3: Converter concept 150.....220A.

A water cooled 6-pulse diode rectifier, connected to the mains via a transformer, serves as source for the DC link. The DC/DC-converter are realized with hard switched IGBTs operating with a switching frequency of 25kHz and are also water cooled. Each PS is controlled by a dedicated DPC-controller and an associated high-precision DPC.

Figure 3.4.5.7 shows the allocation of the different PS to the magnets with rated currents of 50A and more (large magnets) and visualizes series connections of magnets.

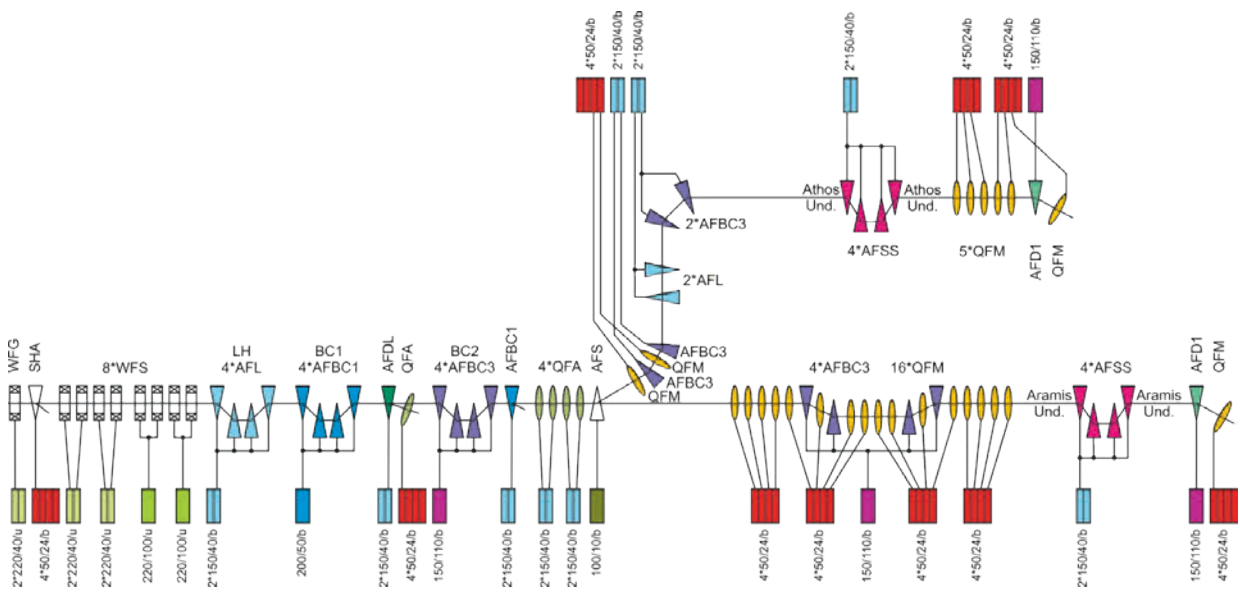


Figure 3.4.5.7: Schematic overview of SwissFEL magnets and power supplies with current ratings of 50A and more.

### 3.4.6 Septum and Kicker systems

SwissFEL operation is planned with two electron bunches per RF macro pulse at a repetition rate of 100 Hz. The electron bunches are separated by 28 ns. One electron bunch will continue through the ARAMIS undulator line, the other bunch will be deviated by the kicker and septum systems towards the ATHOS undulator line. The general approach is to use a kicker magnet to give a small, fast vertical deflection, then to follow with a Lambertson septum magnet, which gives the large but stable horizontal angular deflection. From previous experience with septa at PSI, a beam separation at the septum entrance of 10 mm is a good compromise. The choice of vertical kickers and horizontal (Lambertson) septum decouples the stability performance of the two systems. The tolerances are divided equally between amplitude and time jitter. The results are shown in Table 3.4.6.2.

Beam energy	3.15 GeV
Relativistic gamma	6165
Bunch separation (max rise time)	28 ns
Deflection angle	35 mrad (2°)
Available length	~ 9 m
Vertical beam separation at septum entrance	10 mm

Table 3.4.6.1: System parameters.

Kickers type	Resonant (bipolar), vertical
Number of kickers	2
Kickers total deflection (V)	1.75 mrad
Kickers stability (V)	< 130 ppm rms (0.23 μrad)
Kickers amplitude stability	< 90 ppm rms (0.16 μrad)
Kickers time stability	5 ppt relative to cycle 32 mrad rms @ 17.86 MHz
Septum Type	DC Lambertson, horizontal
Septum deflection	35 mrad (2°)
Septum stability (H)	< 6 ppm rms (0.21 μrad)

Table 3.4.6.2: Error budget for kickers and septum (V - vertical, H - horizontal).

Parameter	Given	Derived
Beam energy (plus 10% reserve)	3.465 GeV	
Magnet gap length	790 mm	
Total angle deflection (peak-to-peak)	1.8 mrad	
Amplitude angular deflection	±0.9 mrad	
Bending radius		880 m
Field intensity		±6.6 mT
Magnet gap width	16 mm	
Number of turns	1 turn	
Resonator frequency	17.86 MHz	
Resonator unloaded Q-factor		~880
Magnet inductance		380 nH
Magnet capacitance		210 pF
Current		±300 A
Voltage		±13.6 kV
Stored energy		18.5 mJ
Pulse repetition rate	100 Hz	
Magnet duty cycle	1%	
Resonator power loss		~20 W

Table 3.4.6.3: Kicker parameters.

Parameter	Given	Derived
Beam energy (plus 10% reserve)	3.465 GeV	
Magnet gap length	0.8 m	
Deflection angle	35 mrad	
Bending radius		22.9 m
Field intensity		510 mT
Magnet gap width	65 mm	
Magnet gap height	7.2 mm	
Number of turns on magnet	41 turns	
Magnet current		113 A
Magnet resistance		32 mΩ
Magnet dissipation		406 W
Magnet inductance		232.8 μH
Stored magnetic energy		1.5 J

Table 3.4.6.4: Septum parameters.

With present pulser technology (based on thyratrons or step recovery diodes), the risks of high voltage, the difficulties of short rise time and requirement for lowest possible jitter gave the impetus to find an improved solution. Consequently, the kicker has been implemented as a novel system using a high Q factor lumped-resonator with a resonant frequency of 17.86 MHz, phase locked to the linac RF and driven by MOSFET driver.

The general parameters for the kickers and the septum are given in Table 3.4.6.3 and 3.4.6.4. The kickers are an in-vacuum design, a lumped resonator with no magnetic core. The lumped resonator is driven at a low impedance tapping point, giving a lower driving voltage which has two major

advantages: it relaxes the electrical vacuum feedthroughs' requirements; it utilizes fully solid-state driver design which is a prerequisite for long and reliable service life.

The septum is a Lambertson design with only half in vacuum. The magnet is supplied by a high stability DC power supply. The Lambertson geometry ensures small leakage magnetic field for the straight beam (~1 ppt of the dipole field). An integrated shorted single turn on the core ensures filtering of unwanted AC current components. The half in-vacuum design reduces the necessary vacuum volume and leaves the electric winding with epoxy insulation in the air side. The magnet's winding is water cooled.

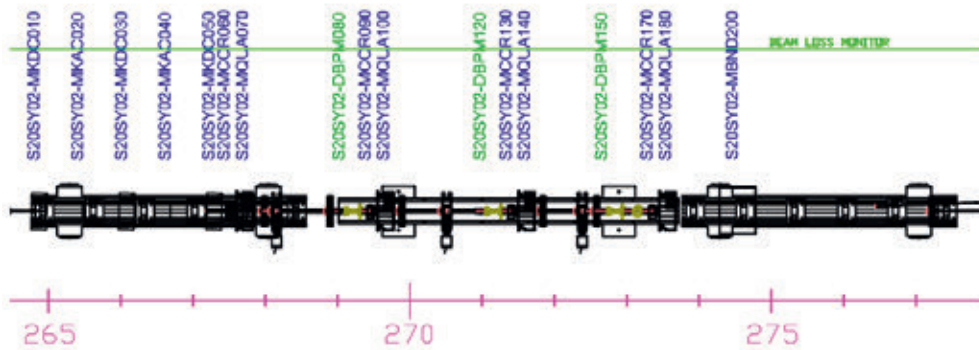


Fig. 3.4.6.1. Kicker and septum layout, with intervening quadrupoles.

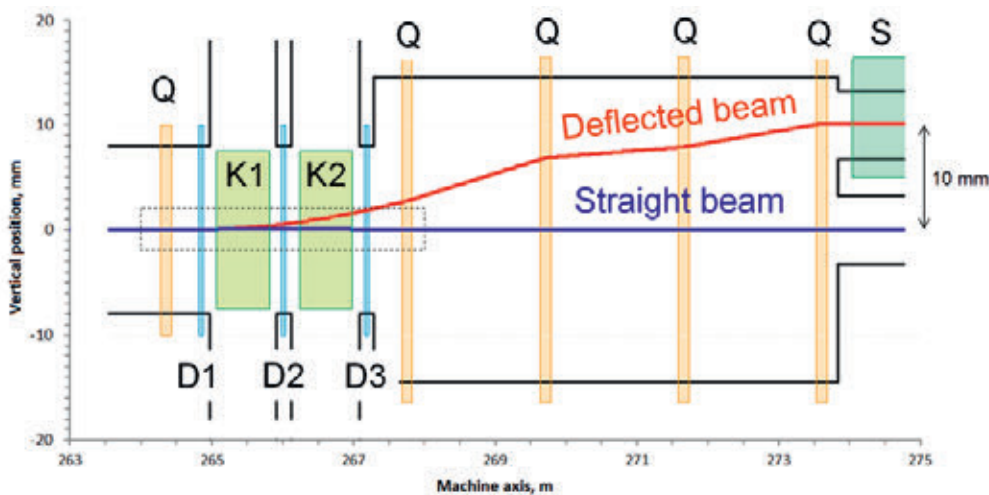


Fig 3.4.6.2. Beam trajectory and field regions in switchyard.

### 3.5 Undulators

The SwissFEL will have two undulator lines. The one for hard X-rays from, 7 Å (2 keV) to 1 Å (12.4 keV), with an electron energy of 5.8 GeV, is named Aramis. The second one, covering the entire soft X-ray range, from about 200 eV to 2 keV with full polarization control, is named Athos.

The undulator design for the Athos line is based on PSI's experience with APPLE II type (Advanced Planar Polarized Light Emitter) undulators.

The emitted photon wavelength is given by the following resonance condition for planar undulators:

$$\lambda = \frac{\lambda_U}{2\gamma^2} \left( 1 + \frac{K^2}{2} \right)$$

where electron energy  $\gamma = E/E_0$ , the period length of the undulator is  $\lambda_U$  and the magnetic field  $B$ .  $K$  is defined by:  $K = 0.0934 \times B[\text{T}] \times \lambda_U[\text{mm}]$ .

All undulators will be based on permanent magnet technology, with its well-established optimization concepts. Electromagnetic alternatives do not deliver sufficient magnetic field strength and superconducting undulators do not yet deliver the required field quality.

#### 3.5.1 Athos undulator

The basic concept to cover the full range from 250 eV to 1900 eV is to combine the  $K$  tunability of the undulators with variable beam energy. An APPLE X type undulator [7] with 38 mm period length (UE38), in combination to a variable extraction energies from 2.9 to 3.15 GeV and the Athos linac

(+/- 250 MeV), is capable of covering the entire wavelength range from 250 eV to 1.9 keV on the fundamental harmonic. The exact photon energy range depends on the maximum undulator parameter  $K$  (up to 3.6) in the various modes of operation: Linear polarization continuously changeable from 0-180°, as well as circular.

Operation of the APPLE X undulators is more challenging than with the in-vacuum undulators. Firstly, because of the different modes of operation, and secondly, the electron trajectory lies in the fringe field of the four magnet arrays. Although these pure permanent magnets have no iron poles, their magnets have a permeability which differs slightly from unity. This results in nonlinearities (hysteresis), which are the source of a variation in the field integrals when shifting the magnet arrays. Those nonlinearities also lead to distortions of the cosine behaviour of the magnetic field, which are responsible for small errors in the prediction of the energy and polarization. Samarium-cobalt ( $\text{SmCo}_5$ ) shows significantly smaller nonlinearities in comparison to  $\text{NdFeB}$ . In addition, it shows a smaller temperature dependency, a larger resistance to radiation induced demagnetisation so that samarium-cobalt seems to be a serious candidate, although it is more delicate to handle because it is more brittle compared with neodymium-iron-boron.

For the UE38 apple undulator, the first concept is to use a  $\text{SmCo}_5$  for the magnets that are longitudinally magnetized and  $\text{Sm}_2\text{Co}_{17}$  for the radially magnetized magnets. In addition the radial magnets will be magnetized using the field shape techniques (non uniform magnetization) so that the magnet field at the tip of magnet, near the beam, could be up to 10%

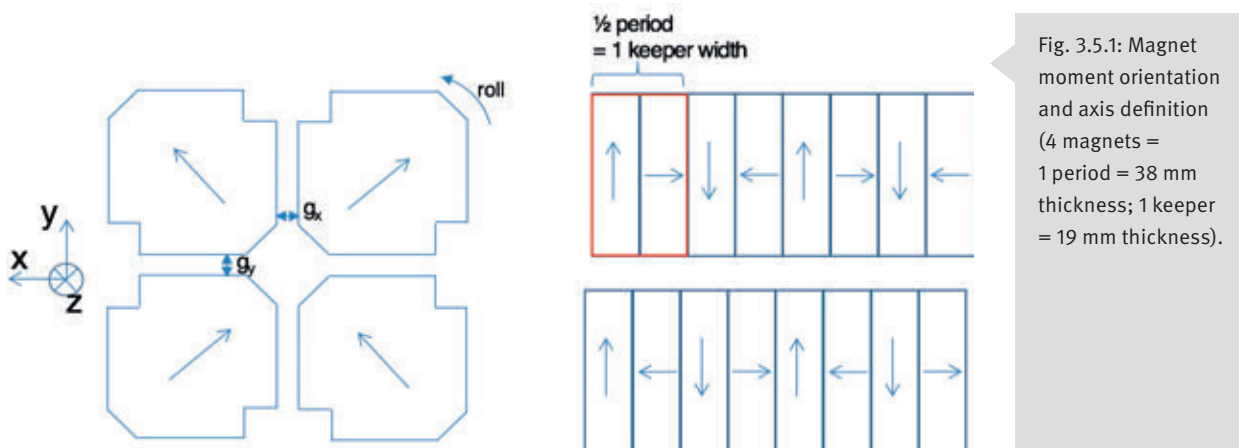
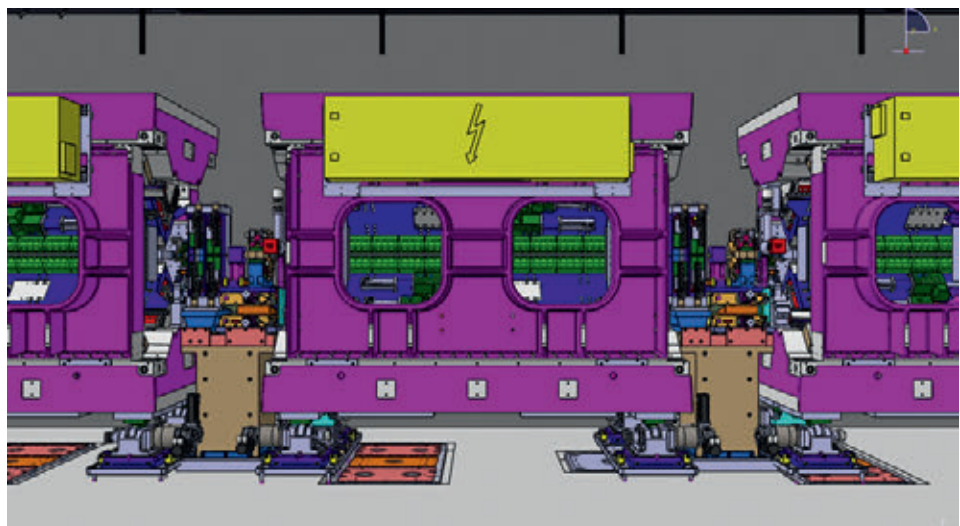


Fig. 3.5.1: Magnet moment orientation and axis definition (4 magnets = 1 period = 38 mm thickness; 1 keeper = 19 mm thickness).

Table 3.5.2: The main parameters of the Athos undulator line.

Name	UE38	comments
Period	38 mm	
Gap / Slit range (in x and in y)	3–21 mm	
K	3.6-0.9	3.6 being the minimum requirement
Minimum aperture diameter	6.5 mm	
Minimum speed for gap variation	1 mm/s	
Magnet material	SmCo	
Remanence	1.08	
Type	APPLE X	
Number of segments	16	
Longitudinal shift range (polarisation)	+/- 21 mm	+/- half a period
Segment magnetic length (including end magnets)	1985 mm	
Number of full period per undulator	50	
FODO lattice 1/2 period length	2.8 m	
Maximum Force between two keepers	+/- 160 N	2 magnets / keeper
Gap reproducibility	1 um	in U15 the reproducibility was better than 1 um
roll position reproducibility for a given array configuration	< 100 urad	this is the deformation in (x,y) plane
Position tolerance in x (transverse to beam axis)	+/- 50 um	Since good field region is 60 um (for 10 <sup>-4</sup> ) 100 mu for 5 10 <sup>-4</sup>
Position tolerance in y (transverse to beam axis)	+/- 50 um	Since good field region is 60 um (for 10 <sup>-4</sup> ) 100 mu for 5 10 <sup>-4</sup>
Position tolerance in z (collinear to beam axis)	+/- 100 um	Since good field region is 60 um
Shimming range of each individual keeper at 45 degrees	+/- 100 um	to compensate inner I beam non linearity (+/- 30 um) and magnets errors (1%; 1 deg <=> 30 um)
magnetic field amplitude variation from block to block	1 %	
magnetic field moment angular orientation error	0.77 degree	

Fig. 3.5.2: Layout of the Athos undulator line: the undulator segment with an inter-undulator section is 2.8m long.



Magnetisation	longitudinal	transverse
grade	SmCo <sub>5</sub>	Sm <sub>2</sub> Co <sub>17</sub>
Trade name	Recoma 22	Recoma 28
radiation hard	yes	yes
Br[T]	0.94	1.1
dB/dT [%/K]	-0.045	-0.035
permeability	1.01 parallel; 1.04 perpendicular	1.06 parallel; 1.15 perpendicular
mech. prop.	brittle	ok
suitable for	UE38	UE38

Table 3.5.3: Material parameter permanent magnets.

larger than with a uniform magnetization. This mix of two magnet types would combine the advantage of high Br (Sm<sub>2</sub>Co<sub>17</sub>) and small hysteresis of SmCo<sub>5</sub>. With this combination the maximum K value could be as high as 3.9 for the circular polarization (elliptic to perfect circular) and between 2.8 and 3.9 for the inclined polarization (see Fig. 3.5.3).

### 3.5.2 Undulator module

The expected saturation length of Athos varies with the electron energy, but should not exceed 30 m. Including in-

ter-undulator space, this means for Athos a total length of 45 m. The undulator has to be segmented to allow space for focusing, beam diagnostic and electron beam corrections (see Figure 3.5.4). Undulator segments are inserted in a periodic FODO section where quadrupole magnets are separated by 2.8 m (FODO period = 5.6 m). This leaves 800 mm for the inter-undulator segment components.

An undulator module consists of a 2 m-long undulator, a 4 dipoles magnetic chicane unit (CHIC), a cavity beam position monitor (BPM) and a quadrupole (QFF). In addition, there are steering magnets SFU (for vertical and horizontal corrections) at each extremity of the undulator together with an earth magnetic field corrector all along the vacuum chamber. Small quadrupoles made with permanent magnets (QFU) are also installed at each undulator extremity for alignment purposes. These QFU can be retracted after alignment of the undulator axis onto the electron beam trajectory. The QFUs are installed on the same undulator frame and aligned with respect to the undulator axis in the magnetic measurement laboratory (MML).

The inter undulator segment is completed by a bellows and a sector valve (SV), for a total length of 800 mm. For the athos undulator, pumping will be done through the vacuum valve.

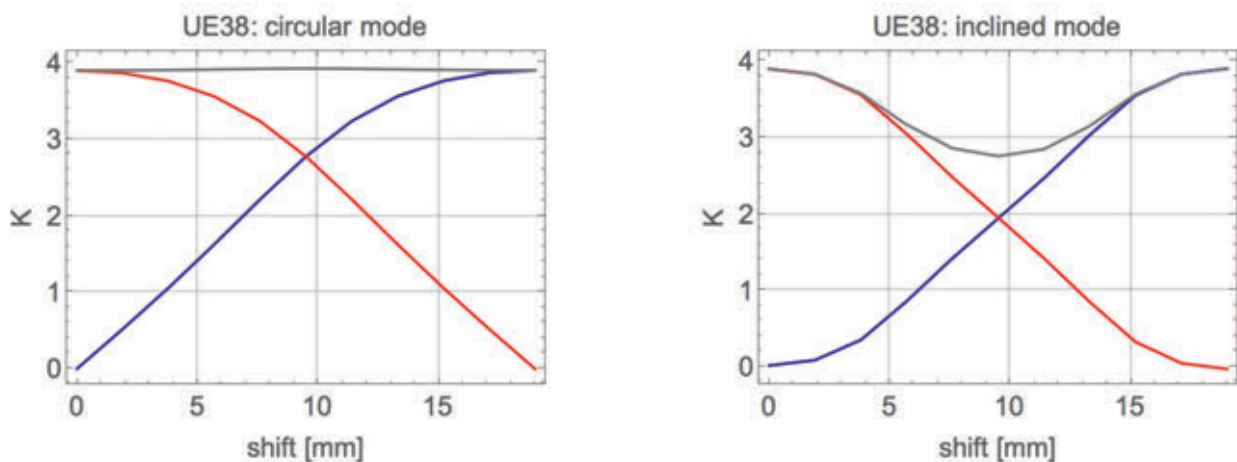


Fig. 3.5.3: K value in the horizontal direction (blue) and the vertical direction (red) and the sum (black) versus the longitudinal shift of the magnet arrays. In circular mode, bottom-left and top-right arrays are shifted by a quarter magnet period in respect to bottom-right and top-left-arrays. In inclined linear polarization, bottom-left and top-right are shifted in opposite direction while other two arrays stay unchanged.

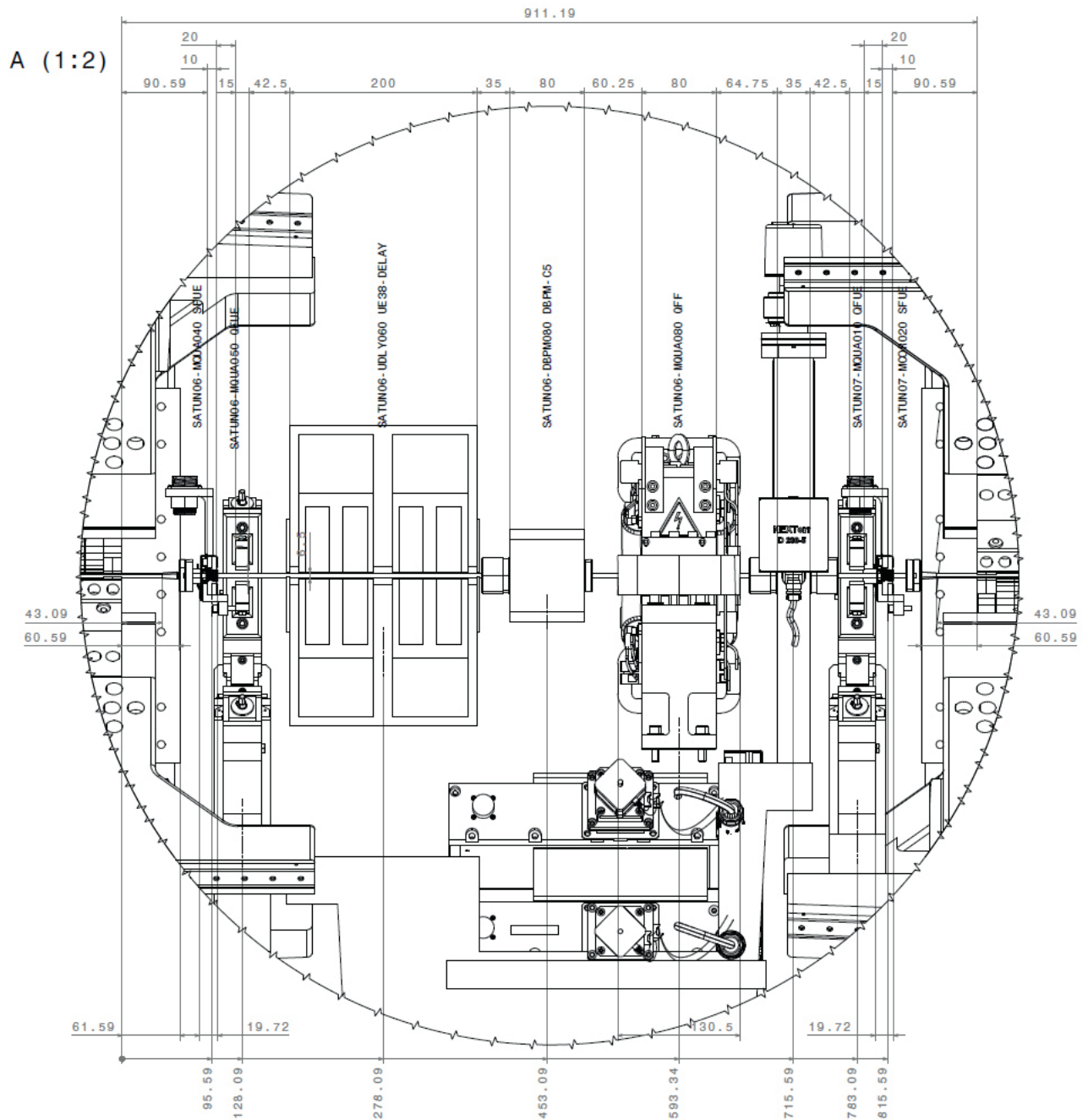


Fig. 3.5.4: Inter undulator section (0.8 m long): from left to right: correctors (SFUE); alignment quadrupole (QFU), magnetic chicane (CHIC), Beam Position Monitor (BPM); FODO Quadrupole Magnet QFF; vacuum valve; alignment quadrupole (QFU); correctors (SFUE).

### 3.5.3 Mechanics

Athos undulator has a different support frame than Aramis undulator, see Figure 3.5.5. This consists of two identical pairs: the lower and the upper “base” and the two sides. This new approach increases the symmetry with respect to the classical C frame adopted for synchrotron light sources and allows for more compact solutions. The main disadvantage is decreased accessibility to the magnet region. The functionality of the frame is also changed, and it now plays a central role in the rigidity of final magnet configuration. The frame material is cast iron which is easier to machine in comparison to the mineral cast used in Aramis undulator. The particularity of the Apple X design is that magnet arrays can move along an axis at 45 degrees angle relative to the vertical or horizontal axis. In addition magnet arrays can also move along the longitudinal axis like any APPLE device. This means that gap and slit always open by the same amount. This mechanical arrangement has several advantages:

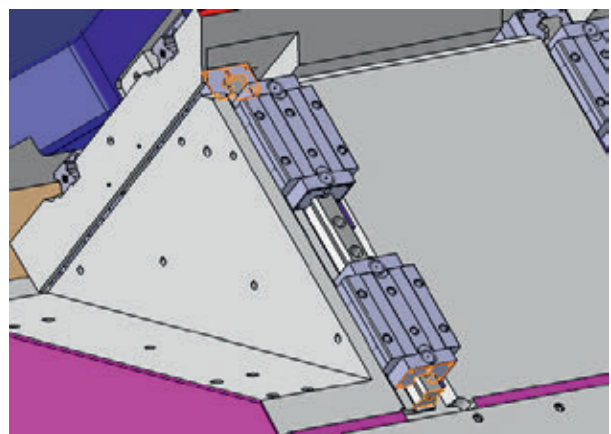
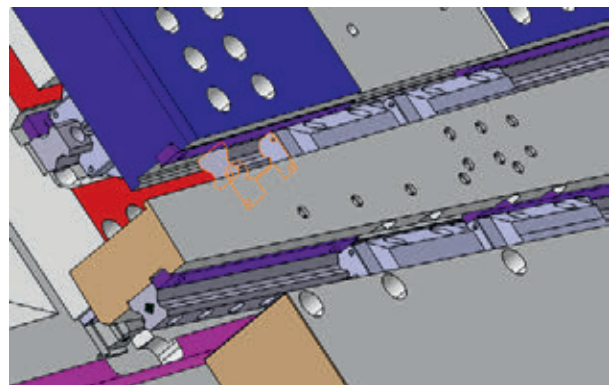
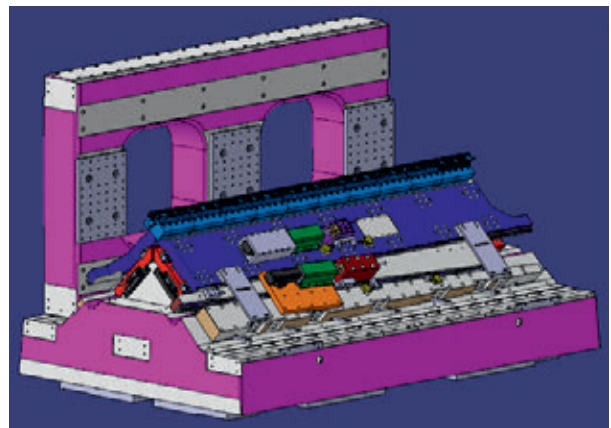
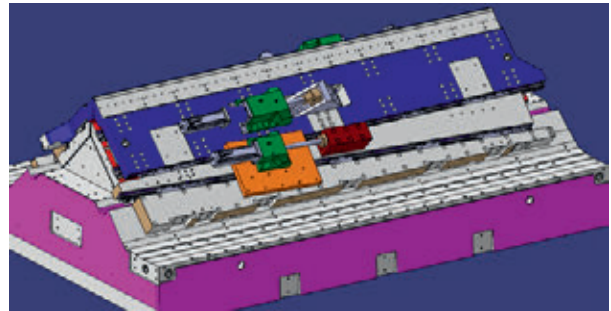
- the longitudinal motion of magnet arrays along the z axis to change the polarisation is decoupled from the radial motion (K changes).
- scanning the K value at constant polarisation is much simpler than in APPLE II devices since you just open the aperture (no need of longitudinal shift compensation)
- the distribution of the forces between vertical and horizontal planes is more symmetric
- a transverse gradient of the magnetic field can be introduced by opening only one half of the undulator.

On Fig. 3.5.5, the blue part is the iron cast part that moves longitudinally on two rails thanks to a motor / shaft situated in the center. The red part moves radially thanks to a motor/wedge system.

An electron beam height of 1200 mm can be realized with this concept, allowing the hosting of the vacuum chamber, the screwing robot or the hall probe measuring bench. The entire module with a weight of 13 tons can be aligned in 5 degrees of freedom by means of the eccentric camshaft movers, which have also been used for the Aramis undulators.

Besides the support structure, solutions for the keeper, which holds the permanent magnets, are also being studied. Those designs allow adjustment of magnet position with

Fig. 3.5.5: 3D global views of UE38 undulator: Bottom part of the frame (top) and with one side wall (middle) and detail view of the wedge and guiding rails of the radial motion at 45 degrees angle (bottom).



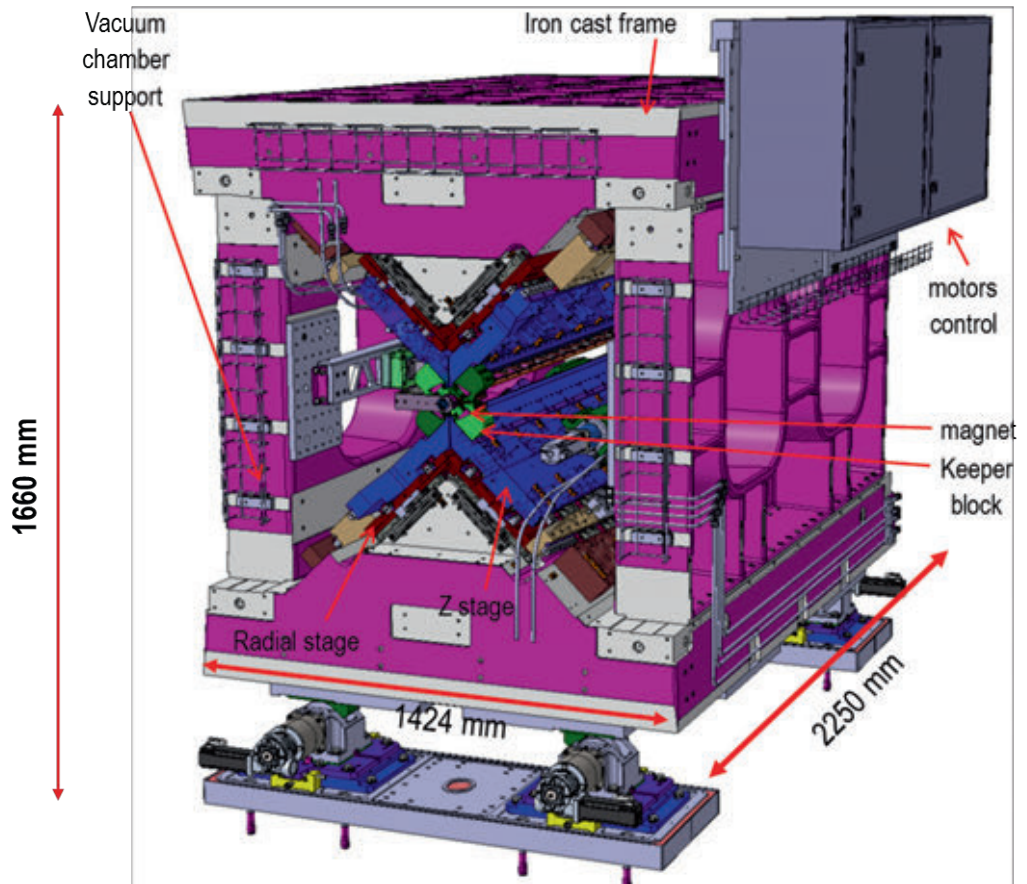


Fig. 3.5.6: Global views of UE38 undulator with reference to the different components.

the help of a single screw to a precision of less than  $1.5 \mu\text{m}$  (see Figure 3.5.7).

In order to improve individual magnet positioning precision, stiffness and cost, the 50 periods of one segment will be distributed over 12 block-keepers and 2 end-block-keepers (Fig. 3.5.7 and 3.5.8). Each block is 152 mm long and carries 4 undulator periods. The block-keepers are made out of

aluminium and magnet pairs are clamped on the keeper but can still be adjusted vertically independently from neighbouring  $\frac{1}{2}$  periods. The keeper is a flexor system and is preloaded by the wedge below the magnets. With the screw up to  $\pm 100 \mu\text{m}$  can be continuously adjusted.

First the vertical trajectory will be corrected and then horizontal trajectory and phase with the wedge.

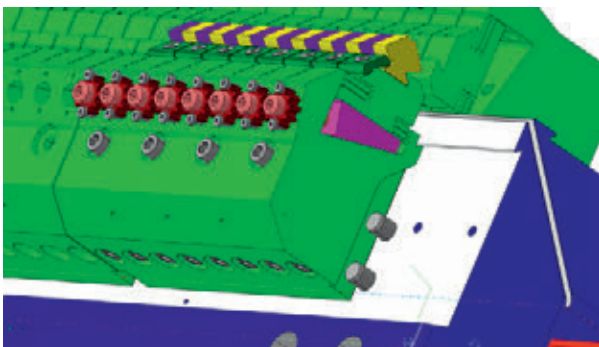


Fig. 3.5.7: 15 cm long block-keeper for 4 periods. The block is partially cut in slices (wire eroded) to allow vertical adjustment of individual pairs.

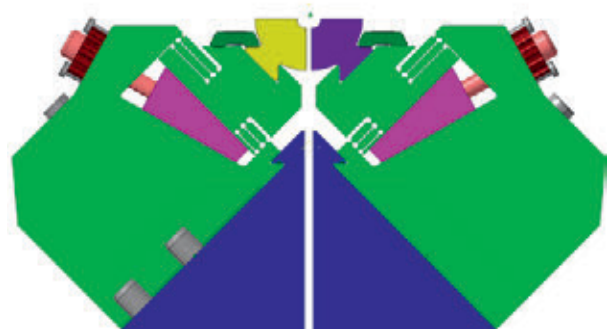


Fig. 3.5.8: Front view of the keepers holding the magnets at 45 degrees in the undulator Athos.

### 3.5.4 Inter-undulator magnetic delay chicane design

The magnetic delay chicane installed between undulator segment has to fulfil several purposes. In the normal SASE operation mode the chicane is used as a phase shifter (like in the Aramis line). In the undulator, the electron bunch accumulates a delay of exactly one radiated wavelength period after each undulator period (38mm). In the inter-undulator section this delay is different and a phase matcher is required to maintain perfect overlap between microbunching and radiated wavelength. This phase matching function requires a quite low magnetic field and thus the chicane will be operated with a gap open to 70 mm.

For the optical klystron mode of operation the magnetic chicane is used as a buncher chicane (compression) in order to convert an energy modulation in a density modulation. There stronger magnetic field is required and the gap has to be closed down to the minimum value of 6 mm depend-

Parameter	Value
Maximum chicane length	200 mm
Required delay (at 3.4 GeV)	2 $\mu\text{m}$ or 7 fs
Required horizontal shift (at 3.4 GeV)	250 $\mu\text{m}$ (and 5 fs delay)
Minimum gap	6 mm
Maximum gap	100 mm
Nominal gap for phase matching	70 mm
Minimum step in gap adjustment	2 $\mu\text{m}$
Reproducibility in gap setting	10 $\mu\text{m}$
Maximum magnetic force per motor axis	1500 N / motor axis
Maximum magnetic force whole chicane	3000 N

Table 3.5.4: Magnetic chicane parameters requirements.

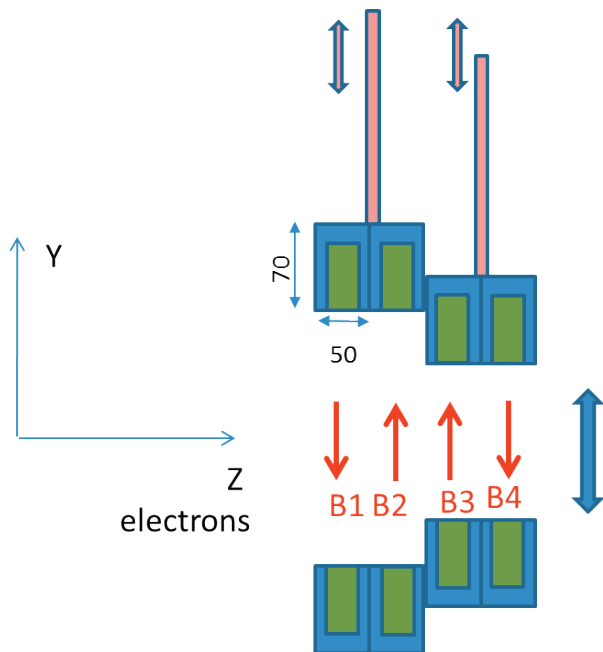


Figure 3.5.4.1: Conceptual magnetic chicane with 4 magnet pairs. The two halves of the chicane can be moved independently in order to generate transverse kick to the electron beam trajectory.

ing on the required R56. For the high brightness mode, the goal is to delay the electron bunch and so operation range is similar to the optical klystron mode. For the TW pulse mode, the electron bunch is delayed and shifted transversally so that only half of the chicane is closed. If only the half of the chicane is closed then the electron bunch will experience an offset kick in the horizontal plane.

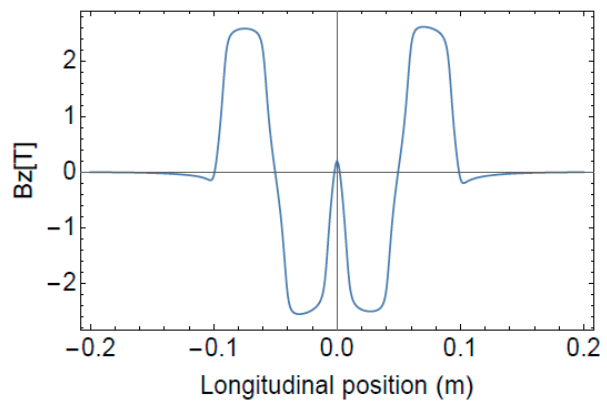


Figure 3.5.4.2: Magnetic field profile along the longitudinal z axis of the chicane. RADIA Simulation done with NdFeB magnets / poles combination.

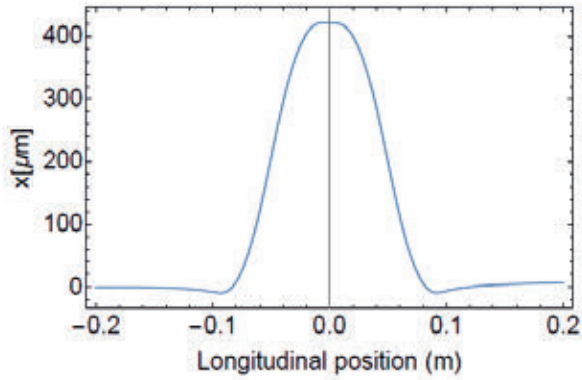


Figure 3.5.4.3: Electron beam trajectory when the gap is closed at 6.5 mm. Electrons deviate by 400  $\mu\text{m}$  in the central two dipoles (RADIA simulation).

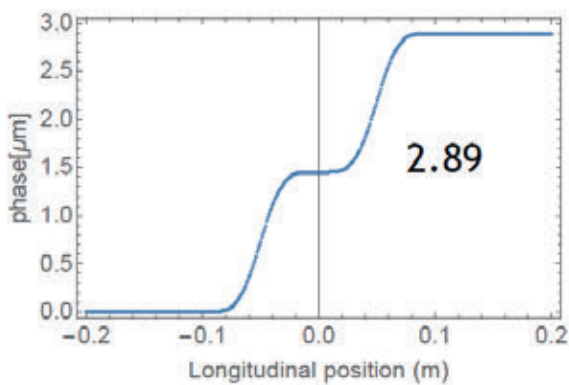


Figure 3.5.4.4: Cumulated path delay (2.89  $\mu\text{m}$ ) of the electrons over a straight trajectory (RADIA simulation).

Fig.3.5.4.1 shows a schematic concept of the chicane where the gap of each half of the chicane can be adjusted independently. The overall length (along the beam line) of the device should not exceed 200 mm. The required parameters of the chicane are summarized in the table 3.5.4. The mechanical design of the magnetic chicane (Fig. 3.5.4.5) is a C shape where magnets are attached to a spindle. The spindle is moved by a DC motor via a belt. The C shape has to stay stable for forces up to 2400 N. Magnets are sitting

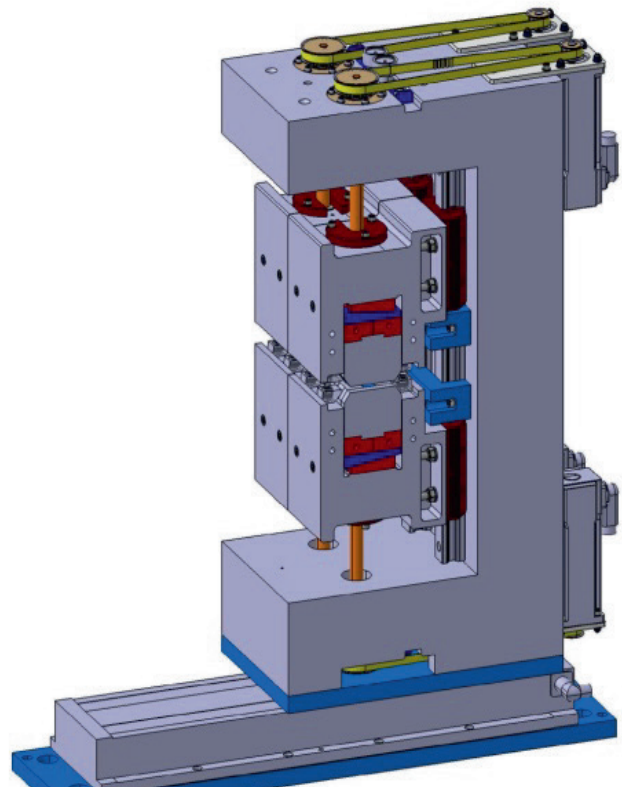
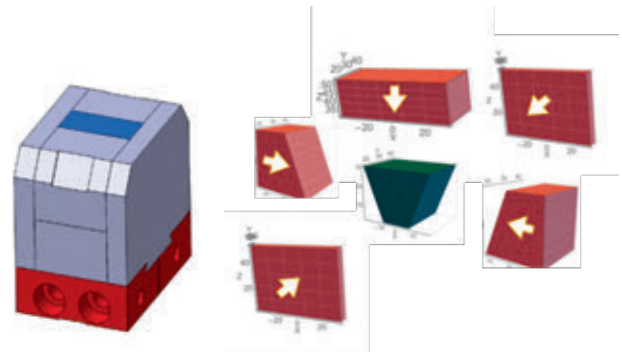


Figure 3.5.4.5: Individual magnet block assembly with a central iron pole (top) and mechanical design of the chicane (bottom) where these magnets are installed.

on a small wedge for shimming; the integral of the magnet field should be zero at all gap to avoid kick in the electron trajectory.

### 3.5.5 Undulator tolerances

#### 3.5.5.1 Error Sources in the undulator lines

The FEL process can be affected by two types of errors within the undulator beamline:

- mismatch in the transverse overlap between the gain – guided optical mode of the radiation field and the electron beam
- synchronization mismatch between the electron micro-bunching phase and the radiated field phase.

Table 3.5.5 summarized the expected stabilities and precisions for the current undulator design and environmental parameters.

Gap variation in UE38: 10µm radial gap change corresponds to a relative field variation of 1e-3. If the gap can be controlled with 1 µm precision then the corresponding change in the FEL photon energy is 0.2 eV (for 1.9 keV photons).

#### 3.5.5.2 Measurements and Alignment of Undulator magnet arrays

The alignment of individual periods of one undulator segment will be performed in the magnetic laboratory of the

SwissFEL building around 100 m away of the final position of the undulator. The ambient air in the magnet laboratory is regulated like in the undulator hall to 24 degrees +/- 0.1 degrees. Careful transport of the undulators (after alignment) to their final place will be done with wheels and/ or air cushion based systems.

Two techniques are foreseen for the alignment and characterization of the undulator segment. With a Hall Probe, the B(z) will be measured along the undulator segment. The trajectory angle ( $\int B \cdot dz$ ) and offset ( $\int \int B dz$ ) is then calculated locally (at every magnet period) and corrected by vertical adjustment of the incriminated keeper support. This adjustment insures a good transverse overlap of the electron beam and radiated field during the FEL process.

Equally important for the FEL process is the synchronization between the radiation and the electron bunch and this requires perfect periodicity of the magnetic field B(z). In consequence, the local phase variation (or the difference in electron excursion time at each period) over the entire segment is also measured and corrected also by adjusting the gap height locally.

In complement to the Hall Probe measurements, stretched wire techniques are used to determine trajectory offset and angle after a full undulator segment.

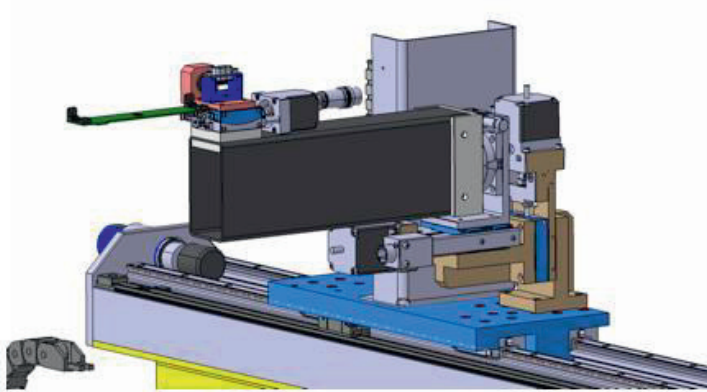
The measurements and adjustment of the local magnetic field is illustrated in Fig. 3.5.5.1 and is described in [40]:

Expected Stability and Precision:		unit
Residual field integral over one segment	40	µT.m
Air Temperature stability over 24 h and over 5 m	0.1	K
Air Temperature stability over week and over 60 m	1	K
Uniformity of K value over 1 segment	10 <sup>-4</sup>	
Phase shake tolerance per segment	2.5	°/ λ <sub>r</sub>
Mechanical tolerances for magnets / pole dimensions	20	µm
Precision in magnetic remanence Br	1	%
Good field region width (where dB/B < 1e-3)	240	µm
Good field region height (where dB/B < 1e-3)	240	µm
Minimum Gap increment (1G)	0.3	µm
Magnetic Field Resolution	1	G
Straightness of inner I-beam undulator (over 2 m)	100	µm
Magnetic Field Measurement Art	Hall Probe	
Magnetic Axis Determination Technique	stretched wire	

Table 3.5.5: Expected stabilities and precision for undulators and environmental parameters.

## Hall probe and screwer on common linear motor

Hall probe



Screwing slave

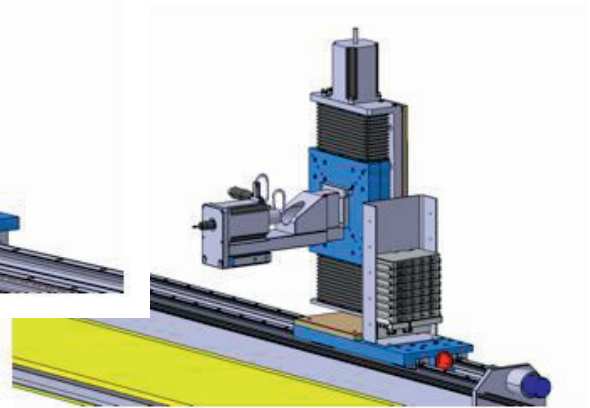


Fig. 3.5.5.1: Motorized Hall probe Measurement and adjustment of gap to compensate field variations along Athos undulators.

### 3.6 Electron beam diagnostics concept

Electron beam diagnostics have to provide a full set of instrumentation for all SwissFEL operation modes, to accommodate three major tasks:

- Support accelerator commissioning and machine start-up (e.g. during SwissFEL commissioning, but also after shut-downs and future upgrades) by permitting the measurement and optimization of all electron beam parameters within an extended dynamic range.
- Provide, where possible, online information about all relevant beam parameters to the control room, to allow day-by-day operation of the SwissFEL user facility in a reliable and reproducible way.
- Provide input to a set of beam-based feedback loops, which will automatically stabilize the electron, and therefore also the photon, beam over longer time periods.

In addition, the designs of the diagnostics systems have to be robust and reliable, to enable 24h / 7d operation of the final SwissFEL user facility. Wide ranges of parameters – starting with the commissioning phase and extending to

user operation modes – have to be incorporated in the designs, and full integration in the control system is a prerequisite for efficient support of machine operation. High data acquisition bandwidths, low-latency data processing and data transfer (over high-speed fibre links) have to be incorporated in all of the feedback-ready monitors (e.g. beam position monitors (BPM) or synchrotron radiation monitors (SRM)). All dedicated diagnostics sections will be designed to be an integral part of the standard SwissFEL beam optics, to allow the measurement, optimization and control of beam parameters with standard accelerator settings.

Although some of the stability requirements are still preliminary at this stage of the project, the two standard SwissFEL beam optics – the so called “200 pC” and the “low charge 10 pC” modes – provide the baseline parameter set for the design of the diagnostics systems.

#### 3.6.1 Overview electron beam diagnostics

The different diagnostic tools foreseen in the Athos branch of SwissFEL are listed in Table 3.6.1 with their respective locations and purpose.

Table 3.6.1: Overview list of the different electron beam diagnostic (except Beam Position Monitors BPMs) along the Athos line.

Section	z (m)	Component Type	Purpose
<b>SCREENS</b>			
SATSY03	326	Screen, Profile Monitor, High Resolution, DN16, vacuum components only, Camera location right	Screen after Tripple bend achromat: to check beam quality after kicker, septum, ...
SATCL01	332	Screen, Profile Monitor, High Resolution, DN16, vacuum components only	Screen located between the 2 first dipoles of the energy collimator (in the dispersive section) just before the collimator. To measure energy spread before before filtering.
SATMA01	381	Screen, Profile Monitor, HR, DN8, but initially with slow camera and optics	Screen located after the Athos linac to check beam matching in the undulator line.
SATBD01	493	Screen, Profile Monitor, High Resolution, DN16, one screen	Screen located downstream the post-undulator deflecting cavity and used for slice emittance measurement in X and Y. The screen is also part of the spectrometer arm of Athos beam dump.
SATBD01	499	Screen, Profile Monitor, Overview, DN38	Screen to watch SR or FEL radiation
SATBD02	497	Screen, Profile Monitor, High Resolution, DN16, one screen	Screen located in the spectrometer arm at Athos beam dump to measure energy spread and FEL energy loss using the post-undulator TDS (Electron beam energy versus time with fs resolution).
<b>WIRE SCANNERS</b>			
SATSY03	326	WireScan Monitor DN16	Wire scanner after the Tripple bend achromat section: to check beam quality after kicker, septum, ...
SATDI01	342	WireScan Monitor DN16	Wire scanner after the last dipole of the switchyard: to check matching into the Athos linac
SATBD01	493	WireScan Monitor DN16	wire scanner to measure beam size downstream the X band deflecting cavity
<b>BAM</b>			
SATBD01	343	Beam Arrival Monitor 16 mm Chamber for fs Bunch Lengths with BAM-BOX	BAM used as arrival time clock for users and also to setup the R56 of the switchyard
<b>BLM for Wire scanner &amp; between undulators</b>			
Downstream each wire scanner		Beam Loss Monitor	beam loss detector associated to the upstream wire scanner and also used for Machine Protection System
<b>Bunch Compressor Monitor</b>			
SATDI01	339	Bunch Compression Monitor for IR Bunch Lengths	online monitoring of the compression done in the double bend achromat of the switchyard
<b>ICT</b>			
SATDI01	340	Integrating Current Transformer 16mm Chamber	charge after collimation and transmission through the switchyard section; calibration of switchyard BPMs
SATBD02	495	Integrating Current Transformer 16mm Chamber	charge after dump dipole + calibration of BPMs
<b>Synchrotron Radiation Monitor</b>			
SATCL01	327	Synchrotron Radiation Monitor in the UV spectral range	online measurements of the energy spread in the dispersive section of the collimator
<b>Slotted foils</b>			
SATSY01	281	Ver.Slotted Foil DN16	Vertical slotted foil in the dispersive section before undulator for two colors mode
<b>RADFET</b>			
SATUN	>400	Dose Rate Monitor Right	Accumulated radiation losses between undulators
<b>Longitudinal Loss monitors</b>			
SATSY01	276.6042	Longitudinal Loss Monitor	longitudinal loss fiber to detect location of losses and part of the MPS
SATDI01	355.0747	Longitudinal LM Pulser	longitudinal loss fiber to detect location of losses and part of the MPS
<b>BLM for fast interlock (MPS) to protect undulator</b>			
SATUN02 to SATUN22		Beam Loss Monitor	beam loss detector for interlock purpose – MPS
SATDI04		Beam Loss Monitor	beam loss detector for interlock purpose – MPS
SATBD01		Beam Loss Monitor	beam loss detector for interlock purpose – MPS

### 3.6.2 Description of the different electron beam diagnostics

#### 3.6.2.1 Transverse profile monitors

A detailed description of the transverse profile monitors design for SwissFEL can be found in [41]. These monitors use a cerium doped yttrium aluminum garnet (Ce:YAG) scintillator, which is polished on both sides. To avoid

charge-up, the YAG is coated with indium tin oxide (ITO). The scintillator has a diameter of 20 mm, and two different observation geometries are implemented, to balance resolution with field-of-view. The screens are imaged by an  $f = 200$  mm macro lens to a CCD or CMOS detector. The magnification of the imaging system is 1 : 1.22, resulting in an effective pixel size on the scintillator of  $7.9 \mu\text{m}$ . To fulfill the Scheimpflug imaging condition, the normal of the CMOS detector is tilted by  $14^\circ$  to the optical axis. At this angle, the microlens array on the chip can be used with only minor loss in efficiency. The field of view is horizontally constrained by the in-vacuum mirror to  $\pm 3$  mm.

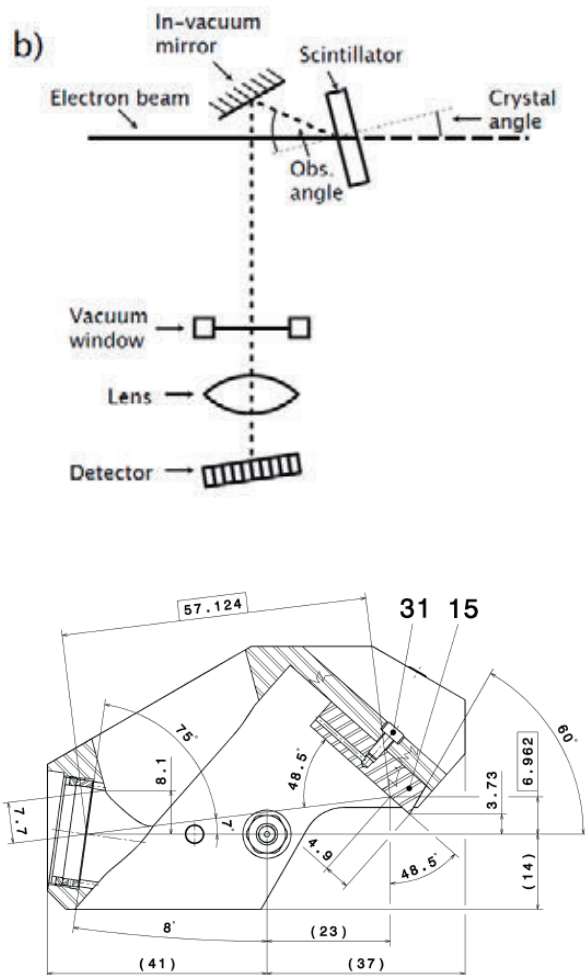


Figure 3.6.2.1: Top: Imaging of the scintillating radiation observing the Snell-Descartes law of refraction as well as the Scheimpflug imaging condition. Bottom: Screen holder for scintillating crystals. Technical drawing, including the scintillator to the left and the in-vacuum mirror to the top right.

#### 3.6.2.2 Wire-scanners and beam loss monitors

A detailed description of the wirescanner design for SwissFEL can be found in [42].

Wire-Scanners can be used to measure the transverse profile of the electron beam in a particle accelerator. Carbon or metallic wires with different diameter ( $D$ ) – stretched on a wire-fork – can be vertically inserted at a constant velocity into the vacuum chamber by means of a motorized UHV linear stage to scan the beam transverse profile with an intrinsic resolution  $D/4$  (rms). An encoder mounted on the linear stage allows the relative distance of the wire from the axis of the vacuum chamber to be measured at each machine trigger event. The interaction of the electron beam with the wire produces a “wire-signal” – scattered primary electrons and secondary particles (mainly electrons, positron and bremsstrahlung photons) – which is proportional to the number of the electrons sampled by the wire in the bunch. The Beam Synchronized Acquisition (BS-ACQ) – over a sufficient number of machine trigger shots – of the wire position and the wire-signal – detected by a loss monitors downstream the wire – allows the beam transverse profile along the horizontal or the vertical direction to be reconstructed. In SwissFEL, view screens and WSCs will be used to monitor the transverse profile of the electron beam which varies between  $500 \mu\text{m}$  and  $5 \mu\text{m}$  (rms) along the entire machine. View-screens will be mainly equipped with YAG crystals. In SwissFEL, only WSCs are in principle able to discriminate the 28 ns time structure of the two-bunches emitted at 100 Hz by the photocathode. The SwissFEL WSCs are designed according to the following criteria, see Fig.

3.6.2.2: use a single UHV linear stage to scan the beam profile in the X,Y and X-Y directions; use Tungsten wire with different diameters from 5 to 13  $\mu\text{m}$  to ensure a resolution in the range 1.5-3.5  $\mu\text{m}$ ; equip each wire-scanner station with spare/different-resolution wires; detect the wire losses in the bunch charge range 10-200 pC and resolve the 28 ns time two-bunches structure of the electron beam; BS-ACQ of the read-out of both the encoder wire position and the loss-monitor; wire-fork suitably designed for routine scanning of the beam profile during FEL operations (no beam interception with the wire-fork); wire-fork equipped with different pin-slots where the wires can be stretched at different relative distances so that the scanning time can be minimized and optimized according to the WSC position in the machine, see Fig. 3.6.2.2.

Scintillator-based Beam Loss Monitors (BLMs) are used at SwissFEL for monitoring the losses, for optimizing beam conditioning, beam measurements with the wire-scanner and Undulator protection. The optical signals from the scintillators will be detected by PMTs which are located outside the accelerator tunnel. The PMT control and signal

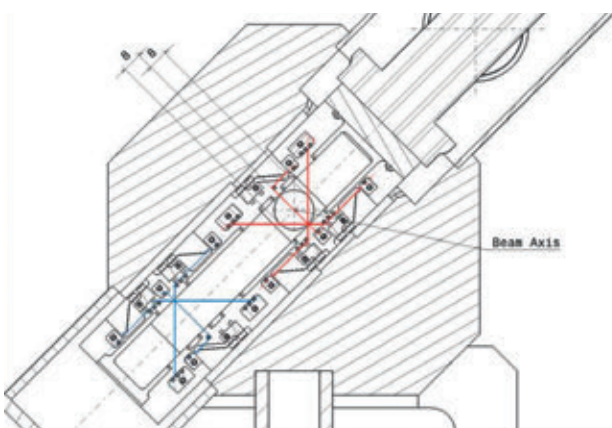


Fig. 3.6.2.2: View of the Transverse section of the WSC vacuum chamber and, in particular, of the wire-fork and of the CF16 vacuum chamber. The wire-fork is equipped with 3 different pin-slots where the wire can be stretched. The distance of the “wire-vertex” from the vacuum-chamber axis can be set at 8, 5.5 and 3 mm in correspondence of the 3 different pin-slots.

conditioning is done via a front-end based on the PSI Analogue Carrier board (PAC). The PAC board allows for amplification/attenuation, offsetting and single-ended to differential conversion of the analog signal, while the Generic PSI Carrier (GPAC) board provides digitization and FPGA-based post-processing, along with bridging the communication to EPICs controls. A fast algorithm was developed to process the signals and trigger the machine protection system (MPS) at 100Hz. A detailed description of the BLMs can be found in [43].

### 3.6.2.3 Beam arrival monitors

A detailed description of the Beam Arrival Monitors (BAM) systems can be found in [23].

### 3.6.3 Beam position monitor system

SwissFEL will have bunch trains of 1–2 bunches at 28ns spacing and 100 Hz bunch train repetition rate, with a fast kicker that distributes each bunch in the train to a different undulator. The injector and main linac BPMs are able to measure the position of each bunch in the train individually. The fast fiber-optic links of each BPM electronics and a latency below 1ms allow the integration of the BPMs into fast transverse trajectory or longitudinal feedbacks (using dispersive BPMs, e.g. in bunch compressors) that operate at bunch train repetition rates up to 100 Hz (see Section 3.11). The SwissFEL BPM electronics will allow remote-controlled selection of the beam charge / beam position range. For the commissioning of the SwissFEL with 1<sup>st</sup> beam and large orbit excursions, a  $\pm 5$  mm range, or more (depending on the beam charge), are possible. During standard user operation, when the beam positions are usually quite close to the BPM centre, a smaller measurement range of  $\pm 1$  mm can be used for lowest (nominal) noise and drift (both scale with the range for the chosen cavity BPM type). If necessary, it is even possible to tune the range of each BPM individually, e.g. for BPMs in special locations, such as the bunch compressor or beam dump, simply by attaching an additional attenuator to the output of the position cavity resonator. The number and locations of BPM can be found in the machine components list (“Heilige List”) [44]. A detailed description of the BPMs can be found in [45].

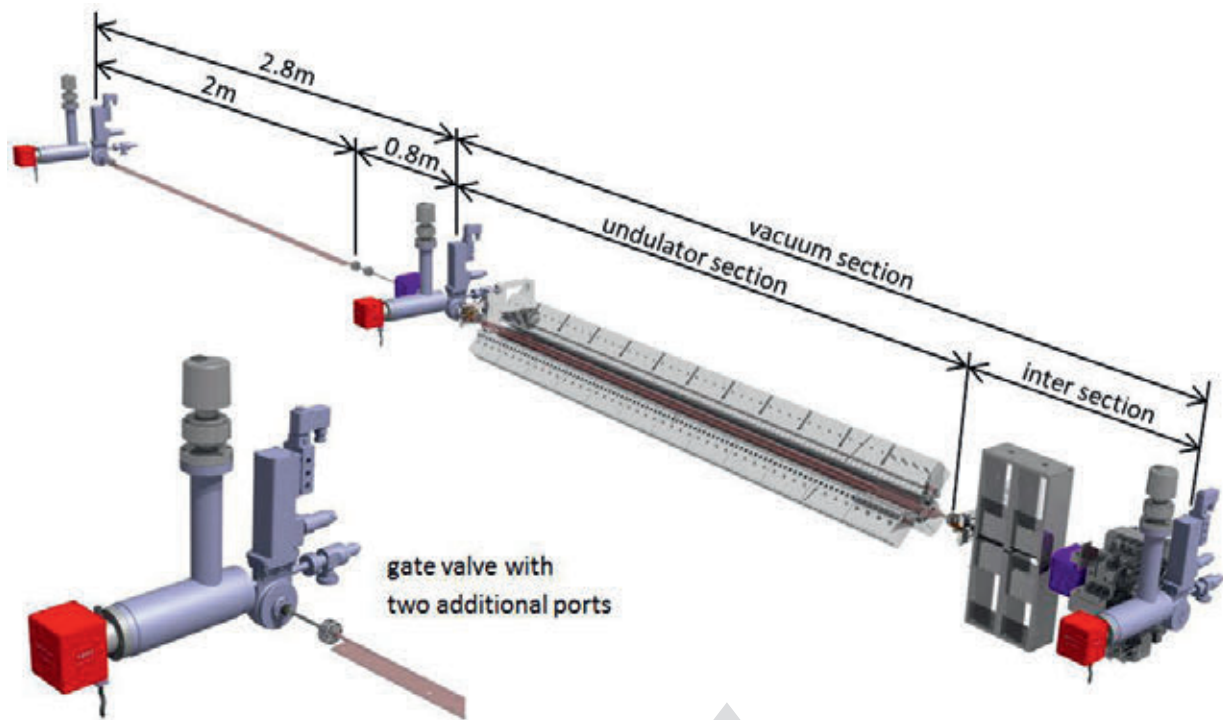


Figure 3.7.1: Arrangement of vacuum components.

### 3.7 Undulator Vacuum concept

#### 3.7.1 Chamber Design

A thin walled tube is used as vacuum chamber for the APPLE undulator Athos. The chamber has an inner diameter of 5mm and a wall thickness of 0.2mm ( $0/+50\mu\text{m}$ ) to allow the required minimum undulator magnet gap. Since low electrical resistance and best performance in magnetic permeability (optimal  $\mu_r=1$ ) is necessary, the vacuum chamber is made out of galvanized copper (oxygen free, high conductive). Total length of the undulator chamber is 2040mm, including the two DN16CF adapter flanges on both ends. The flange material is 1.4429 stainless steel, with copper plated bore hole wall.

The bellows tubes for the intersection will have DN16CF connecting flanges and an inner tube diameter of 5mm as well. Due to the small cross section no RF-shields are built in and an axial gap of 3mm is accepted. The bellows are designed for a 0.1mrad pitch of the undulator vacuum chamber, which is mounted fix to the undulator frame. The flange material is 1.4429 and the tubes and bellows material 316L stainless steel. The inner tube surface will be copper plated.

A smooth surface, with roughness values less than 300 nm, for all inner chamber walls is required to avoid a negative influence on beam performance due to wall wake fields.

##### 3.7.1.1 Production Process

Chamber fabrication will be based on a galvanization method, with the following steps:

A thick wall tube shaped silicon profile with an outer diameter of 5mm and an inner diameter of 0.6mm is threaded on a stranded wire. Then the two adapter flanges with already copper plated bore hole ( $d=5\text{mm}$ ) are threaded on the silicon profile in symmetric arrangement at both ends. With a customized fixture made out of aluminium and electrolyte resistive plastics, the stranded wire will be horizontally strained and the adapter flanges held in position. Then a thin conducting silver layer is deposited on the silicon profile by hand and all electrically conductive surfaces of the flanges and parts, that not supposed to be galvanised, will be shielded.

At this point the thin copper chamber wall is galvanized to the silver coated silicone profile and also to the end flanges. Finally the stranded wire is pulled out and due to the cross section reduction when stretching the silicon, the profile can also be removed by pulling.

Optionally at this stage an electro polishing treatment of the inner chamber walls can be done if the roughness of less than 300nm is not achieved.

After cleaning, bake out and leak testing a stabilizing and supporting 2mm thick copper sheet, is jointed to the vacuum chamber by a second galvanization process. Therefore the tube and the copper sheet are mounted in the fixture in a way that all surfaces except of the joining seams are covered. Like this the outer diameter of the tube and the thickness of the stabilization copper sheet remain and the joining copper is only deposited in the seam.

### 3.7.2 Vacuum Performance

The overall length of an undulator vacuum section is 2.8m, while the undulator itself will have a length of 2m. The APPLE arrangement and the small gap of the undulator magnets don't allow placing vacuum pumps along the undulator. In the intersection are located different focusing and steering magnets, a phase shifter, a beam position monitor and a gate valve. There is no space for separated pumping ports or bulky and heavy ion getter pumps.

For that reason a special DN16CF gate valve with two additional ports will be mounted in each vacuum section. One pumping port for a combined NEG-ion getter pump (NEX Torr D200-5) and a vacuum measurement gauge (Compact Full-Range Gauge) and the second for a venting valve (All-metal angle valve DN16CF). The vacuum sections are respectively pumped from the gate valve at the beginning of each section. Conductance is very limited by the small chamber aperture. The combined NEG-ion getter pump is primarily dedicated for this application because of its low weight, small dimensions and low magnetic stray field. A simulation (MolFlow+) over three vacuum sections shows that an average pressure of  $1.8 \times 10^{-7}$  mbar can be expected. The highest simulated pressure is at  $2.6 \times 10^{-7}$  mbar. The simulation was done with a static outgassing rate of  $5 \times 10^{-11}$  mbar l/s/cm<sup>2</sup> (30% CO, 70% H<sub>2</sub>) and pumping speed of 5l/s for CO and 150l/s for H<sub>2</sub>. An in-situ bake out is not foreseen.

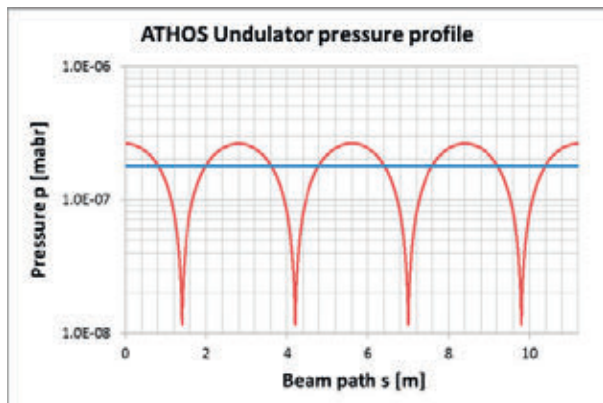


Figure 3.7.2: Pressure profile over 3 vacuum sections of ATHOS undulators.

### 3.7.3 Further steps

The design work for this new vacuum chamber type is nearly completed and the next steps are the manufacturing of the fixture and then the fabrication of the first prototypes.

## 3.8 Mechanical systems

### 3.8.1 Girder Concept

The mechanical support system concept is based on having pre-assembled girders in granite (Fig. 3.8.1.1) where small components (magnets, vacuum pumps, diagnostics, ...) are pre-assembled and aligned. The girder is then mounted on adjustable feet for final alignment in the beamline. The design and alignment concept is identical to the one used in the main linac of Aramis [46,47].



Fig. 3.8.1.1: Granite girder sitting on 4 feet. Each feet is manually adjustable in x, y and z. The components (e.g. quadrupoles) are positioned with shimming blocks on the precisely machined granite surface.

### 3.8.2 Special mechanical systems

#### 3.8.2.1 Dechirpers

The Athos dechirpers consist in 3 sections of 2 m length and 2 sections of 1 m length. For ideal FEL performance, the energy distribution of the bunch electrons along z should be uniform. The problem is that in the injector and in linac 1, a linear dependence of the electron energy with his position along z (so called energy chirp) is voluntary introduced in order to optimize the compression in the magnetic chi-

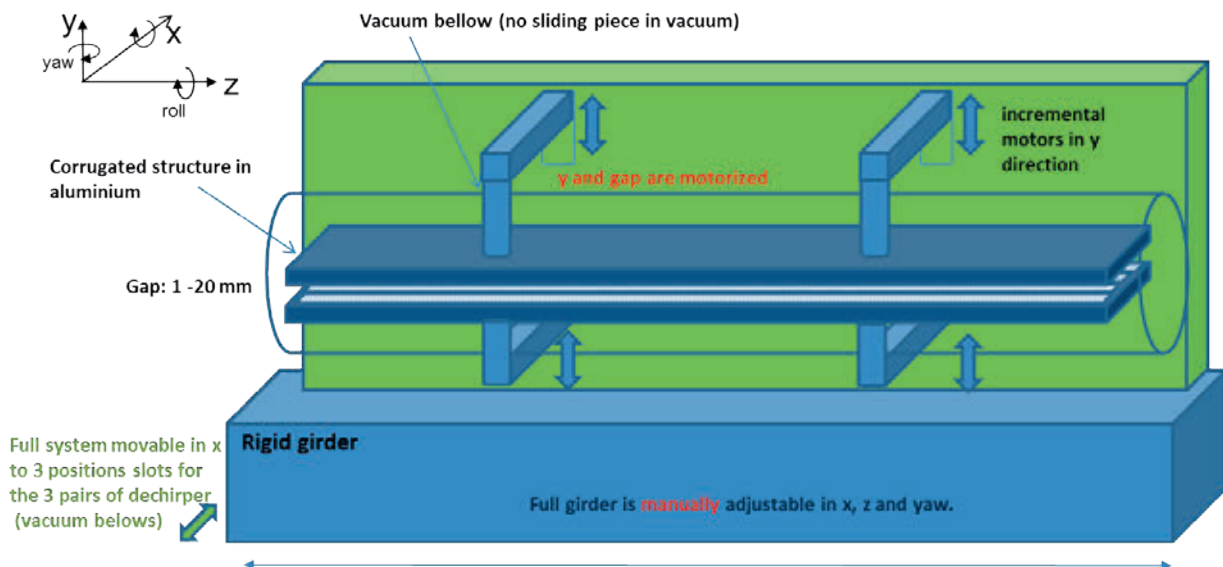
General parameters		Remark
dechirper length	2 m	2 m is the length of active area, flange to flange might be 2.1m
Flatness over 2 m	< 50 $\mu\text{m}$	Gap measuring sensor:
Corrugation design	Table 3.1	
Material for corrugated surface	Aluminum	Copper is also possible
Number of units	3	D1, D2 and D3
Positioning of system	< 100 $\mu\text{m}$	Manual by shimming
X motion range	+/- 2 mm	
Y motion range	+/- 2 mm	
Pitch, yaw and roll motion range	+/- 2 mrad	
Speed of motion for translation In / Out	< 1 mm/s	
Limit switches	yes	

Table 3.8.2.1: Fixed square cross section dechirper Specifications.

canes BC1 and BC2. The purpose of the dechirper units is to remove this linear dependence energy – z by using the wakefields effects. Geometrical wakefields are the electromagnetic waves generated by the traveling electrons which are reflected by the surrounding vacuum pipe. These wakefields act back on the electron bunch. Typically the wakefield generated by the head electrons will slow down the tail electrons. Since the bunch energy chirp is negative (tail's electrons have larger energy), geometrical wakefields will slowly remove the chirp.

In order to control the wakefields and thus the bunch energy chirp, one can design special corrugated surface which enhance this effect: the dechirper. These surfaces are in general metallic with a periodic structure, typically a series of micrometric grooves.

Figure 3.8.2.1: Design principle of the variable gap dechirper unit.



General parameters	
Gap_dechirper length: D4_Gap	1 m
Corrugation design	Table 3.2
Flatness over 1 m (p.t.p.)	<50 $\mu\text{m}$
Material for corrugated surface	Al or Cu
Number of units	1
<b>Overall system positioning</b>	<b>(manual)</b>
X, pitch, yaw and roll positioning	Manually adjustable by survey to within 100 $\mu\text{m}$ .
X minimum motion range (to select 3 different pairs of dechirper)	+/- 25 mm
Beam Height	1.2 m
<b>Motorized Gap and height (in y direction)</b>	
Y gap range	1 to 20 mm
Y minimum step for alignment (when going in one direction)	< 10 $\mu\text{m}$
Height moving range	+/- 2 mm
Y Encoder precision	1 $\mu\text{m}$
Speed in gap change	< 1 mm /s
Limit switches	yes
<b>Manually Selectable dechirper pair</b>	To test 3 different corrugations
Number of pairs	3
Motion range in X (not motorized but with tunnel access)	+/- 25 mm

Table 3.8.2.2: Variable gap (or slit) dechirper.

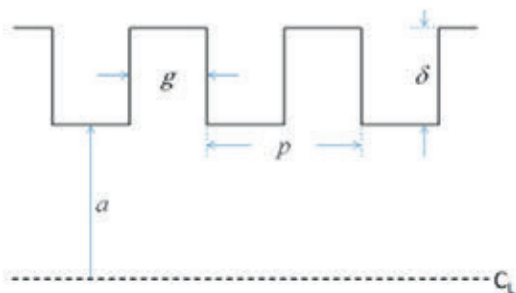


Fig. 3.8.2.2: Generic profile of the corrugated structure (parameters are given in Table 3.8.2.3).

Fixed square section parameters	
dechirper length	2 m
Dechirper width to get a square of 2.5 mm side	2.5 mm
Flatness over 2 m	50 $\mu\text{m}$
Material for corrugated surface	Al or Cu
Number of units	3
g (see Fig. 3.1)	250 $\mu\text{m}$
p	500 $\mu\text{m}$
delta	500 $\mu\text{m}$
a	1.25 mm
rounding	R <sub>tip</sub> < 25 $\mu\text{m}$
Tolerance in g, p, delta	+/- 13 $\mu\text{m}$ for p (critical) +/- 25 $\mu\text{m}$ for g (less important) +/- 25 $\mu\text{m}$ for delta

Table 3.8.2.3: Corrugation parameters for the dechirper corrugation.

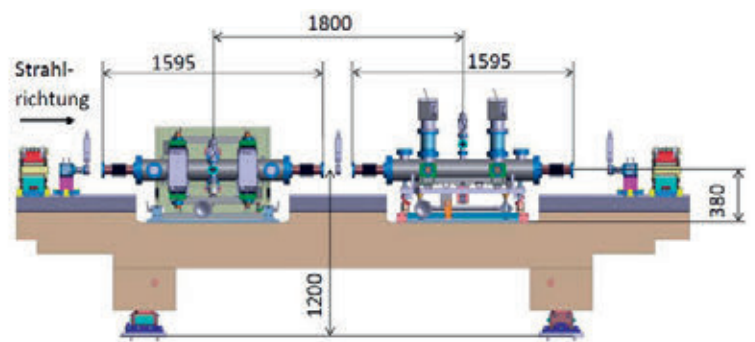


Fig. 3.8.2.3: Preliminary design of the two variable gap/slit dechirper on their girder.

### 3.9 Control system

#### Purpose

The control system presents a central part of all large facilities. Its main task is to integrate the distributed subsystems of the facility into one coherent infrastructure. The control system provides the connection between hardware and the operators, it creates the environment that allows physicists to carry out their measurements, and it archives data to allow retrospective comparison with simulations. Guidelines for the design of the control system are reliability, ease of use, and expandability. Beyond its pure functionality, the maintainability of the whole system and the portability for new developments in computer science are basic requirements. The maintainability of the control system can be optimized when there is an agreement on the use of standardized equipment. Exceptions can be allowed on individual basis only when the standardized equipment is not able to deliver the requested performance.

As Athos is an integral part of the SwissFEL facility it will inherit control system solutions used at SwissFEL (accelerator and Aramis beamline). The hardware and software platforms, boot and archive services, configuration management and logistics developed for SwissFEL will be used.

#### Reliability

A fault in the control system will most probably prohibit machine operation or experiments. Therefore, control system reliability should reach 98% of the machine's operation time (the number is a little lower than the achievements of the SLS control system, to take the challenges of the FEL into account). This implies similar reliability for most subsystems, such as file servers, databases, etc. A system can only be stable and reliable as long as malicious mischief (e.g. software viruses) is prevented. Therefore, the firewall infrastructure will provide access control to the machine and the experiment networks.

#### 3.9.1 EPICS environment

The control system will use the EPICS (Experimental Physics and Industrial Control System) toolkit. EPICS has already been successfully applied in other PSI large facilities as well as in several similar large projects around the world (e.g.

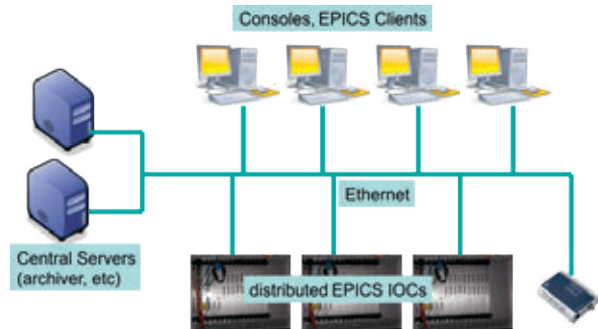


Figure 3.9.1: Control system architecture.

LCLS at SLAC or Diamond in UK). Due to its collaborative nature, using EPICS enables us to take advantage of work done at other laboratories. Using a standard software toolkit will allow us to make the best use of in-house know-how and to consolidate technical support services.

The basic structure of EPICS is a network-based client-server model implementing Channel Access (CA) as network protocol (3.9.1).

#### Server side

At PSI, the EPICS servers are mainly IOCs (Input Output Controller) that can run on various hardware platforms, such as VME boards, Linux PCs, or embedded systems. The IOC is configured at boot time by loading a set of configuration files, start-up scripts and drivers. The IOC may also run a sequencer process which implements a finite-state machine or customized programs. IOCs host EPICS channels or so called Process Variables whose values can be polled by EPICS clients by using CA network protocol.

#### Client side

EPICS client programs run mainly on the control room consoles and can be divided into three categories:

- System expert applications that enable experts to commission and maintain hardware systems
- Operator programs that provide control for routine machine operation
- Data acquisition programs that are used by scientists to perform and analyse experiments (on the accelerator or the experiment)

EPICS provides various interfaces to programming languages such as Java, Python, Matlab and others. To ensure maintainability of the programs and the interface itself, installation mechanisms and versioned updates will be provided by the controls section, in cooperation with the IT department.

While dealing with beam synchronous data, all of the client software relies on the common beam synchronous data acquisition system of SwissFEL. Live data can be subscribed from the so called Dispatching Layer as well as past data can be retrieved from the DataBuffer, a short term buffering and long term archiving system.

Certified beam synchronous analysis code, i.e. one that proves to be capable of dealing with the incoming data rate in a robust manner, can be deployed and enabled in an online analysis cluster. Results from this code can also be subscribed and retrieved in a synchronised fashion from the dispatching layer.

Non-certified analysis code will be executed on other (user) machines.

### EPICS access control

By using Channel Access Gateway (CAGW) application one can control the access to EPICS servers (IOCs) from EPICS clients in a different network (e.g. machine and experiments). Currently at SwissFEL CAGWs are not used; however, in case of need, they will be implemented in order to limit/control the access to machine control channels from the experiment network.

### 3.9.2 Network infrastructure

The design basics for the network infrastructure of Athos are based on the network Infrastructure design for SwissFEL. The SwissFEL network is a class B but segmented by using Variable Length Subnet Masks (VLSM) into C-like subnets. We have subnets divided according the SwissFEL building topology and functionality:

- Injector 1
- Injector 2
- Linac1-1
- Linac2-1
- Linac3-1
- Undulator hall

- Experiment hall-1 (Aramis)
- Virtual services/host for controls IT infrastructure
- CW timing & synchronization

Thus, for Athos additional C-like subnets will be setup. This system will be flexible and extensible, to meet new requirements from scientists or to adapt to new technologies.

### 3.9.3 Software maintenance and distribution

Software development is not finished once a program works, but has to be maintained and looked after to provide reliable service. Therefore, the control system not only has to include a development environment that allows easy design and distribution of software, but maintenance and upgrade as well.

Again, as Athos is an integral part of SwissFEL, same processes for software maintenance and distribution will be used.

All control system software as well as IOC configurations needed for machine and experiment operation will be stored and maintained using a versioning system (GIT), in order to ensure accessibility and flexibility. Part of the controls software (IOC configurations and EPICS drivers) will be distributed using existing in-house developed tools, which are already used in other facilities at PSI. The IOC configuration and installation tools are based on data stored in the relational database containing all the information about the control system hardware and software [48]. The IOC configuration files and the necessary drivers are deployed to a central location (NFS File Server), from where the IOCs load them during boot time. On the other hand, scripts and client application configuration files (i.e. launcher, alarm handler, caQtDM GUIs) will be distributed taking advantage of existing GIT versioning system features (e.g. web hooks, deploy keys).

General guidelines and support will be provided to make it easy for scientists and operators to use these tools to include their programs into the control system structure [49].

### 3.9.4 Controls infrastructure and subsystems

It is foreseen that the same Controls infrastructure (HW and SW solutions) as for the SwissFEL will also be used in Athos. If case new hardware or specific software is requested or

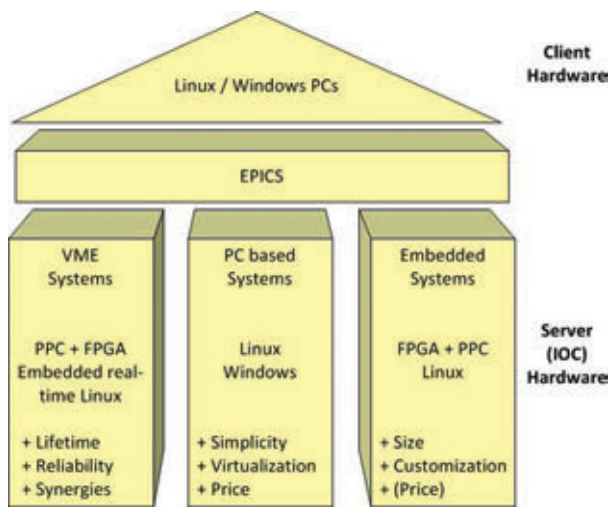


Figure 3.9.2: The three pillars of the SwissFEL/Athos control system.

desired, development time and the cost for integration into EPICS (for example, for driver development in case of a new HW) has to be taken into account and planned beforehand. For network components, file servers and PCs, SwissFEL will use hardware based on PSI standards defined by the central IT department. The IT infrastructure supporting the control system IOCs and other software is based on experiences gathered at already running facilities at PSI. Main services (boot servers, softioc hosts, etc.) are running on virtualization and the system administration is automated by a configuration management tool.

EPICS IOC's will be the base for standard hardware control, such as analogue and digital signals and motor control (see Figure 3.9.2).

Special requirements that cannot be met with either VME nor with PC based systems are fulfilled by using embedded

controllers (for example, FPGA-based systems or microcontrollers). Examples of such systems include geographically isolated devices or new hardware components which are not yet supported by any PSI standard hardware (e.g. DeltaTau Power Brick motion controller). However, the embedded controllers are and will be integrated into the EPICS framework as well as in the software maintenance and distribution processes.

More details on specific Controls subsystems are presented in following sub-sections.

### 3.9.4.1 Timing

Timing system provides the synchronization of all time-dependent subsystems with the electron bunch. Athos will be integrated into the SwissFEL timing system infrastructure. Timing and Event (from here on T&E) system of the SwissFEL has the following major responsibilities:

- provide precise triggering required by various subsystems of the machine as well as experiments
- distribute operation-critical parameters synchronously to various subsystems
- assist beam synchronized data acquisition

T&E system is not responsible for femtosecond level synchronization (this is provided by another system). All above mentioned functions, especially 2 and 3, require well defined interface and tight interoperation with the control system. SwissFEL T&E system is based on the Micro Research Finland

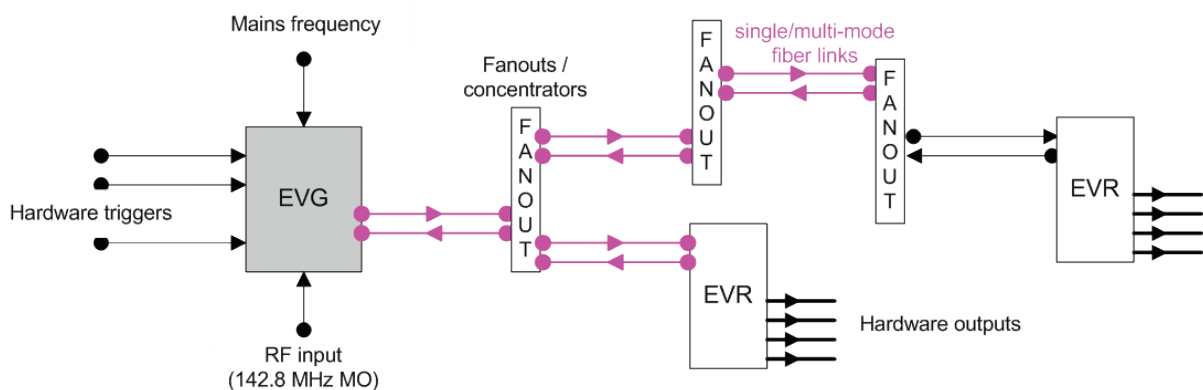


Figure 3.9.3: Timing and Event System Block Diagram.

(MRF) timing hardware which has been well accepted in accelerator community since several years (APS, Diamond, cells, super KEKB, LANSCE, Spring8, etc.). The same hardware has been adopted, for example, by some FEL facilities such as LCLS. T&E is a distributed master-slave system. It is comprised of one central system, the master, and many slave systems which are connected to the master in a star topology with optical links. The master gathers, generate and transmits all timing information. A slave is any system that receives timing information. The overall system architecture is illustrated in Figure 3.9.3.

There are two key components in the T&E system: EVG and EVR. The Event Generator (EVG) generates and distributes the timing information to slave systems. Slaves are equipped with one or more Event Receivers (EVR) which decode and react in both hardware and/or software wise on the received timing information. Fan-out units are 1-to-N receive-and-forward distributors (max N=12) which receive from upstream (EVG side) and distribute to downstream (EVR side). The major information flow is downstream (EVG to EVRs).

The master T&E system is a VME-based IOC that contains the EVG and the first level of fan-out distribution. The EVG synchronizes itself with the master oscillator (MO) of the machine by getting the 142.8 MHz reference clock. All the hardware logic inside the EVG runs with this clock.

The T&E system also provides some limited assistance to MPS (Machine Protection System) upon request of MPS responsables. It has to be noted however that the T&E system cannot guarantee machine protection as it can be prone to failure for example due to bad configuration of timing components or partial failure of the system.

Detailed information on Timing system Infrastructure for SwissFEL can be found in [50] and [51].

#### 3.9.4.2 VME IOC systems

In Athos, VME based IOC systems will be using a VME form factor IFC\_1210 carrier board which was developed together with industrial company IOxOS and is built around the industry standard PCI Express (and [52]). The FPGA is attached to the PCI infrastructure and it connects to the VME bus and two FMC interface slots which provide fast I/O functionality. A dual-core PPC CPU is included on the board, which runs a Linux operating system and on top of it runs the control

system software EPICS. The IFC\_1210 carrier board provides capabilities of fast front-end processing, data transport and industry-standard interfaces in already existing VME infrastructure. A VME crate monitoring tool will also be provided as a standalone EPICS IOC running on the CPU board.

#### 3.9.4.3 I/O signals

I/O signals to/from hardware equipment can be integrated into the control system either via the VME IOC systems (fast I/O) or by using the modular WAGO system [53], controlled from a soft-ioc that runs on a Linux console and uses MODBUS communication protocol to communicate with the HW(slow I/O). High frequency (GHz region) ADCs are integrated via dedicated systems running EPICS IOCs and using a PCI Express industry standard. High Reliability fast I/O signals will be interfaced with the use of PLCs, which will be integrated into the control system via EPICS soft-IOCs running on a linux console.

#### 3.9.4.4 Motion systems

For SwissFEL, thus as well for Athos, three basic types of motion systems are foreseen: Multi-axes systems, single axis systems and motion systems using piezo positioners (Figure3.9.4) [54]. Multi-axes systems can be further divided into conventional lower-performance motion systems and into high performance systems, that require complex or synchronous motion and might have to be synchronized with the arrival of bunches.

Depending on the motion system type and requirements, following motion controllers are provided:

##### **DeltaTau PowerBrick motion controller**

High performance 8 channel motor controller with support for incremental and absolute encoders used for control of 2-Phase or 3-Phase stepping motors as well as servo motors in case they would be needed for a specific system. DeltaTau PowerBrick motor controller is provided with a real-time multitasking operating system which supports coordinated motion and kinematic algorithms. And embedded Linux OS is running on the CPU and on top of it runs the EPICS control system with the IOC. It provides also built-in digital and analog I/O as well as the interface to the SwissFEL timing and event system via the PCI express slot (for the EVR).

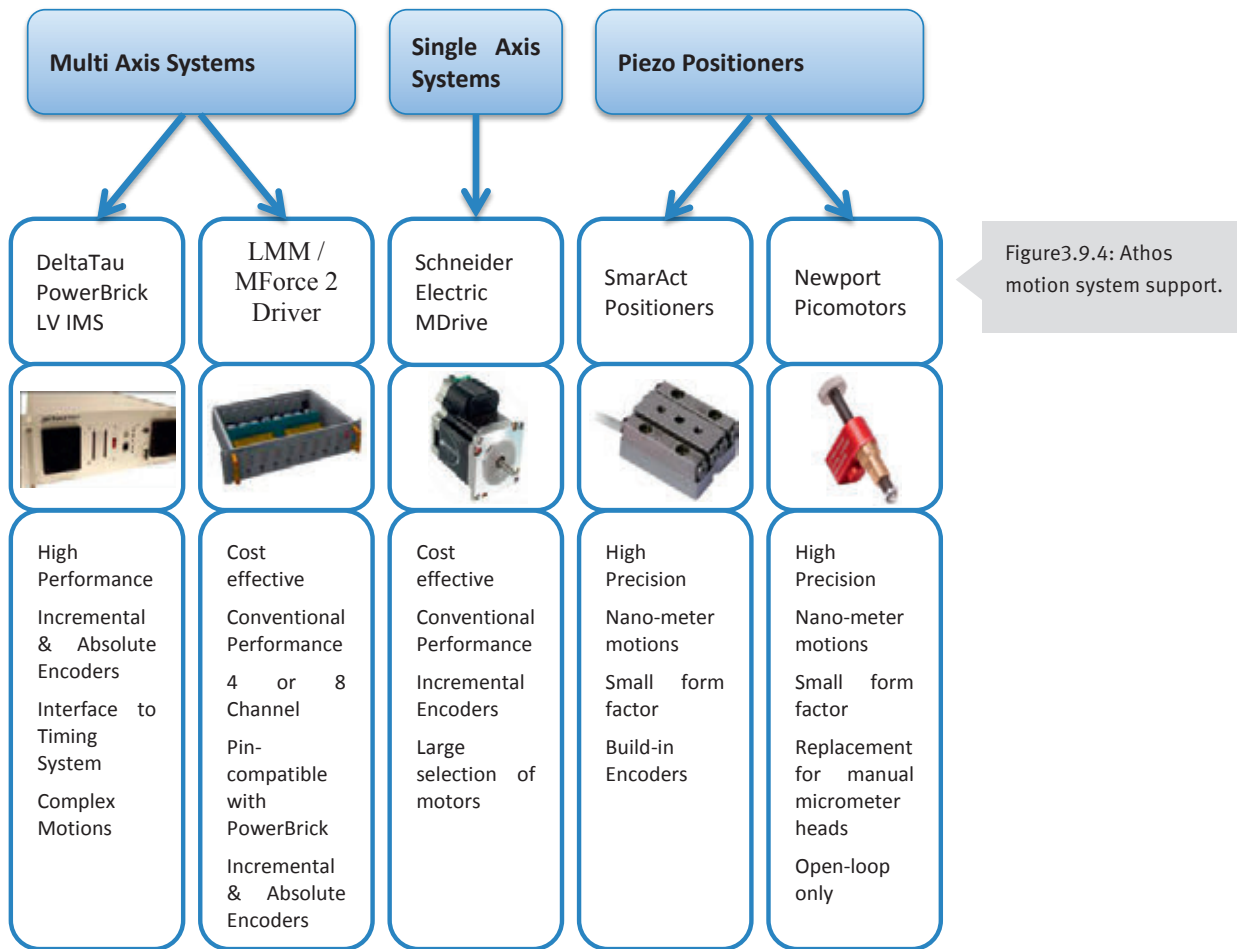


Figure 3.9.4: Athos motion system support.

DeltaTau motion controller will be used for all motion systems that require absolute encoders, coordinated motion and/or synchronization of movement or encoder readout with the bunch arrival time.

#### LMM/MForce 2 Driver

The SwissFEL 1602 LMM/MForce 2 Driver is based on the Schneider Electric MForce and LMM Driver Module which is software compatible with the Schneider MDrive Motor and is pin compatible with the DeltaTau Power Brick controller. It provides the option for 4 or 8 axis control, however in comparison with DeltaTau controller it does not provide the support for coordinated motion and interface to the timing system. It is controlled via the EPICS soft-IOC running on the terminal server (Moxa) which runs an embedded Linux OS.

#### Schneider Electric MDrive

Schneider Electric MDrive is a single-axis all in one controller used for a simple motion. The 1601 MDrive Interface Module is designed to simplify the connection to a Schneider Electric Mdrive Stepper Motor. It can be controlled via the EPICS soft-IOC running on the terminal server (Moxa) which runs an embedded Linux OS or in case an additional in-house developed interface is used, also from the EPICS soft-IOC running on the linux console.

#### Control of Piezo positioners

Piezo positioners are used for high precision nano-meter motions. Two standard types of piezo positioners are supported at SwissFEL/Athos, namely SmarAct positioners and Newport picomotors.

SmarAct positioners are controlled through the SmarAct Modular Control System (MCS) integrated into the EPICS control system through a serial interface.

Newport Picomotors are integrated into the EPICs control system via serial interface.

#### 3.9.4.5 Cameras

Controls will deliver a standard support for various camera types used in SwissFEL (Athos). Cameras from two suppliers, namely Basler and PCO will be supported. The EPICS IOC will run on a Windows-based server system (HP DL380 G[n]), hosting also a PCIE-EVR-300DC card, connecting the camera server to the SwissFEL Timing & Event system. All camera servers will be installed in dedicated water-cooled racks. The camera server is connected to the camera with one fiber and two Ethernet connections (one for camera data transfer and one for the timing/trigger signal) – See also Figure 3.9.4 [55]. The data will be transferred from the camera server to the data storage server (located in the remote data storage room) streaming out a ZeroMQ stream of data.

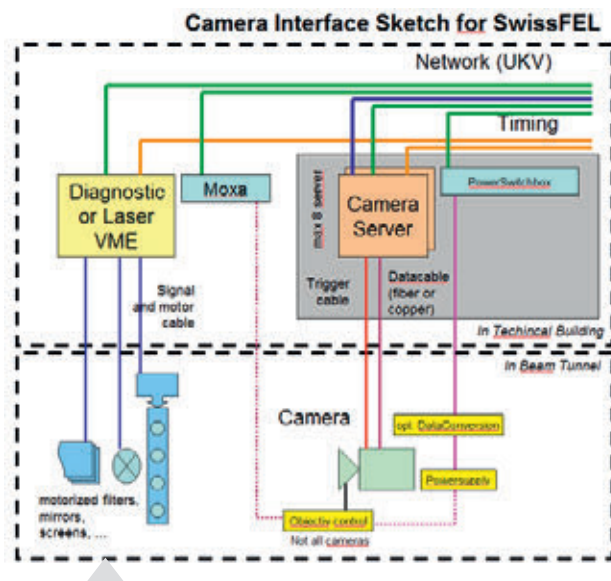


Figure 3.9.5: Camera interface for SwissFEL.

term archiving capability of selected buffered data. It enables also a subscription of live data in case they are needed for on-line real time analysis. DataBuffer depends on the bsRead software which provides synchronized and fast Epics IOC based readout functionality for the SwissFEL data acquisition system. The readout of requested channels from IOCs is triggered by a timing system provided event. Data are streamed out via ZeroMQ.

Archiver appliance provides the archiving ability for configured channels using three different engines: Short-term, medium-term and long-term archiver.

Depending on the number of EPICS channels added to the archiving systems, the systems might have to be scaled hardware wise. For both tools a data keeping policy will have to be agreed upon based on user needs, but also on financial and management aspects.

### 3.9.4.6 Data Archiving

The current SwissFEL beam synchronous data acquisition and archiving systems will be used also for Athos. Beam synchronous data (EPICS channels) will be archived with the use of the DataBuffer tool, while beam non-synchronous data will be archived using the Archiver Appliance (Figure 3.9.63.9.6).

The DataBuffer tool provides a short term buffering capability of requested beam synchronous data and later a long

### 3.9.4.7 Other Interfaces

Other systems such as Vacuum, Cooling, Dose Rate Protection System (DRPS) or GLS are also integrated into the control system. They are interfaced via EPICS IOCs running on Linux consoles. Often systems that require highly reliable, real-time I/O signals (such as vacuum interlocks, DRPS, Cooling) connect to Programmable Logic Controllers (PLC), which are then interfaced to the EPICS control system. Other systems or devices are integrated through serial interfaces.

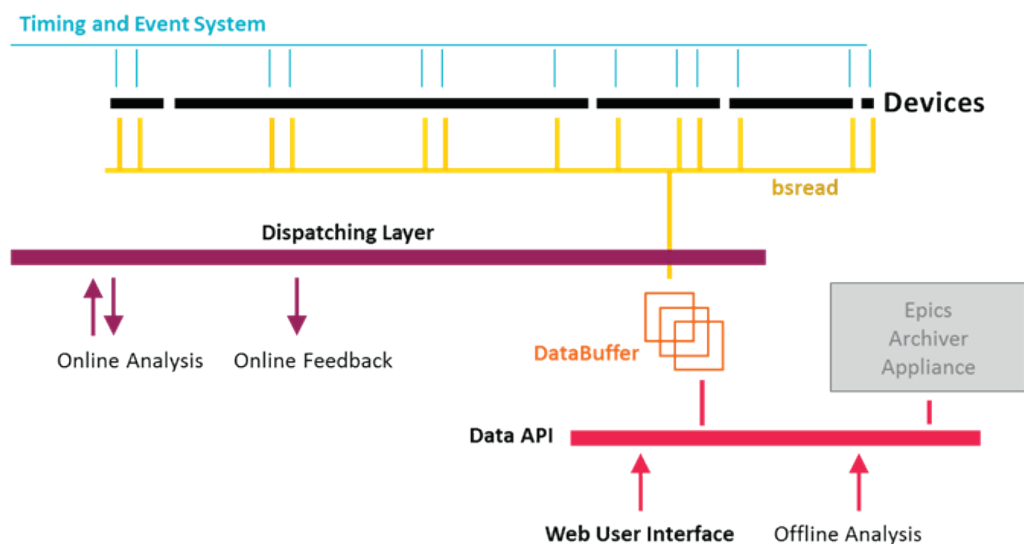


Figure 3.9.6: SwissFEL Data archiving system.

# 4 Photon beam components

This chapter describes the main components situated downstream from the main beam dump dipole magnet of the Athos lines. The photon transport can be split into the following main areas:

- the Front End
- the photon switch-yard (in the Athos Optical Hutch)
- the Athos Experimental Hall

The purposes of the Front End are to diagnose (arrival time, position, intensity, spectrum) and control (attenuate, collimate) the photon beam. The photon switchyard is used to distribute the photon pulses towards one of the three possible experimental stations. Only two experimental stations are foreseen at the startup of Athos. The Front End is located in the main tunnel and is separated from the Optical Hutch by a 2 m thick shielding wall.

## 4.1 Front End Layout

The Front End layout for Athos is given in Figures 4.1.1. The Front End starts after the beam dump dipole magnet ( $z=499\text{m}$ ) and extends up to the beam profile monitor situated just after the front end shielding wall. The Photon Switch-yard (from the 1<sup>st</sup> mirror to the photon beam stopper) is located in a room separated from the main tunnel, downstream the Front End shielding wall to allow maintenance access during machine operation of Aramis.

The Front-End will use the same or similar components as used in the ARAMIS Front-End. The first upstream component is the fixed collimator, followed by a photon shutter and an adjustable aperture, i.e. an x-ray double slit system which is adjustable from an aperture of  $3 \times 30$  mm to completely closed. The role of those components is to restrict the angular acceptance on the beamline to the angular distribution of the FEL radiation and limit the effect of spontaneous radiation. In normal operation, the opening of the x-ray double slits will be set to 4-6 sigma of the FEL central cone. Each jaw of the x-ray double slits is covered by a 10 mm thick B4C plate bonded onto a 50 mm tungsten alloy block. The B4C, a low atomic number and high melting temperature material, has been identified as a good candidate to absorb the FEL radiation without beam damage.

The photon shutter is a simplified version of the Aramis photon Beam Stopper, whereas it uses only the first actuator with the B4C structure. This photon shutter is not a safety device, rather it is used to block the beam when changing the mode of the beamline or when moving devices in and out of the beam which cannot take the full beam during transition.

The first photon diagnostics element in the front end is the gas beam intensity and position monitor developed and produced by DESY [56] followed by a solid position monitor developed by SACLA [57]. A gas attenuator in combination with a solid attenuator with a set of thin diamond and silicon films of various thicknesses is used to adjust the beam pulse fluence. The gas attenuator has an attenuation length of around 50cm which can be filled with various gases at different pressures to achieve an attenuation from 0 to 100% for low photon energies. At higher energies the solid state attenuator will be used. The attenuator is followed by a Diode intensity monitor. This has been proven to be very helpful during commissioning of the ARAMIS undulators and will thus be included in ATHOS. A beam profile monitor before the single shot spectrometer is needed for diagnostics.

The single shot spectrometer cannot be the same used at ARAMIS as its lowest photon energy threshold is around 4keV. Thus the single shot spectrometer will be based on a hemispherical analyzer.

The last item inside the tunnel is the beam stopper, which controls the radiation exiting the tunnel, followed by a collimator which limits the angular distribution of this radiation. Finally, the front-end section ends with a beam profile monitor located just behind the tunnel shielding wall in the optics hutch.

## 4.2 Photon Beam Diagnostics

The Athos beamlines will have shot-to-shot on-line photon diagnostics available to help the users better understand the data they are gathering, and to help the machine operators to continuously improve the photon beam quality and parameters during an experiment. A summary of the diagnostics to be used is listed in table 4.2.1 below.

Fig. 4.1.1: Layout of the Athos Front End ( $z < 539\text{m}$ ) and optical hutch ( $539 < z < 604\text{m}$ ).

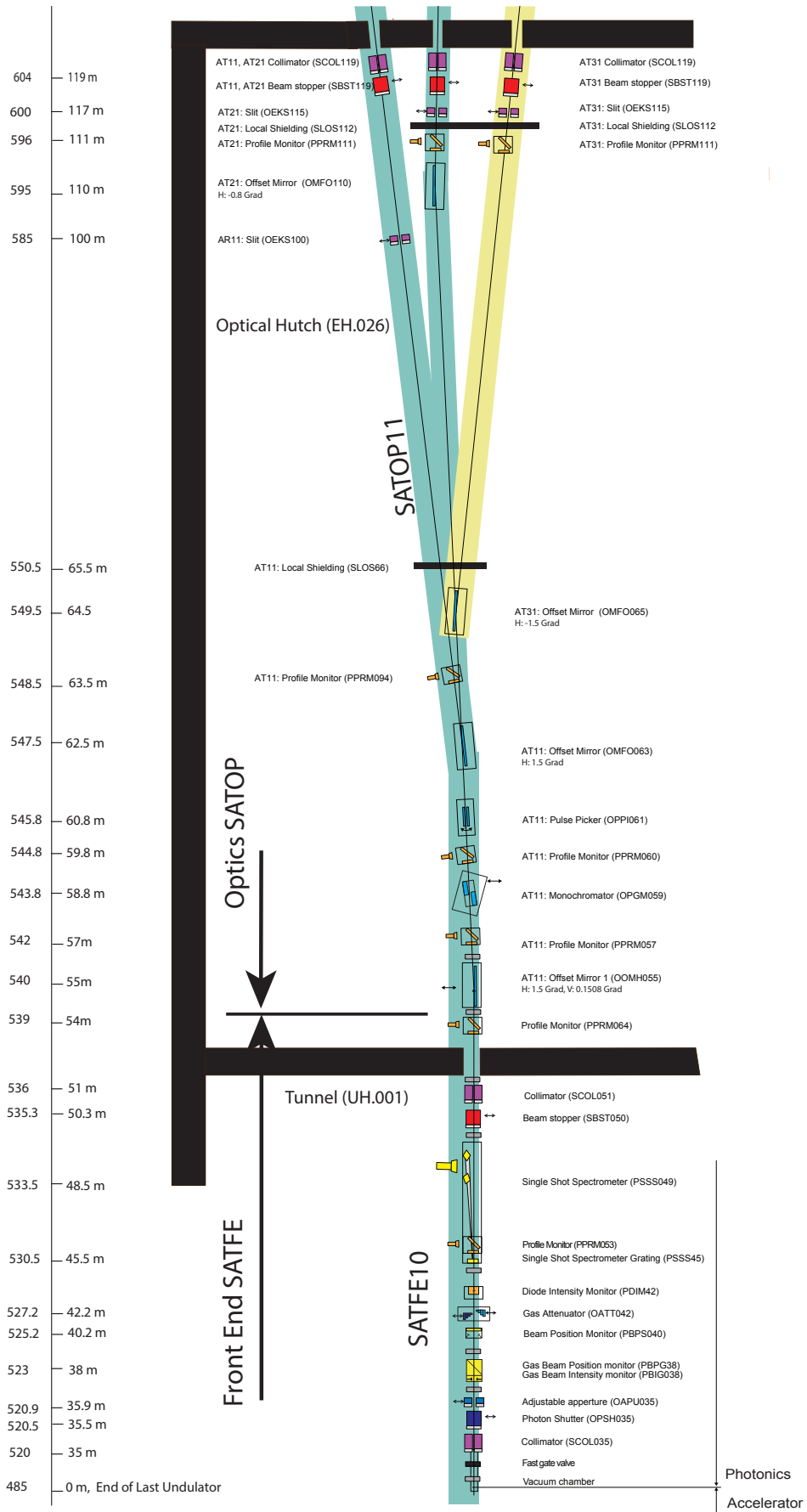
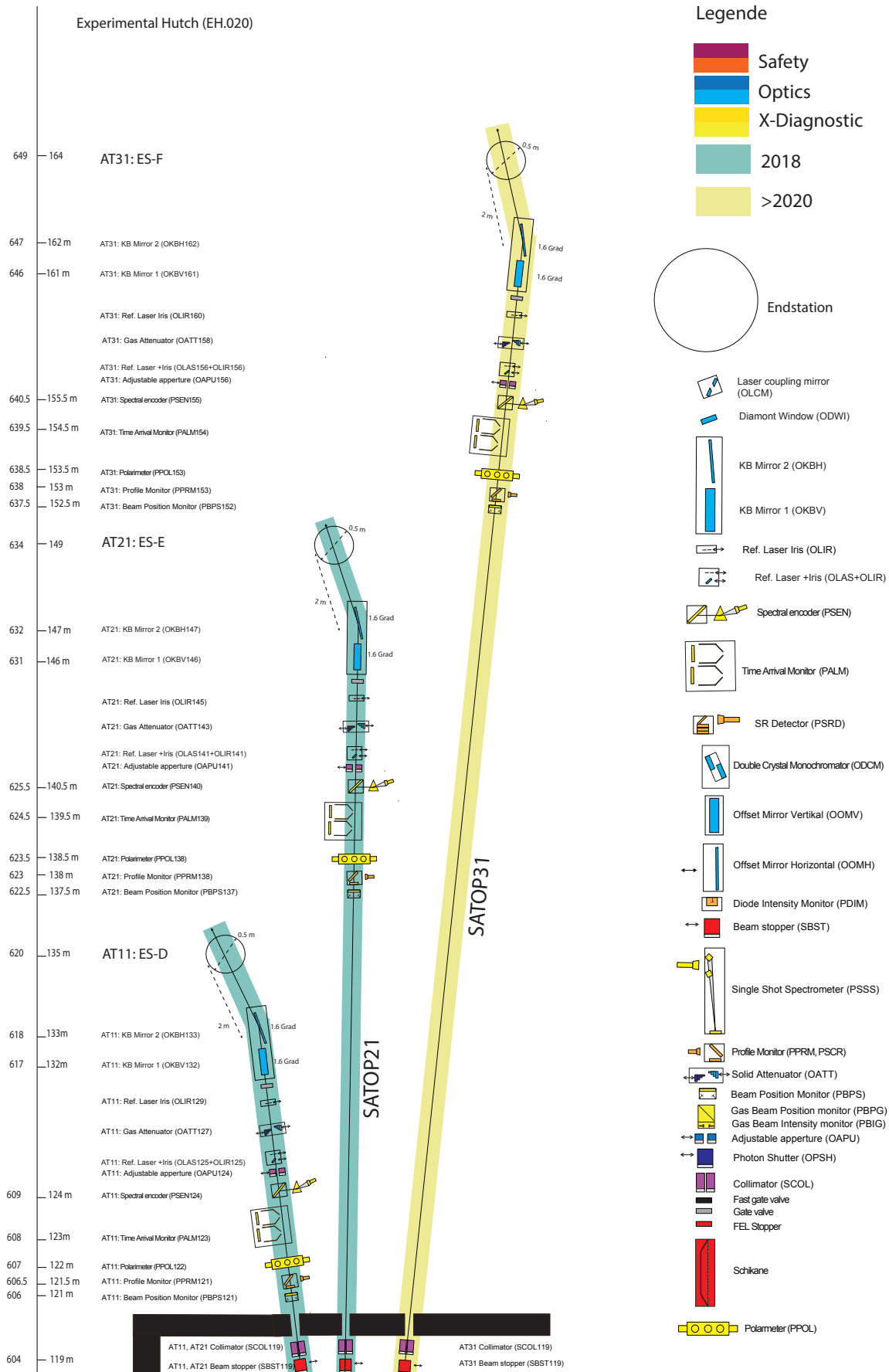


Fig. 4.1.2: Layout of the Athos Experimental Hall with legend (z > 604m).



Most of the diagnostics tools to be used at Athos are gas-based, to ensure they do not disturb the beam and fulfill the requirement for non-destructive measurement. They are discussed below.

**Gas position and intensity monitor:**

This device will be a variation of the already existing Photon Beam Intensity (Gas) and Photon Beam Position (Gas) (PBIG/PBPG) monitor used at Aramis and tested at various FELs around the world [58] [59]. It will be a pair of ionization chambers with split electrodes to detect both the intensity of the photon pulses ionizing the gas in the chamber, and measuring the vertical or horizontal position of the beam by comparing the signals on the two halves of the split electrodes. The device will be adapted for lower photon energies, which will make it significantly shorter and easier to use due to the larger atomic ionization cross sections at the photon energies expected at Athos.

**Ce:Yag Screens:**

These screens will be copied from the existing PPRM design for Aramis and installed in Athos. They are equally able to work at lower and higher photon energies, and can cover a range of 5x5 mm for observation of beam position and beam shape. If the beam parameters require a larger area for observation, the optics and the design can be adapted to match the new conditions.

**Online Spectrometer:**

The soft x-ray energies that will be used at Athos require a different concept than the Photon single-shot spectrometer (PSSS) used for the harder energies at Aramis. The only way to measure the photon energy non-destructively over the whole 200-2000 eV energy range of Athos is through the use of a gas-based detector. To this end, the new online spectrometer for Athos will be based on a hemispherical analyzer that will observe the photoionization spectra of various valence shell or outer sub-shells of inner shell electrons. Though the device is still in the development stage, the theoretical calculation show that it will work with an expected resolution of around 200 meV and intensity profile accuracy of 10% over the whole photon energy range of Athos. If the intensity profile accuracy condition is relaxed, the resolution could be improved to be as good as 40-50 meV. The spectrometer would be able to look at the whole bandwidth of the FEL with this accuracy on a shot-to-shot basis.

**Beam Polarization Monitor:**

An online polarization monitor has been developed at DESY by Jens Viefhaus and his group, and already tested at FERMI [60] with crossed-polarized undulators. The monitor, also known as the cookiebox, uses 1 electron time of flight spectrometers (eTOFs) placed in a circle around the photoionization region to read the angular photoelectron distribution perpendicular to the propagation direction of the FEL beam.

Device	Task	Operational parameters
Gas position and intensity monitor	Non-destructive intensity and position monitor	10 μm positional resolution, <10% absolute intensity measurement, 1% relative intensity measurement
Ce:Yag screens	Destructive position and beam profile monitors	10 μm position resolution, signal resolution of 8 bits or better.
Online spectrometer	Non-destructive measurement of the photon pulse spectra.	About 200 meV resolution over the bandwidth of the FEL.
Beam polarization monitor	Non-destructive measurement of the polarization of the FEL beam.	Measures the non-circular polarization of the FEL beam to an accuracy of about 10 degrees.
Photon pulse length and arrival time monitor	Non-destructive monitor of the FEL arrival time vs. the experimental laser, and pulse length monitor	10 fs RMS or better arrival time and 10 fs RMS or better pulse length resolution.

Table 4.2.1: Diagnostics foreseen for Athos at SwissFEL.

The distribution is described by equation (1)

$$\frac{d\sigma(h\nu)}{d\Omega} = \frac{\sigma(h\nu)}{4\pi} \left[ 1 + \frac{\beta}{2} (3\cos^2\theta - 1) \right] \quad (1)$$

where  $\sigma(h\nu)$  is the photon-energy dependent atomic cross-section,  $\theta$  is the angle of the emitted photoelectrons in the plane perpendicular to the motion of the photon beam, and relative to the polarization of the ionizing photon.  $\beta$  is an experimentally determined parameter, measured for most electron shells, and varies between  $-1$  and  $2$ . As an example, all s-shell electrons have a  $\beta$  parameter of  $2$ , creating angular photoelectron distributions like those shown in figure 4.2.2.

The device can measure the linear polarization of the FEL pulse to an accuracy of about 10% on a shot-to-shot basis.

**Photon Pulse Arrival and Length Monitor (PALM):**

This device, already tested at SACLA at hard x-ray energies [61] [62] and implemented as a standard diagnostics tool at Aramis, will be adapted to soft x-rays and used as an on-line diagnostics for Athos. The basic principle of the device is that it uses an electron time of flight spectrometer and an oscillating THz pulse that interacts with the electron at

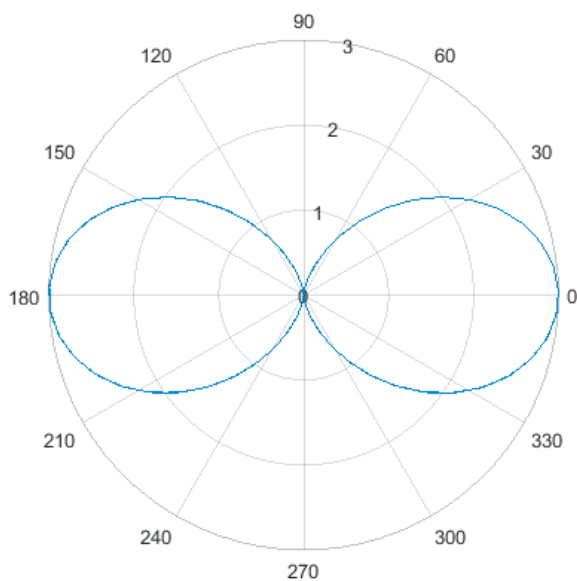


Figure 4.2.2: Angular distribution for s-electrons.

ionization to give it additional energy dependent on the strength of the THz pulse at that time. This allows for a map of time to the kinetic energy of the electron, which is measured by the eTOFs. These measurements are then used to both provide the arrival time of the FEL pulse relative to the experimental laser that generates the THz pulse, and the pulse length of the FEL beam.

### 4.3 Athos optical layout

#### 4.3.1 Introduction

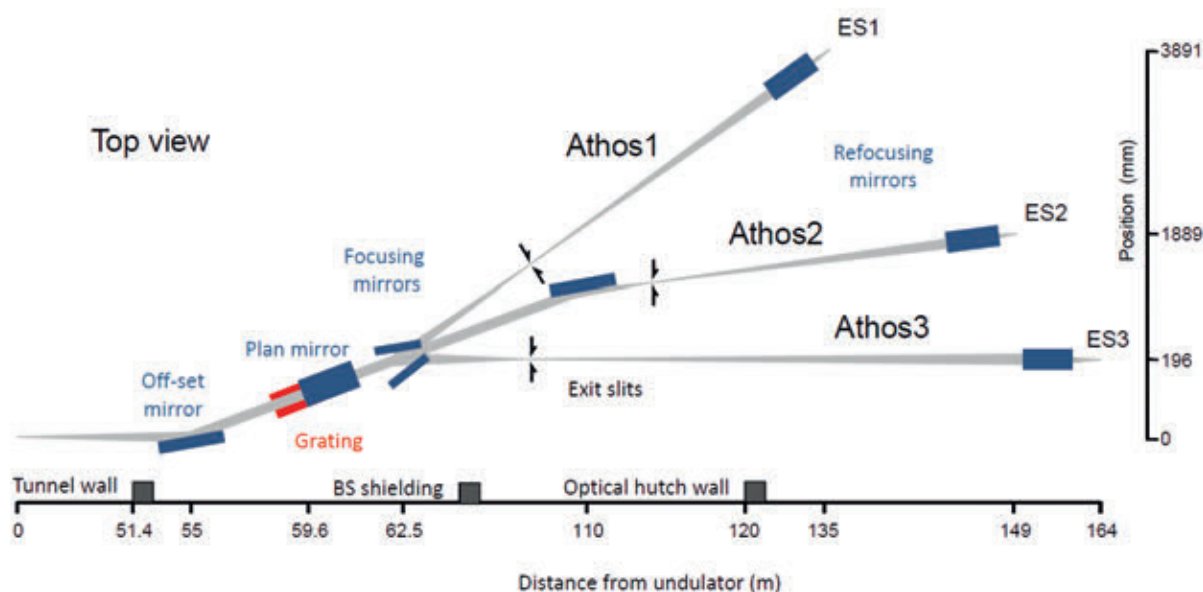
To cover the full wavelength range, the SwissFEL facility divides up into an undulator line Aramis for the hard X-ray regime and the undulator line Athos for the soft X-ray regime. Future upgrades with additional hard x-ray undulators lines are already foreseen in the layout of the buildings and will be realized at a later date. This report describes the beam transport system for the Athos undulator lines for photon energies from 170 eV – 2 keV.

The beam transport system has several intentions. While some of them are mandatory for all lines, others may be realized in particular branches only. From the optical point of view, the most important are:

1. the distribution of the beam to the various end stations.
2. the monochromatisation of the FEL-beam or the alternative use of the undispersed, pink beam in the same end station.
3. the formation of beam spots with variable size in the end stations.

The overall layout of the beam transport system is shown in Figure 4.3.1. To be compatible with the spatial requirements at other SR-facilities, especially the SLS, the height above the floor should be approximately 1400 mm at the location of the experiments. The beamline thus transports the beam from 1200 mm height at the exit of the undulator to the required 1400 mm at the the experimental stations. For maximum flexibility a collimated PGM design with variable deflection angle at the grating is chosen. The higher deflection angles at the optical elements allow for a splitting of the beamline branches after the grating chamber and still have a reasonable lateral space at the end.

Figure 4.3.1: Schematic layout of the Athos beamlines.



The incoming beam is separated from the Bremsstrahlung by a horizontally deflecting offset mirror and directed to a common monochromator vessel. A single grating chamber saves costs, reduces complexity but a failure affects all three endstations. The grating chamber consists of a plan grating-plan mirror combination in a SX-700 setup [63]. Contrary to the original design, the grating is placed in front of the plan mirror and deflects the beam upward whereas the mirror is mounted face down. The beam transport to a height of 1400 mm above floor is accomplished by operating the grating at a higher deflection angle as the subsequent plan mirror. Similar configurations have been successfully implemented in other beamlines in the past [65; 66]. An advantage of this configuration is a large deflection angle on the grating with enhanced diffraction efficiency and a small deflection angle on the plan mirror with higher reflectance. A drawback is the long mirror length of approximately 1000 mm, necessary to span the full energy range with two gratings of 50 l/mm and 200 l/mm line density, respectively. Whenever possible, the beam transport system should accept the whole FEL beam, i.e. five times the rms-value of the beam cross section. This may not be possible at all

photon energies and at all optical elements. But at least an acceptance of four sigma should be guaranteed. A smaller acceptance not only wastes pulse energy but also leads to interference effects at the apertures, resulting in an inhomogeneous intensity distribution on the sample. This becomes a major drawback, especially when nonlinear processes are studied. Besides the mirror surface quality, the mirror lengths and deflection angles are therefore of crucial importance for the optical design. Particular attention is paid to the choice of mirror coating materials to increase the acceptance of the mirror systems.

#### 4.3.2 Incident photon beam characteristics

The Athos line will use APPLE undulator with a period length of 38 mm operating with k-values between 1.0 and 3.8. This offers full polarization control.

GENESIS calculations performed by S. Reiche serve as basis for the layout of the beam transport system. The bunch charges are 200 pC and pulse length approx. 29 fs (rms). The source size and divergence are proportional to the wavelength and a linear regression is plotted in Figure 4.3.2. The regression gave:

Photon Energy (eV)	180	310	620	1240	1770
Source size* (μm)	58.2	50.2	39.5	37.7	36.0
Source divergence* (μrad)	28.6	19.0	10.6	5.3	3.9
Pulse energy (μJ)	590	890	700	580	410
Spectr. Bandw.* (%)	0.41	0.24	0.2	0.15	0.1
Beam size* in 55 m (μm)	1570	1050	580	290	220

Table 4.3.1: Beam parameters for the ATHOS undulator UE38 operating with 200 pC bunch charge.

\*rms-values

$$\sigma_r = 3.679 \mu\text{m} / \text{nm} * \lambda + 33.6 \mu\text{m} \quad (1)$$

$$\sigma'_r = -0.21513 \mu\text{rad} / \text{nm}^2 * \lambda^2 + 5.62678 \mu\text{rad} / \text{nm} * \lambda + 0.02822 \mu\text{rad} \quad (2)$$

From the source size  $\sigma$ , a diffraction limited divergence  $\sigma' = \lambda / (2\pi\sigma)$  is calculated and shown as dotted line in the right panel of Figure 4.3.2. This assumes a gaussian intensity distribution in the waist of the FEL-beam and sets the lower limit of beam divergence.

The values for beam size and fluence are plotted in Figure 4.3.3 for typical distances of the offset and the refocussing

mirror systems. Without pre focusing, the beam at the end of the Aramis 2 beamline extends to almost 5 mm width ( $5\sigma$ , 1.7 keV).

The values for source size ( $\sigma_r$ ) and divergence ( $\sigma'_r$ ) given in Table 4.3.1 denote the rms-values of the corresponding two-dimensional intensity distribution. The rms-values of the one-dimensional intensity distribution, when projected on the cross section, ( $\sigma_x$ ) and the divergence ( $\sigma'_x$ ) derived from that, are smaller. For a gaussian beam they are related by:

$$\sigma_x = \sigma_r / \sqrt{2} \quad (3)$$

$$\sigma'_x = \sigma'_r / \sqrt{2} \quad (4)$$

Figure 4.3.2: Rms-values for source size (left) and beam divergence (right) of the Athos-FEL-beam according to Table 4.3.1. A linear regression to the data is plotted in both diagrams. The dashed line in the right diagram shows the divergence of a gaussian beam with the same beam waist as the FEL-beam.

As the mirrors are always wide enough to accept the full beam in the direction perpendicular to the deflection plane, the mirror length is designed with the rms-values of the projected intensity distributions.

The projected rms-values are plotted as dashed lines in Figure 4.3.3

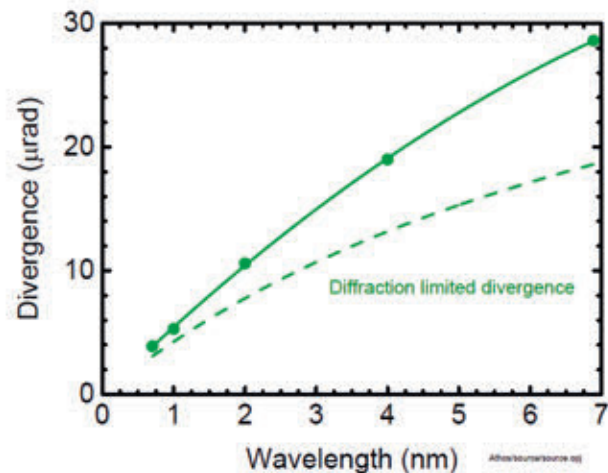
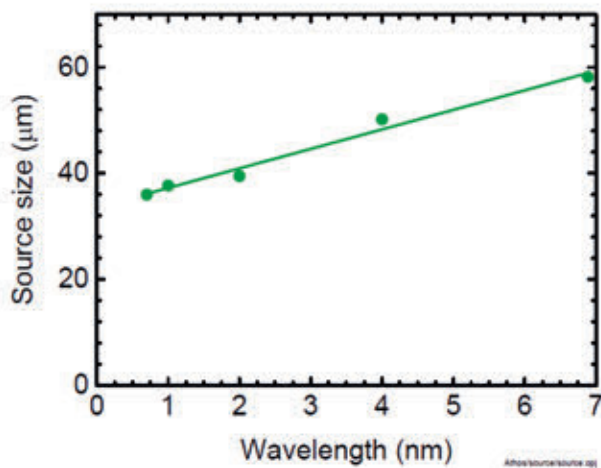


Figure 4.3.3: Left panel: Beam size at the offset mirrors (55 m) and the location of the refocusing mirrors of Athos 3 (160 m). Solid lines are fits to the values of Table 4.3.1, dashed lines represent the projected values according to eqn (4). The right panel shows the peak fluence at the two distances as function of the photon energy.

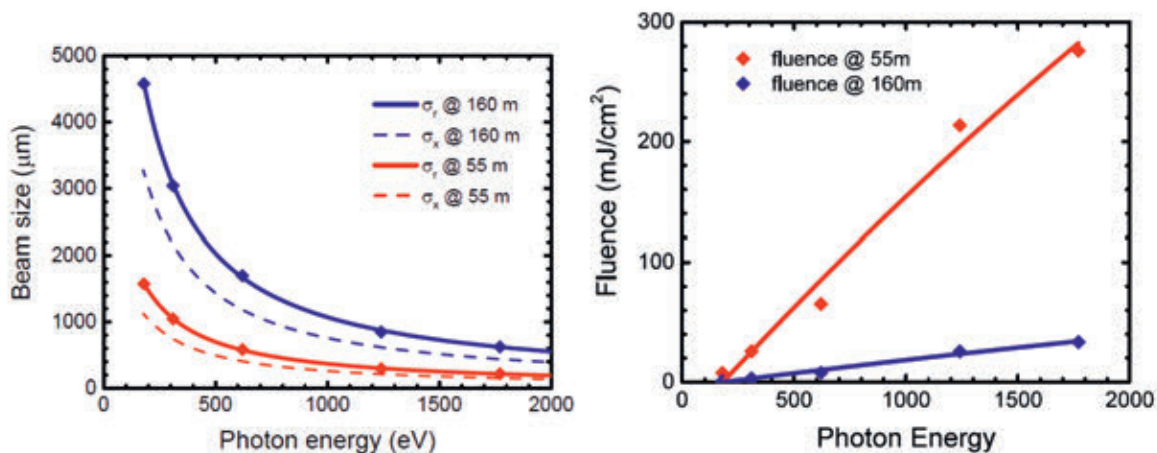
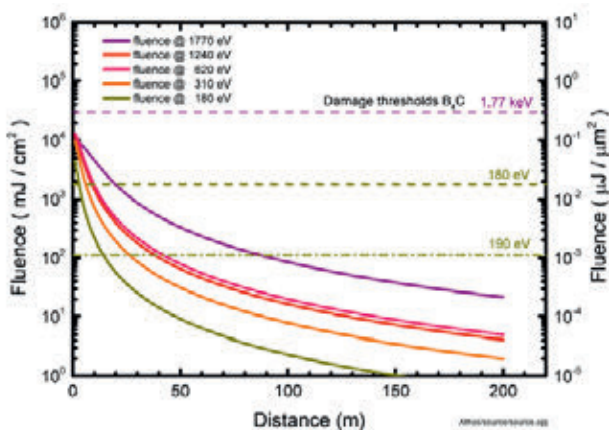


Figure 4.3.4: Fluence along the beamline.



### 4.3.3 Optical Beamlines

The optical layout of the Athos beamlines is shown in Figure 4.3.1. A more detailed view of the Athos-1 branch is shown in Figure 4.3.5.

The higher deflection angles at the optical elements allow for a splitting of the beamline branches after the grating

chamber and still have a reasonable lateral space at the end. A single grating chamber saves costs, reduces complexity but a failure affects all three endstations.

The changeover from monochromatized to pink beam operation is accomplished by a rotation of the first mirror and a translation of the second mirror out of the beam. By this the deflected beam follows the same beam path as in monochrome mode from the location of the second mirror.

The grating chamber consists of a plane grating / plane mirror combination in a SX-700 [63] setup. The beam transport to a height of 1400 mm above floor is accomplished by operating the grating at a different deflection angle as the mirror M2. This configuration has been successfully implemented in other beamlines in the past [65,66].

#### 4.3.3.1 Pink beam operation

The switching from monochromatic to pink beam could be accomplished by just setting the zero diffraction order at the grating. However this would require the plan premirror M2 and the grating to be in the beam. A solution with less optical elements in the beam can be realized by moving the grating out of the beam and rotating the first mirror to direct

the beam directly onto mirror M3. The defining condition for this is that the beam hits the center of the focusing mirror M3 with the same incidence angle. The difference is that in monochrome mode the beam impinges the mirror M2 from the grating, whereas in pink mode the beam comes directly from mirror M1 and mirror M2 is moved aside.

The main setup for the motion of mirror M1 is a roll-rotation with small corrections in pitch and yaw. This roll-motion of M1 is a well established procedure in dipole beamlines at synchrotrons to select linearly polarized light from the orbital plane or elliptically polarized light from above and below [64]. In monochrome operation the mirror deflects the beam horizontally by twice the incidence angle  $\theta$ . Switching to pink beam operation, a roll rotation of an angle  $\alpha$  inclines the reflected beam by an angle  $\varphi$  with respect to the horizontal plane. By this the beam arrives at the height of the subsequent grating but the deflecting angle projected to the horizontal plane is now different. This has to be compensated by a small rotation around the vertical axis by  $\Delta\theta$  bringing the beam back to the position of the grating center. After that, a yaw-rotation of the mirror orients the mirror with respect to the new deflection plane as set up by the incident and the reflected beam, respectively.

A fundamental issue of soft X-ray beamlines spanning a wide photon energy range is the coating of the optical elements. There are no materials available that offer a continuous high reflectance over the full ATHOS photon energy range. For FEL-beamlines, low-Z materials as diamond like carbon or  $B_4C$  are preferred materials to reduce the damage risk under high fluence values but both show pronounced absorption edges – and therefore high damage risk- at the carbon edge around 280 eV. However, in the last years mid Z-coatings as for example rhodium have been successfully commissioned under intense FEL-radiation and proved to be useful at least for higher photon energies [67]. A dedicated second coatings on the optical elements could be an option to access the problematic spectral range of  $B_4C$ .

#### 4.4 Experimental Hall

In contrast to the hard x-ray endstations of the Aramis beamline, the Athos experimental hall will not be divided into hutches by fixed walls (Fig. 4.4.1). Instead subdivision between the different soft x-ray endstations will be achieved by movable shields. This allows for maximum flexibility for

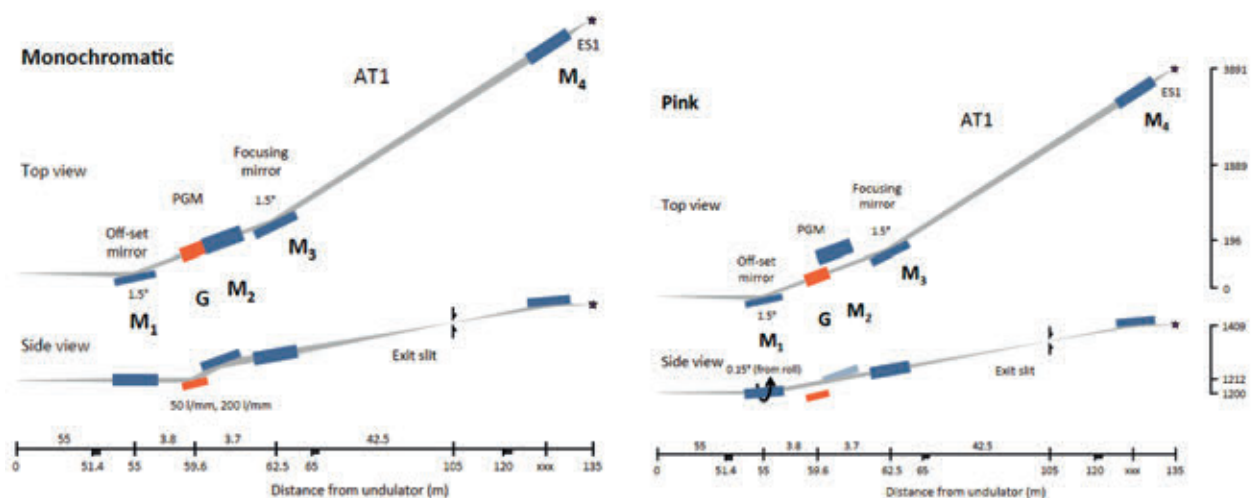


Figure 4.3.5: In monochromatic mode, the first mirror directs the beam horizontally to the plane mirror M2 (shown left). In pink mode, a roll motion of M1 steers the beam in a way that the fix point is hit.

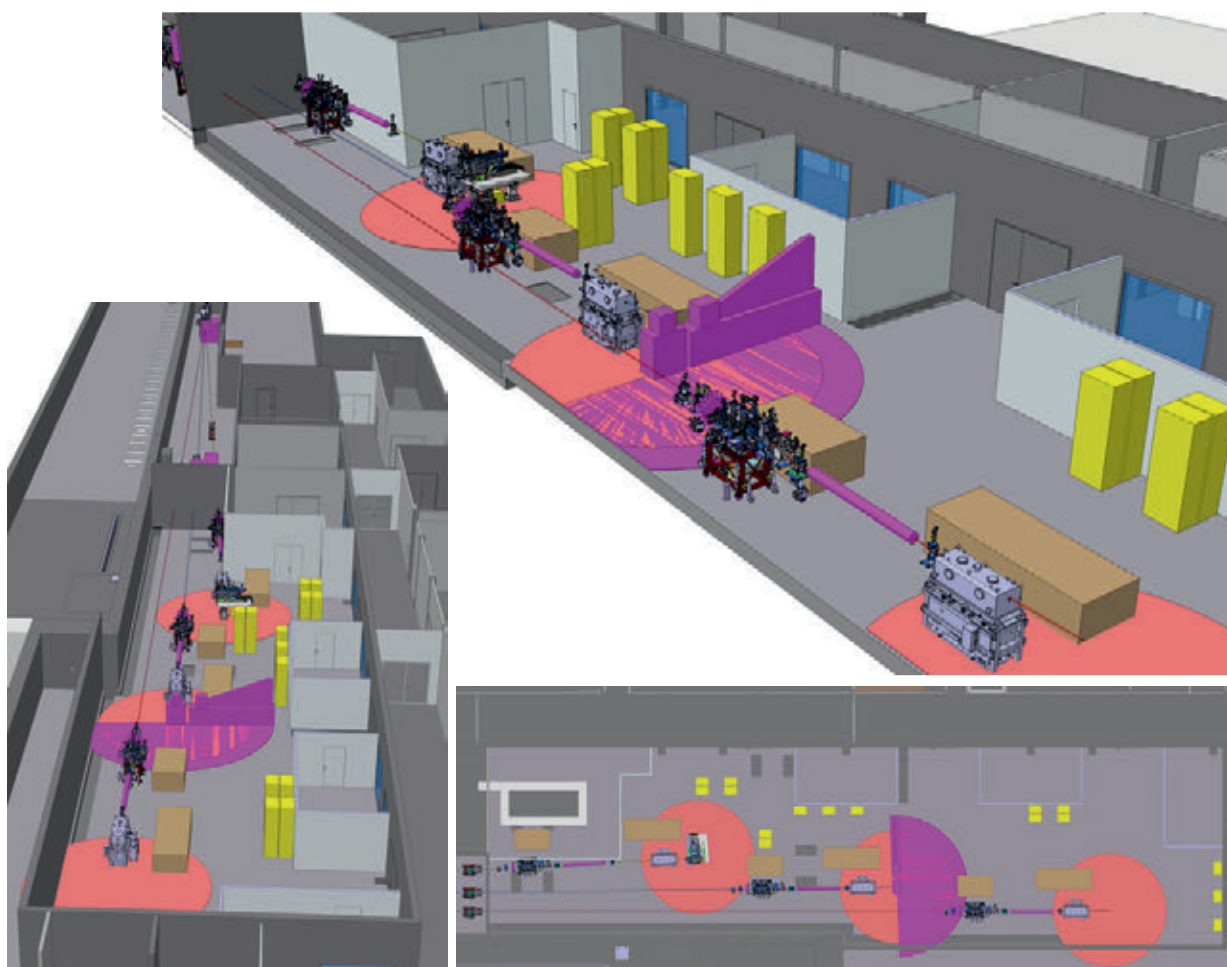


Fig. 4.4.1. Layout of the experimental hall of the Athos beamline, including schematics of the three Athos endstations.

user-supplied experimental station installation. In addition to the experimental stations the hall contains a laser room, which contains the experimental pump laser. This laser will be delivered to the experiment using vacuum transfer lines.

#### 4.4.1 Concepts for experimental endstations

It is foreseen to permanently install standard equipment of the experimental endstations in the Athos experimental hall, such as refocusing mirrors, photon diagnostics, pump lasers and control rooms. Details of the instrumentation are not yet defined, as the Athos beamline will come online in a second phase of the project (see Chapter 1). However, by avoiding the use of fixed internal separation walls will guarantee flexibility to accommodate both permanent instrumentation as well as roll-in-roll-out equipment provided by some of the prospective Athos users.

A first attempt towards concepts for experimental endstations was made at the three-day “Photonics Spring Workshop” in April 2017 [68], where the future user community

of Athos was consulted to discuss which breakthrough can be expected from the unique combination of the CHIC operation modes and the full x-ray polarization control. Moreover, the goal of the workshop was also to prioritise techniques and the required experimental endstations, which should be available when Athos becomes operational. The discussion included what requirements these instruments should have in terms of pump lasers, sample environment and detector capabilities.

Input from the prospective users was collected in “condensed matter physics” and “ultrafast chemistry and biology” break-out sessions. Generally, the numerous contributions have demonstrated that time-resolved resonant elastic and inelastic x-ray scattering, time-resolved absorp-

tion and fluorescence spectroscopy, as well as femtosecond studies of the dynamics of chemical reactions will have priority during the first phase of scientific endeavours at Athos.

#### 4.4.1.1 Condensed matter physics

Research of correlated electron systems and magnetism will tremendously benefit from the ultrabright x-ray pulses of the Athos beamline, as many relevant atomic absorption edges are found in the soft x-ray regime, in particular the so-called water window of C, N and O, the *L*-edges of 3d transition metals, the *M*-edges of rare-earth elements and also the Si *K*-edge (see Fig. 1.6.2).

The “condensed matter physics” break-out contributions can be grouped as follows:

- **Time-resolved resonant soft x-ray scattering** (7 contributions), including time-resolved resonant soft x-ray diffraction, time-domain Fourier transform spectroscopy [69] [70], time-resolved resonant inelastic x-ray scattering (trRIXS) [71], two-color, stimulated RIXS, as well as single-shot and imaging RIXS using Fresnel zone plates.
- **Single-shot x-ray magnetic circular dichroism** (trXMCD) and **x-ray absorption spectroscopy** (trXAS) using the large bandwidth mode (see Chapter 2.3.3.2) and a spectrometer to cover multiple absorption edges per x-ray shot (3 contributions).
- Plane-wave coherent diffractive imaging [72] (1 contribution).
- Time-resolved soft x-ray photoemission spectroscopy (1 contribution).
- **Non-linear x-ray / two-colour experiments** (2 contributions), including two-colors with different beam pointing, split-and-delay unit for transient gratings to imprint periodic potentials (e.g. on charge/spin ordered correlated materials), stimulated Raman scattering and four-wave-mixing. For the latter, the availability of extremely short femtosecond to sub-femtosecond pulses is regarded critical to beat the core-hole lifetime.

Generally, a strong request was identified for a modular resonant x-ray scattering and absorption chamber with a large 2D detector on a detector arm. Such a detector should feature a high dynamic range (down to ~500 eV) and be

combined with advanced state preparation using a flexible pump laser suite that covers narrow and broadband THz, mid-infrared up to visible radiation. These capabilities should come along with polarisation analysis and sample environment that allows reaching low temperatures (ideally sub-5 K) and possibly also involve static vector / pulsed magnetic fields (1 Tesla).

Such a chamber would be compatible with time-domain Fourier transform spectroscopy in the soft x-ray regime and the proposals to use Fresnel zone plates for time-revolved single-shot and imaging RIXS. The latter would particularly employ the flexibility offered by the Apple X undulator design (see Chapter 3.5). Moreover, also the proposal for plane wave coherent diffractive imaging should be compatible with its requirements of in-vacuum scanning stage, 2D detector, circularly polarized femtosecond x-rays and infrared/THz excitation.

In addition, for trRIXS tunability of the energy and time resolution within the Fourier limit was identified as a demand. High-resolution time-resolved soft x-ray photoemission spectroscopy (e.g. to look for dynamics of buried interfaces) could benefit from the spectral brightness of the high-brightness SASE or self-seeding modes (Chapters 2.3.2.3 and 2.3.2.1) in combination with time-of-flight detection schemes.

#### 4.4.1.2 Ultrafast chemistry and biology

This session at the PSW [68], covered a broad range of techniques and science and included several contributions from users with pre-existing endstations that could be used at Athos. The instrument discussions covered:

- **An atomic, molecular and optical (AMO) endstation**, which is capable of measuring a variety of ion/electron signals (COLTRIMS, VMI), forward scattering using a large 2D detector, and transient X-ray absorption spectra. The station will handle a variety of sample injectors, including gas jets, liquid jets, and particle/cluster sources.
- **A surface chemistry endstation** that is designed to measure monolayers of molecules adsorbed onto a metal surface using both X-ray absorption and emission spectroscopy.
- **A surface science endstation** which measures the structure of molecules on surfaces using photoelectron diffraction.

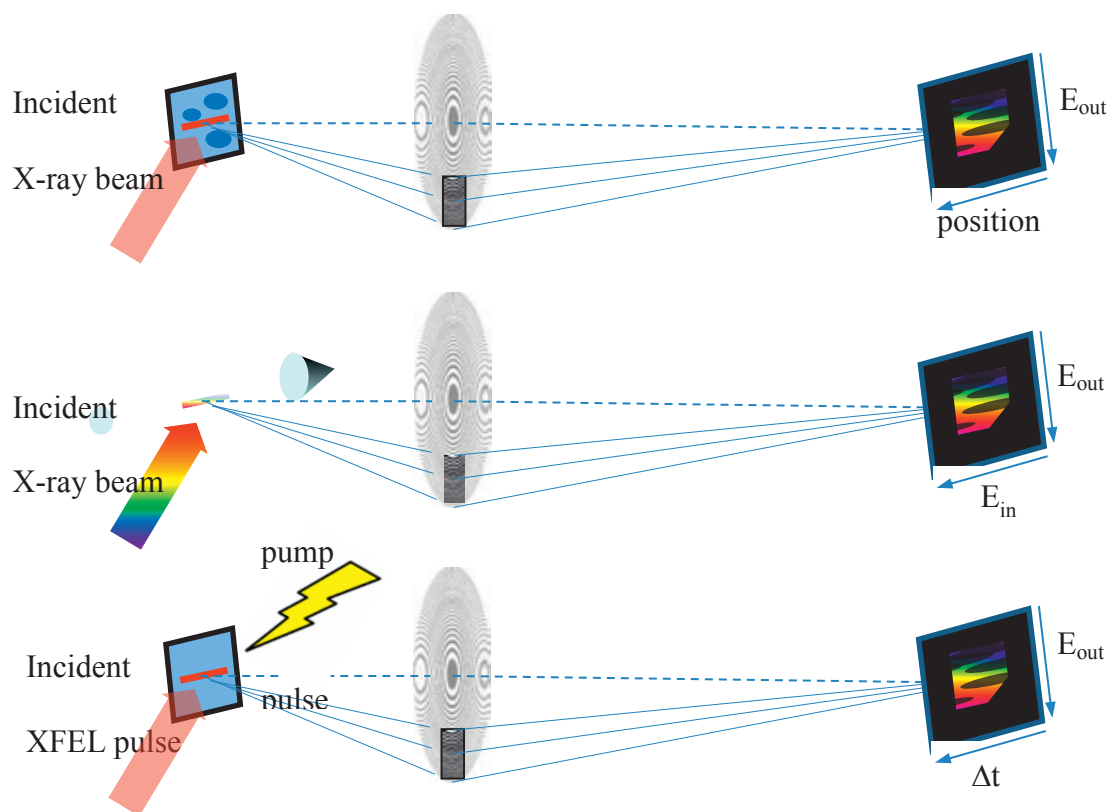


Fig. 4.4.2. Examples of simultaneous measurements that can be performed using off-axis zone plates.

The latter two instruments already exist and require Athos only to ensure compatibility with them on a suitable beamline. The previous version of the surface chemistry instrument [73] has been used at LCLS to investigate the dynamics of CO on Ru, where the molecule is probed using X-ray spectroscopy after photoexcitation of the metal surface [74]. The surface science photoelectron instrument has been demonstrated with high-harmonic sources and used at the FLASH XFEL [75] [76]. The AMO instrument is based on two pre-existing instruments that are used regularly at both FLASH and LCLS [77]. In all cases the instruments are compatible with roll-in/roll-out operation, allowing for other specialized instruments to be used, such as for time-resolved resonant XES on liquid samples. In particular several techniques were proposed, which allow single-shot XAS measurements to be performed.

The instruments mentioned above will be able to drive new research and allow SwissFEL's international user community to perform experiments covering a broad range of scientific

topics. During the Photonics Spring Workshop [1] the following topics were discussed:

- Catalytic chemical reactions on surfaces
- Single-particle imaging
- Dynamics of metal clusters upon photoexcitation
- Aerosol formation and structure
- Gas-phase molecular dynamics
- Solution-phase molecular and biomolecular spectroscopy
- Novel uses for nonlinear X-ray spectroscopy (e.g. stimulated X-ray emission [78] [79])
- Multiplexed X-ray spectroscopy (single-shot measurements of multiple experimental observables)

This last topic was a point of interest in both the condensed matter (see 4.4.1.1) and chemistry/biology sessions, since the techniques were applicable to a variety of samples. The ability of the LMN laboratory to produce zone-plates for both spatial and spectral dispersion/focussing, allows experiments to be proposed that measure several observable simultaneously. The various simultaneous combinations included measuring both the X-ray absorption and emission spectra, spatial mapping of the X-ray emission from the sample, and the X-ray absorption spectrum as a function of pump-probe time delay. Some of these examples are shown in Figure 4.4.2.

# 5 Building and infrastructure

## 5.1 Building layout

With a total length of 719 m and a width ranging from 6 m to 45 m, the SwissFEL facility is located a few hundred meters south-east of PSI-East (see Figure 5.1.1). This location pre-

sents the advantage of having a continuous area (with possibility of future extensions) and homogeneous ground to contain the SwissFEL installation, in contrast to the PSI-West area, which would be cut by a small river and limited in size. Figure 5.1.1 shows some views of the buildings



Fig. 5.1.1: SwissFEL views location for SwissFEL (Bottom: map; Top: aerial view with main access points).

Fig. 5.1.2: Building foot print drawing (top view) from z=290 m to z=400 m (top picture) and from z=400 m to z=550m (bottom picture). The red line indicates the trajectory followed by the Athos bunch from extraction point to the Athos Undulator Line.

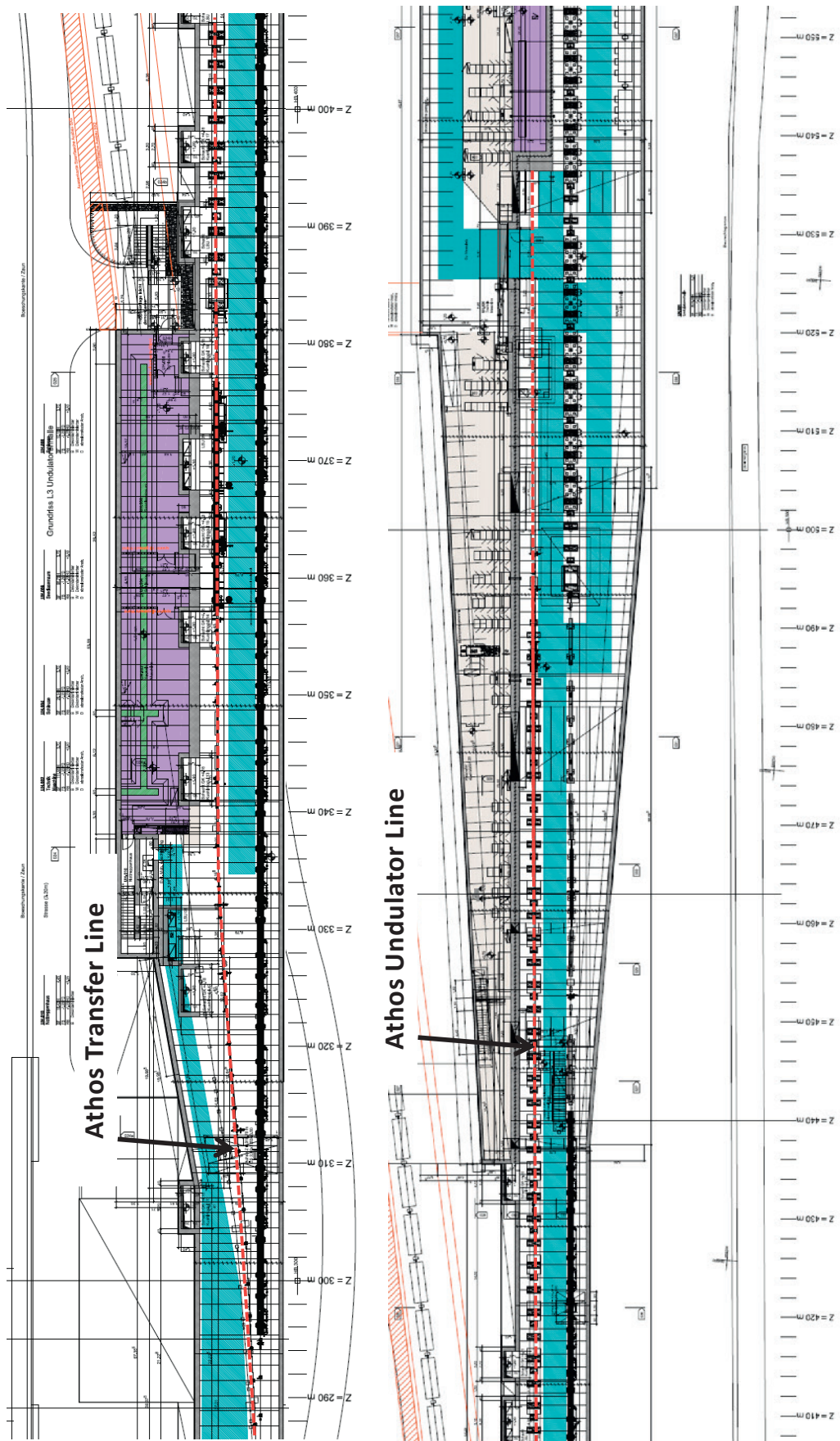


Fig. 5.1.3: Building foot print drawing from z=550 m to z=660 m. The yellow line indicates the Athos Optical Hutch and the red line corresponds to the Athos Experimental Hutch.

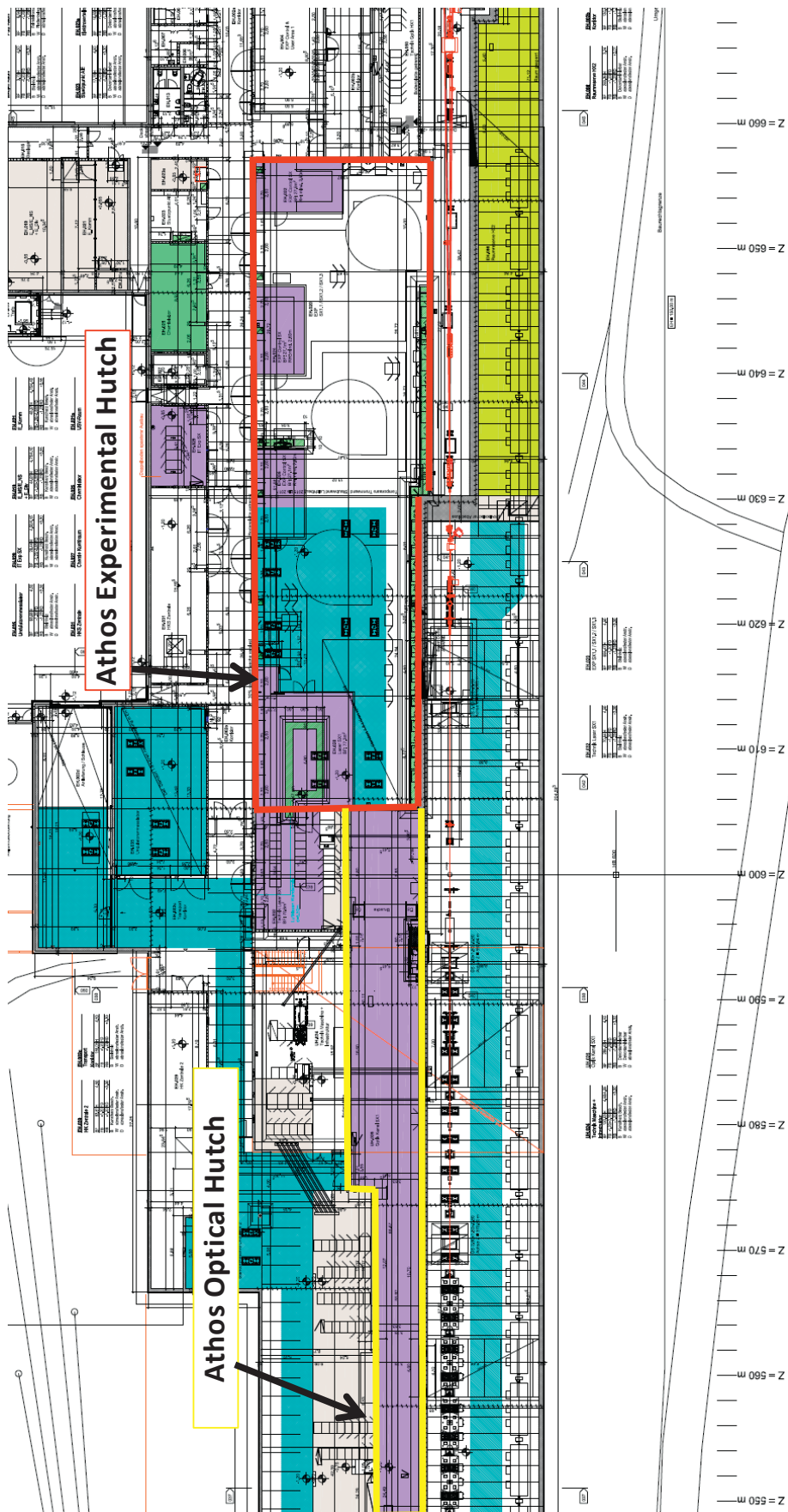




Fig. 5.1.4: Room OSFA-L3.140 in December 2016.

half-covered by earth. Two sections of the building are entirely covered with soil, to allow animals to cross the building.

Access to the facility is ensured via a road alongside the building. The Beam Tunnel and the Undulator area situated under the natural ground level are accessible through escape stairs and via a loading zone equipped with a crane for large equipment installation (Figure 5.1.1). The electron beam is flowing from south to north. More details on the SwissFEL building design can be found in [15].

The Athos line starts with the extraction point at  $z = 265\text{m}$  and will follow a dog-leg shape until  $z = 338\text{m}$ . After this point the Athos line will stay parallel to linac 3 & Aramis undulator line. The distance between the 2 electron beamlines is 3.75 m. The electron beam trajectory of Athos is represented by a red dashed line on the building map of Figure 5.1.2. After the electron beam dump at  $z = 517\text{m}$ , the photon beam generated in the undulator line continues straight to the Athos Optical Hutch (yellow rectangle in Fig. 5.1.3). In the Optical Hutch the FEL beam can be deflected and sent to three end stations located in the Athos experimental Hall. With about 650 m<sup>2</sup>, the Athos experimental hall (red rectangle in Fig. 5.1.3) is a large open space to allow flexibility in the installation of the future experiments.

Besides the main tunnel for beam transport several other rooms are dedicated to the Athos infrastructure. For the components located at the beginning of the Athos line from

$z = 265\text{m} - 460\text{m}$ , the electronic control instruments (power supply, diagnostic electronic, PLC electronic ...) are located in electrical cabinets situated in the upper floor. The RF klystron / modulator system required for the C band module of Athos is located at  $z \sim 354\text{m}$  in OSFA-L3.140 (a side room separated from main RF gallery (Fig. 5.1.4 and Fig. 5.1.5)).

The layout of the C band modulator in the room OSFA-L3.140 will be similar to the one used for the main linac of SwissFEL:

- A two meters wide transport way (without double floor) is reserved along the west wall for transport of large RF components.
- The electrical racks are installed on a 55 cm high double floor filled with cable trays to connect racks to machine components (magnets, diagnostics, ...). The electrical connection from top floor to tunnel is insured via holes in the concrete shielding (no direct vertical drilling).

Downstream  $z \sim 460\text{m}$ , the building is only a one storey building and so the infrastructure electrical cabinets are located on the same level in the room going along the tunnel (Fig. 5.1.2 \_ bottom).

As a consequence, the RF modulator for the X band transverse deflecting cavities will be located in the side gallery OSFA-UH.020 at  $z \sim 485\text{m}$ .

The preparation and measurements of the Athos undulator modules will be done in the undulator laboratory OSFA-EH.035. Every month a new undulator will be assembled

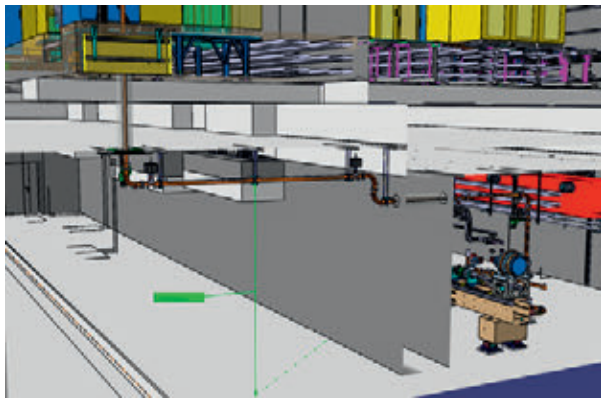
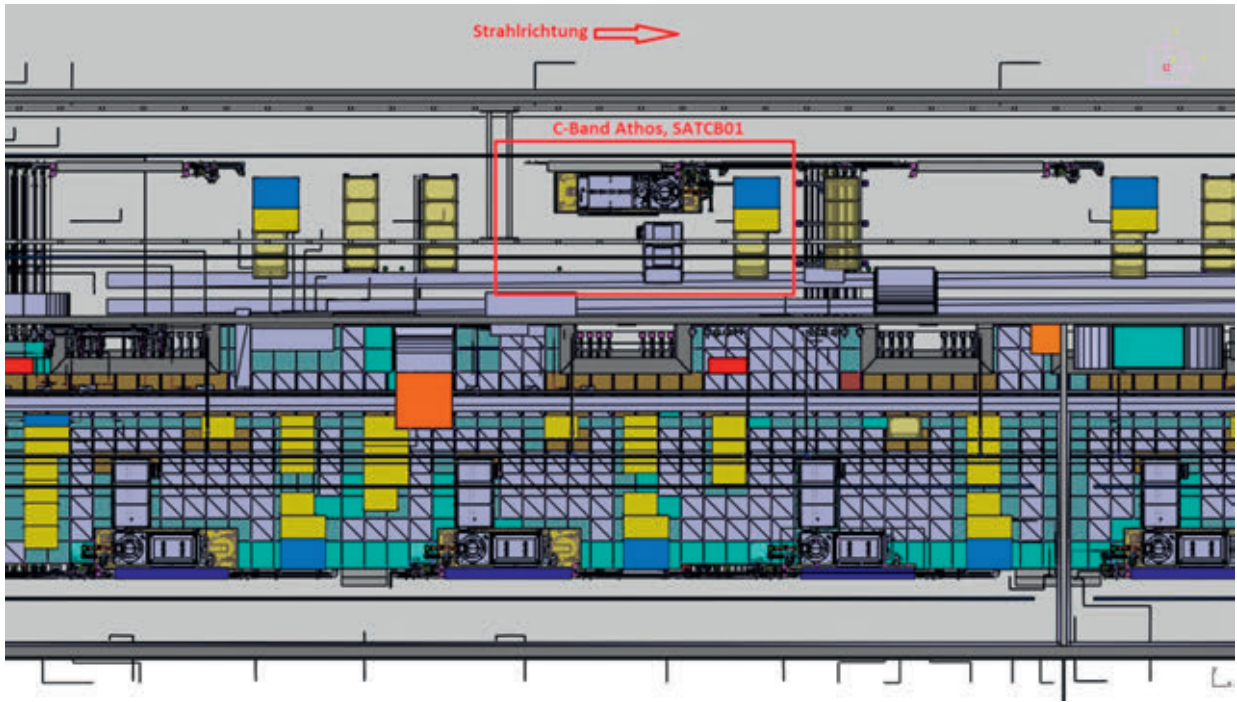


Fig. 5.1.5: Top view of the RF gallery the Athos C band module (top picture). The waveguide crosses the floor and goes through the UH.006 room and then into the tunnel (bottom picture).

Fig. 5.1.6: Rack gallery in OSFA-UH.020 around  $z \sim 485\text{m}$  where the cable trays are deviated to allow the installation of the X band modulator.

Fig. 5.1.7: Building view at  $z \sim 400\text{m}$  with the groundplates for the undulator on the left side and linac 3 on the right side.



	Normal operation (2 lines operated in parallel)		Maximale Power (only one line at a time)	
	Aramis	Athos	Aramis	Athos
frequence ( $f_{GL}$ )	100 Hz			
Charge pro pulse	200 pC	200 pC	2 x 400 pC	2 x 400 pC
Charge pro hour	72 $\mu$ C	72 $\mu$ C	288 $\mu$ C	288 $\mu$ C
Beam energy	5.8 GeV	3.4 GeV	7.0 GeV	3.8 GeV
Beam power	116 W	68 W	560 W	304 W

Table 5.2.1:  
Main beam power parameters allowed in the Aramis and Athos lines.

and delivered in the tunnel. The undulators with more than 12 tons weight are positioned on massive steel ground plates (Fig. 5.1.7). The floor flatness and the availability of pressurized air make it possible to transport the undulator with air cushion based vehicles.

The Athos beam dump is installed below the undulator hall floor. The Athos Front End (from Athos beam dump until the shielding wall of the Athos Optical Hutch) is integrated in the tunnel. The optical components (mirrors and monochromators) are located in the Athos Optical Hutch. The Athos Optical Hutch is separated from the UH building by a 2 m thick shielding wall to protect users from electron induced radiations (an additional beam safety wall will be located at z~507.5 in case of failure of main dump dipole).

## 5.2 Safety issues

A detailed overview of all safety aspects of SwissFEL installation can be found in [80].

With the installation and operation of the Athos line several existing systems have to be extended or revised:

- The remote access control system (PSYS) have to include the Athos RF power plants which should be disabled before giving access to the tunnel.
- The safety check tour (“Rundgang”) before closing the tunnel has to be extended to the Athos line.
- General safety (escape route, new moving equipment ...) will be revised in view of the Athos line integration.

The particularity of a Free Electron Laser installation is the generation of radiation which required radiation protection.

Detailed information about the radiation shielding of the SwissFEL building can be found in [81] [15].

The level of radiation depends on the electron beam power produced in the installation. Table 5.2.1 summarized the beam power allowed with the installed shielding elements (shielding walls, beam dump, ...).



Fig. 5.2.1: Top picture: Installation of the beam dump shielding blocks in the beam dump groove (2013). Bottom picture: Athos beam stopper in front of the undulator line.

Building Name	Device	Nominal Electrical Power Consumption / Item [kW]	Number of Items	Nominal Power Consumption [kW]	Nominal Water Cooled Power [kW]	Nominal Power Dissipated in Air [kW]	
Switch-Yard (z= 273 to 338m)  and Athos Line (z=338 to 384 m)	<b>RF:</b>						
	RF Module (Modulator; solenoid; klystron)	80	1	80	72	8	
	LLRF (pre-ampli, ...)	4	2	8			
	LLRF Cooling Cabinet	5	2	10	5		
	<b>Magnets:</b>						
	Athos AFL Dipoles	0.86	1	0.86	0.774	0.086	
	Athos Switchyard dipoles AFBC3	6.288	1	6.288	5.6592	0.6288	
	Switchyard quadrupoles QFD	0.13	37	4.81		4.81	
	Switchyard sextupoles HFB	0.02	7	0.14		0.14	
	<b>Vacuum:</b>						
	Ion Pumps power supplies	0.6	19	11.4		11.4	
	Vacuum gauge controllers	0.04	5	0.2		0.2	
	Vacuum SPS modules	0.01	25	0.25		0.25	
	Vacuum PC	0.3	1	0.3		0.3	
	<b>Diagnostic:</b>						
	Motor driver rack	0.6	3	1.8		1.8	
	PC for Camera	0.3	5	1.5		1.5	
	VME	0.3	3	0.9		0.9	
	Athos Undulator Line (z= 384m to z=503 m)	<b>Undulator UE38:</b>					
		Undulator Positioning Motors	0.4	16	6.4	0	6.4
Undulator Gap Motors water T stabilization		0.2	16	3.2	2.88	0.32	
<b>Magnets:</b>							
FODO Cell Quadrupole QFF (+ Correctors + PS)		0.122	34	4.148	0	4.148	
BMP driving electronic mini-racks (MBU)		0.3	18	5.4	0	5.4	
Athos Self seeding dipoles AFSS (+ Corr. + PS)		1.13	1	1.13		1.13	
Athos Beam Dump Dipole AFD1 (+ Corr. + PS)		7.5	1	7.5	6.75	0.75	
Matching quadrupoles QFM+SFQFM (+ PS + Corr.)		0.58	1	0.58	0.522	0.058	
Steering magnet Undulators (2*SFU + Earth corr.)		0.3	16	4.8		4.8	
Corrector magnets (sextupole, dipoles, skew...)		0.026		0		0	
<b>RF TDS:</b>							
RF Module X band (Modulator; solenoid, klystron)		81.5	1	81.5	73.35	8.15	
LLRF (pre-ampli, ...)		4	2	8			
LLRF Cooling Cabinet		5	2	10	5		
<b>Vacuum:</b>							
Ion Pumps power supplies		0.6	41	24.6		23.4	
Vacuum gauge controllers		0.04	10	0.4		0.4	
Vacuum SPS modules		0.01	50	0.5		0.5	
Vacuum PC		0.3	2	0.6		0.6	
<b>Diagnostic:</b>							
Motor driver rack	0.6	3	1.8		1.8		
PC for Camera	0.3	3	0.9		0.9		
VME	0.3	3	0.9		0.9		
<b>Mechanical Support:</b>							
QFF motorized Table	0.016	38	0.608		0.608		
<b>Total [kW]</b>			<b>289.4</b>	<b>171.9</b>	<b>90.3</b>		

Table 5.3.1: Estimation of the nominal Electrical power consumption of Athos machine components.

The Athos main beam dump ( $z=517\text{m}$ ) [82] and beam stopper ( $z=383\text{m}$ ) [83] have been installed during the Aramis phase of the project (Fig. 5.2.1). The only missing large shielding element is a safety stopping wall at  $z=503\text{m}$  in case of beam loss near the dump dipole.

In addition to passive shielding, SwissFEL is equipped with a dose rate protection system (DRPS) which continuously measures the radiation level in the tunnel and compares it to the allowed threshold. In case this threshold is exceeded the DRPS system will stop the electron beam in less than one second. The tunnel shielding walls are designed to tolerate a full beam loss of one second per hour.

In order to avoid such events, a machine protection system (independent from the DRPS) based on beam loss monitors will continuously monitor the beam losses and reduce the repetition rate in case losses are thought to be too high for surrounding electronic or if it comes too close to a DRPS limit.

## 5.3 Supply installations

### 5.3.1 Electrical supply and consumption

The electrical distribution comes from PSI site and is distributed from the main divider situated in the Experimental hall to the different building. The middle voltage is converted to low voltage by transformers distributed along the building. There are two electrical power networks foreseen: one for the machine components and one for the infrastructure components. In addition a data network is foreseen to transfer data to/from PSI main control room.

Total electrical consumption is a key parameter for defining the required building infrastructure in terms of electrical supply as well as cooling capacity. The nominal electrical power consumption for Aramis and Athos lines is about 5.2 MW, of which 3.9 MW are used for beam accelerator components and 1.35 MW for infrastructure components (water pumps, air conditioning, etc). The power going to accelerator components (RF modulator; magnets; etc) is completely dissipated in heat losses (the average FEL light power is only about 100 mW). The main consumption is for the RF power plants units (up to 3.5 MW). Most of the heat (4.2 MW) is dissipated by direct water cooling (magnets or

RF modulators) pumped in the ground. The water is then either re-direct to PSI site for heating up other buildings or discharged into the Aare river. The rest of the heat (1 MW) is dissipated in the air, mainly in the RF gallery and the infrastructure rooms.

Table 5.3.1 depicts the electrical consumption of the specific Athos machine components. The table is based on 100 Hz operation repetition rate and shows an estimation of the nominal electrical consumption of around 300 kW. In fact, most of the consumption is for the 2 RF power plants and those power plants will be operated at about 80 – 90 % of their maximum. The nominal electrical power consumption from front end, optical hutch and experimental stations can be estimated to 300 – 350 kW as for the Aramis line.

### 5.3.2 Heating, cooling, air conditioning and water supplies

#### 5.3.2.1 Summary

The concept of the heating, cooling and air conditioning infrastructure is characterized by a combination of common, cost-effective techniques with low electrical consumption. The challenging requirements regarding air temperature stability ( $\pm 0.1\text{K}$ ) inside the beam tunnel, as well as the large amount of heat dissipation, can be handled by a proven combination of direct cooling, using ground water as sink and a simple forced-air cooling system over the whole tunnel length. The required air conditioning within the experimental hall is ensured by laminar air flow, generated by so-called displacement air outlets. The technical gallery above the beam tunnel will be similar to server rooms, conditioned by local forced-air cooling systems.

The chosen concept will be applied throughout the whole year, without additional cooling. The cooling comes from existing ground water right at the facility location. The variation of the ground water temperature is extremely small, which helps greatly in meeting the high requirements on temperature stability. In addition, it allows the use of simple cooling techniques, and it is at the same time very ecological and economical.

#### 5.3.2.2 Heating / Cooling facilities

The ground water is pumped from the pump station near Linac 2 and will be distributed to several infrastructure rooms

along the building. The maximum flux of water which is allowed to be pumped is 95 l/s. This flow is also enough to cool both Aramis and Athos line.

The groundwater has a maximum temperature of 15 °C and the maximum temperature of the water rejected to the Aare river is 30 °C. Three cooling circuits are foreseen for all components between the gun and the beam dump:

- normal water cooling circuit 17±0.2 / 23 °C (In / Out temperature)
- demineralised water circuit 19±01 / 36 °C
- demineralised water circuit 60±1 / 80 °C

Twenty-one (21) cooling stations (Fig. 5.3.2.1) distribute locally the cooling water to the components of the facility. Each station consists of few sub-distribution circuits with different regulation requirements and topology (see example of Fig. 5.3.2.2).

For the Athos C band module at z=357m, an additional cooling station will be installed in the first floor gallery at z~365m: KKV15.

Globally one identifies nine (9) classes of sub-distribution circuits distributed within the 21 cooling stations. The classes were defined according to the topology of the sub-circuit, the required operating temperature of the component to cool (klystron, accelerating cavities, magnets, racks ...).

Those cooling circuit are installed in parallel along the entire building on the ceiling of the UH and infrastructure gallery (Fig. 5.1.6).



Fig. 5.3.2.1: Picture of cooling station KKV14 installed at SwissFEL.

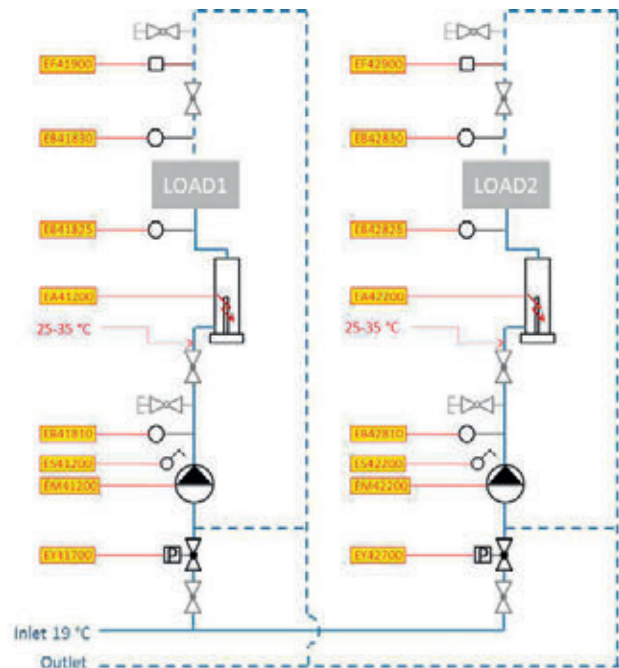


Fig. 5.3.2.2: Principle layout for sub-distribution module „RF accelerating cavities”. Example with two independent cavity sub-distribution circuits within one cooling station.

The experimental hall has an independent cooling circuit of demineralised water 20/26 °C.

Inside the beam tunnel, the mains trays will also run along the ceiling, just above the beam components (Fig. 5.1.7). The trays will contain the following supplies:

- Cooling water in/out
- Pressurized air

At the switchyard, the supply tray is going one floor up from the UH ceiling to the infrastructure gallery ceiling.

### 5.3.2.3 Air conditioning units

Table 6.3.2.1 summarizes the requirements in terms of temperature and temperature stability. The stability of ±0.1 K in the undulator hall, for example is insured over a length of 5 m and over 5 hours. The temperature of the undulator hall should never (also during shutdown) change by more

Air Temperature Specifications at SwissFEL		
Room	Temperature	Humidity
Beam Tunnel, Undulator Hall, Front End and X ray Switch Yard	24 °C +/- 0.5 K (absolute) and +/- 0.1 K (near beam axis)	30–65 %
Infrastructure Gallery and Rooms (L3.140)	21 – 26 °C +/- 2K over 24 hours	25–65 %
Undulator Lab	24 °C +/- 0.2 K	30–55 %
UH Entrance and Transport channel along undulator hall	24 °C +/- 2 K	30–55 %
Experimental Hall	24 °C +/- 0.5 K	30–55 %
Laser Rooms (ISO Class 7)	21 °C +/- 0.1 K	40–45 % +/- 2.5%
Oil Tanks Room	15–40 °C	

Table 6.3.2.1:  
Air Temperature requirements in SwissFEL.

than 2°C (ie.  $24 \pm 1^\circ\text{C}$ ) or it could irreversibly affect the position of the magnets in the undulator. The operating temperature of the beam tunnel is  $24^\circ\text{C} \pm 0.5 \text{ K}$ . A separate heating group is foreseen for heating the offices, restrooms and labs.

The beam tunnel will be equipped with approximately 12 air circulation cooling units, to control the temperature within approximately  $\Delta t = \pm 0.1\text{K}$  at a specific point in the tunnel. The temperature difference between different locations in the tunnel, however, will be higher. Each unit has a cooling capacity of about 12 kW and air exchange capacity of  $6000\text{m}^3/\text{h}$ . They will all sit on vibration dumpers and are

distributed inside the infrastructure gallery. Fresh air will be introduced near the undulator hall side of the tunnel and exhausted at the gun end. In the beam tunnel, air will circulate towards the gun with a speed of 0.1 m/s; the temperature of the tunnel can be measured (and recorded) every 10 m in the tunnel and locally adjusted if necessary.

For Athos, one additional air cooling unit (monoblock) will be installed in room L3.140 in order to stabilize the temperature within  $\pm 2\text{K}$ .

## 6 References

- [1] R. Bakker *et al.*, X-FEL concept based on a low emittance gun, Report No. Volume VI, 2004.
- [2] R. J. Bakker *et al.*, in *FEL06*, Berlin, Germany (2006).
- [3] B. D. Patterson, Time-Resolved X-ray Spectroscopy – Mapping electron flow in matter with the ATHOS beamline at SwissFEL, Report No. PSI Bericht Nr. 14-01, 2014.
- [4] SwissFEL Technical Design Report (TDR), [https://intranet.psi.ch/Swiss\\_FEL/SwissFELTDR](https://intranet.psi.ch/Swiss_FEL/SwissFELTDR).
- [5] E. Prat *et al.*, *J. Synchrotron Rad.* **23**, 861 (2016).
- [6] E. Prat *et al.*, *J. Synchrotron Rad.* **23**, 874 (2016).
- [7] M. Calvi *et al.*, *J. Synchrotron Rad.* **24**, 600 (2017).
- [8] R. Coisson, *Particle Accelerators* **Vol. 11**, pp. 245 (1981).
- [9] N. A. Vinokurov and N. A. Skrinsky, Report No. Report BINP 77-59. , 1977.
- [10] E. Prat *et al.*, *Phys. Rev. ST Accel. Beams* **18**, 100701 (2015).
- [11] S. Reiche and E. Prat, *J. Synchrotron Rad.* **23**, 869 (2016).
- [12] E. Prat *et al.*, *Nuclear Instruments and Methods in Physics Research A* **In Press** (2017).
- [13] B. W. J. McNeil *et al.*, *Phys. Rev. Lett.* **110**, 134802 (2013).
- [14] N. R. Thompson and B. W. J. McNeil, *Phys. Rev. Lett.* **100**, 203901 (2008).
- [15] SwissFEL Technical Design Report, [https://intranet.psi.ch/Swiss\\_FEL/SwissFELTDR](https://intranet.psi.ch/Swiss_FEL/SwissFELTDR).
- [16] E. Prat *et al.*, *J. Synchrotron Rad.* **23**, 874 (2016).
- [17] G. A. Loew and O. H. Altenmueller, Design and applications of RF deflecting structures at SLAC, Report No. Report PUB-135 SLAC, 1965.
- [18] E. Prat and M. Aiba, *Phys. Rev. ST Accel. Beams* **17**, 052801 (2014).
- [19] B. W. Zotter and S. Kheifets, *Impedances and wakes in High Energy Particle Accelerators* (Singapore: World Scientific, 1998).
- [20] E. Prat and S. Reiche, *Phys. Rev. Lett.* **114**, 244801 (2015).
- [21] V. Petit *et al.*, *Appl. Phys. B* **78**, 681 (2004).
- [22] A. Trisorio *et al.*, in *FEL2013*, New York, USA (2013).
- [23] R. Abela *et al.*, SwissFEL Conceptual Design Report, Report No. 10-04, 2012.
- [24] T. Sakurai *et al.*, in *IPAC*, Kyoto, Japan (2010).
- [25] C. Behrens *et al.*, *Nature Communications* **5**, 3762 (2014).
- [26] Y. Ding *et al.*, in *LINAC2014*, Geneva, Switzerland (2014).
- [27] L. Doolittle *et al.*, in *LINAC'06*, Knoxville, Tennessee, USA (2006).
- [28] S. Hunziker *et al.*, in *IBIC2014*, Monterey, USA (2014).
- [29] T. Schietinger *et al.*, *Phys. Rev. Acc. and Beams* **19** (2016).
- [30] S. Sanfilippo *et al.*, *IEEE Transactions on applied superconductivity* **24**, 4002005 (2014).
- [31] S. Sanfilippo, edited by F. Meeting (PSI, 2014).
- [32] S. Sidorov, Requirement Specification QFDP / QFDS Quadrupole Magnets, Report No. FEL-SS88-007-7, 2011.
- [33] S. Sidorov, Requirement Specification QFM Quadrupole Magnets, Report No. FEL-SS88-010-2, 2012.
- [34] S. Sidorov, Requirement Specification QFFP / QFF Quadrupole Magnets, Report No. FEL-SS88-008-0, 2011.
- [35] <http://magnet.web.psi.ch/Measurements/>.
- [36] S. Sidorov, Requirement Specification AFBC3 Dipole, Report No. FEL-SS88-040-1, 2013.
- [37] S. Sidorov, Requirement Specification AFD1 Dump Dipole, Report No. FEL-SS88-045-2, 2013.
- [38] R. Ganter *et al.*, Athos Delay Chicane Dipole Magnets AFSS, Report No. FEL-GR16-178, 2017.
- [39] S. Sidorov, Requirement Specification HFB Sextupole Magnet, Report No. FEL-SS88-054-0, 2014.
- [40] M. Calvi *et al.*, in *FEL'14*, Basel, Switzerland (2014).
- [41] R. Ischebeck *et al.*, in *IBIC2014*, Monterey, USA (2014).
- [42] G. L. Orlandi *et al.*, in *FEL2014*, Basel, Switzerland (2014).
- [43] C. O. Loch *et al.*, in *IBIC2015*, Melbourne, Australia (2015).
- [44] A. Zandonella, Heilige List – FEL-SL88-051-8.8.1\_SwissFEL\_Haupt-Komponenten\_OracleDB, Report No. FEL-SL88-051-8.8.1, 2017.
- [45] B. Keil *et al.*, in *IBIC2015*, Melbourne, Australia (2015).

- [46] H. Joehri *et al.*, in *MEDSI2012*, Shanghai, China (2012).
- [47] K. Dreyer and T. Hoewler, in *IWAA2012*, Fermilab, Batavia, USA (2012).
- [48] Inventory Tool, <https://inventory.psi.ch>.
- [49] T. Celcer *et al.*, SwissFEL IOC and Application Configuration Management, Report No. FEL-CT84-001-1, 2016.
- [50] B. Kalantari, SwissFEL Timing and Event System, Report No. FEL-KB84-001-1, 2014.
- [51] B. Kalantari, in *EPICS Collaboration Meeting 2016*, Lund, Sweden (2016).
- [52] D. Zimoch, in *EPICS collaboration meeting 2013*, (2013).
- [53] WAGO system (Twiki), <https://intranet.psi.ch/Controls/WagoInputOutputControl>.
- [54] C. Pradervand *et al.*, SwissFEL Motioncontrol Solution Ver. 1.4, Report No. TM-16-14-03, 2016.
- [55] SwissFEL Cameras (Twiki), <https://intranet.psi.ch/Controls/SwissFELCameras>.
- [56] K. Tiedtke *et al.*, *J. Appl. Phys.* **103**, 094511 (2008).
- [57] T. Kensuke *et al.*, *Rev. Sci. Instrum.* **82**, 023108 (2011).
- [58] K. Tiedtke *et al.*, *Optics express* **22**, 21214 (2014).
- [59] M. Kato *et al.*, *Metrologia* **47**, 518 (2010).
- [60] E. Ferrari *et al.*, *Scientific Reports* **5**, 13531 (2015).
- [61] P. N. Juranic *et al.*, *Optics express* **24**, 30004 (2014).
- [62] I. Gorgisyan *et al.*, *Optics Express* **25**, 2080 (2017).
- [63] F. Riemer and R. Torge, *Nuclear Instruments and Methods in Physics Research A* **208**, 313 (1983).
- [64] T. Kachel *et al.*, *J. Synchrotron Rad.* **22**, 1301 (2015).
- [65] R. Follath and J. S. Schmidt, *AIP Conference Proceedings* **705**, 631 (2004).
- [66] J. Viefhaus *et al.*, *Nuclear Instruments and Methods in Physics Research A* **710**, 151 (2013).
- [67] T. Koyama *et al.*, in *Proc. SPIE* (2015).
- [68] Photonics Spring Workshop – SwissFEL ATHOS and SLS-2, <https://indico.psi.ch/internalPage.py?pageId=0&confId=5401> (2017).
- [69] N. Trigo *et al.*, *Nat. Phys.* **9**, 790 (2013).
- [70] D. Zhu *et al.*, *Phys. Rev. B* **92** (2015).
- [71] M. Dean *et al.*, *Nat. Mater.* **15**, 601 (2016).
- [72] J. Miao *et al.*, *Science* **348**, 530 (2015).
- [73] T. Katayama *et al.*, *J. Electron Spectrosc* **187**, 9 (2013).
- [74] A. Nilsson *et al.*, *Chem. Phys. Lett.* **675**, 145 (2017).
- [75] M. Greif *et al.*, *Phys. Rev. B* **94**, 054309 (2016).
- [76] M. Greif *et al.*, *Struct. Dyn.* **2** (2015).
- [77] L. Strüder *et al.*, *Nuclear Instruments and Methods in Physics Research A* **614**, 483 (2010).
- [78] K. Kunnus *et al.*, *J. Electron Spectrosc* **204**, 345 (2015).
- [79] M. Beye *et al.*, *Nature* **501**, 191 (2013).
- [80] R. Scheibl, Sicherheitsbericht SwissFEL, Report No. TM-85-15-01, 2015.
- [81] A. Fuchs, SwissFEL shielding consideration, Report No. FEL-FU96-028, 2015.
- [82] R. Ganter, SwissFEL Aramis and Athos Beam Dumps Technical design report, Report No. FEL-GR16-170, 2015.
- [83] R. Ganter, SwissFEL Aramis and Athos Beam Stoppers Technical Design Report, Report No. FEL-GR16-177, 2015.

# PSI in brief



The Paul Scherrer Institute PSI is a research institute for natural and engineering sciences, conducting cutting-edge research in the fields of matter and materials, energy and environment and human health. By performing fundamental and applied research, we work on sustainable solutions for major challenges facing society, science and economy. PSI develops, constructs and operates complex large research facilities. Every year more than 2500 guest scientists from Switzerland and around the world come to us. Just like PSI's own researchers, they use our unique facilities to carry out experiments that are not possible anywhere else. PSI is committed to the training of future generations. Therefore about one quarter of our staff are post-docs, post-graduates or apprentices. Altogether PSI employs 2000 people, thus being the largest research institute in Switzerland.

## Imprint

**Photography and Graphics**  
Paul Scherrer Institut,

**Design and Layout**  
Monika Blétry

**Printing**  
Paul Scherrer Institut

**Available from**  
Paul Scherrer Institut  
Events and Marketing  
5232 Villigen PSI, Switzerland  
Tel. +41 56 310 21 11

Villigen PSI, September 2017

